12-2016

Multivariate calibration of a load sensor for dynamic and static freight railcar applications

Dylan Michael Blackwell
The University of Texas Rio Grande Valley

MULTIVARIATE CALIBRATION OF A LOAD SENSOR FOR DYNAMIC AND STATIC FREIGHT RAILCAR APPLICATIONS

A Thesis

by

DYLAN MICHAEL BLACKWELL

Submitted to the Graduate College of
The University of Texas Rio Grande Valley
In partial fulfillment of the requirements for the degree of

MASTER OF SCIENCE ENGINEERING

December 2016

Major Subject: Mechanical Engineering

MULTIVARIATE CALIBRATION OF A LOAD SENSOR FOR DYNAMIC AND STATIC FREIGHT RAILCAR APPLICATIONS

A Thesis
by
DYLAN MICHAEL BLACKWELL

COMMITTEE MEMBERS

Dr. Constantine Tarawneh
Co-Chair of Committee

Dr. Stephen Crown
Co-Chair of Committee

Dr. Robert Jones
Committee Member

December 2016

ABSTRACT

Blackwell, Dylan. M., Multivariate Calibration of a Load Sensor for Static and Dynamic Freight Railcar Applications. Master of Science Engineering (MSE), December, 2016, 180 pp., 9 tables, 87 figures, 42 references.

Approximately 40% of intercity freight transportation occurs by rail, making it the most widely used method of transporting large commodities. Currently, the load of freight railcars is measured by weighbridges or retrofitted tracks at isolated locations. This paper provides proof of concept verification for an onboard railcar load sensor and presents analysis on the accuracy of the proposed correlations: one second-order model, one third order model, and one multivariate model that incorporates the bearing operating temperature as read by the onboard sensor. The proposed load sensor can be readily implemented in freight railcars with minimal adjustments to the current bearing adapter assembly. The incorporation of the temperature sensors to the proposed onboard load sensing system provides added condition monitoring capability, and allows for a much improved load measurement with an accuracy of within 2% of the actual value.

DEDICATION

This work is dedicated to my friends and family, all of which helped me to pursue my dream of continuing my engineering education. My father, Michael Blackwell, for always encouraging me to embrace the subjects I enjoy. My mother, Shirla Blackwell, for being my foundation from childhood on. To my friends, for continually offering your support and a lending ear. This thesis would not have been possible without all of you. Thank you for everything.

ACKNOWLEDGEMENTS

I would like to thank my Co-Chair, Dr. Constantine Tarawneh, for always leading his research assistants by example and working hard at everything he does. He is not only a great leader, but a mentor who helps his students to reach their full potential. Thank you for not only teaching me the principles of hard work, but also reigniting my passion for engineering.

I would also like to thank my Co-Chair, Dr. Stephen Crown, for all the knowledge and assistance you have given over the past years. The problems were not always ordinary, and you were able to think of extraordinary solutions.

I would also like to thank Dr. Robert Jones, for being such a great influence to his students. Thank you for always putting forth your encyclopedic knowledge in every conversation and allowing pupils to expand their minds.

A special thanks goes out to the Railroad Research Group for not only the vast amount of help and support, but for being great friends and a joy to work with.

TABLE OF CONTENTS

Page

LIST OF TABLES

Page

LIST OF FIGURES

Page

CHAPTER I

INTRODUCTION AND BACKGROUND

When observing the modern age, it may come as a surprise that rail remains the prominent means of intercity freight transportation. An estimated 40% of freight travels by rail, leading the second most utilized transportation method, via truck, by 10.9%. It is described as being arguably "the safest, most efficient, and cost effective" method in the world by the Federal Railroad Administration [1]. Yet despite its advantage in efficiency, limitations arise from the fact that all systems of the train must work in unison to ensure the safety of the cargo as well as pedestrians. These limitations can end up being the cause of massive, costly derailments. Consequently, oversight is required by most rail corporations to prevent catastrophes, such as that which occurred in West Virginia in 2015, where 26 tanker cars derailed and threatened the water supply of the nearby population [2]

Wheel misalignment, the foremost factor of derailments, can be caused by: excessive speeding on curves, track defects, and railcar suspension failures, involving events such as hunting or the overheating of defective bearings [3]. The majority of railroad research and development is focused on preventative measures targeting the dynamic and static health of each component that lies within the railcar suspension system. One of the most examined components, the double-tapered roller bearing, seen in Figure 1, is used as a railroad standard due to its ability to handle both axial and radial loads [4]. Currently, there are non-contact devices and techniques

employed in the field that aim to monitor the health of bearings, but studies have found these to be somewhat ineffective in identifying the onset of bearing failure [4].

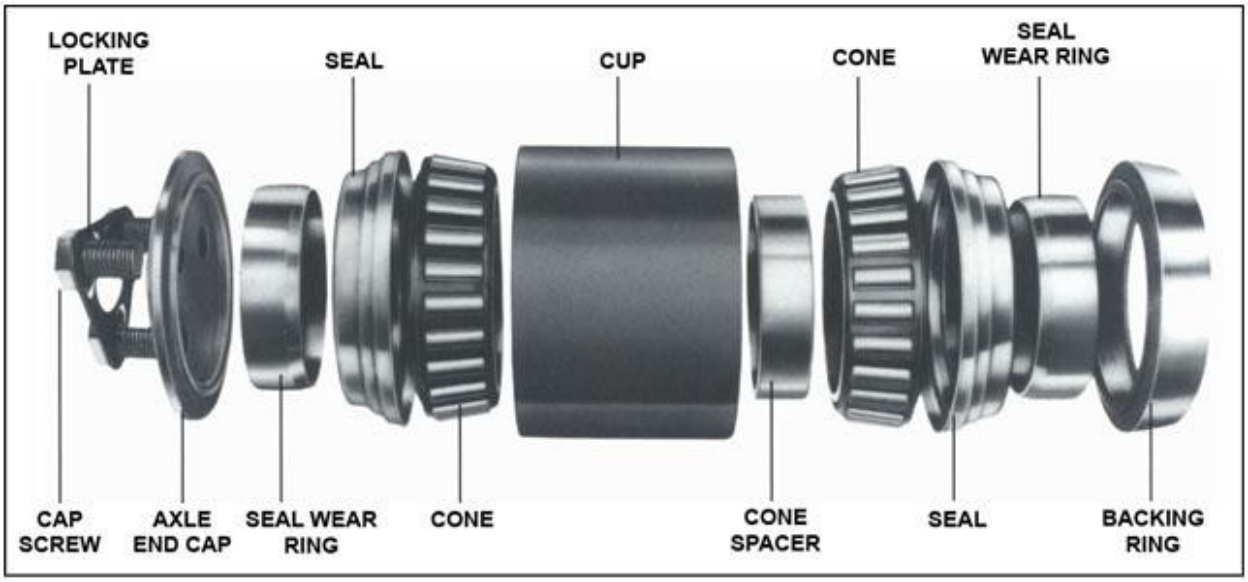

Figure 1. Components of a Double-Tapered Roller Bearing [6]

The Railroad Research Group (RRG) at the University of Texas Rio Grande Valley (UTRGV), previously the University of Texas-Pan American, has made incredible strides in the research and development of innovative railroad bearing condition monitoring technologies and techniques. From its inception, the research conducted by the UTRGV Railroad Research Group has provided pivotal product development and testing, and has further resulted in numerous publications that have influenced the Association of American Railroads (AAR) regulations concerning the guidelines for bearing removal and refurbishing. This program is progressing towards continuous onboard health monitoring systems aimed at categorizing suspension train defects through the assessment of bearing conditions and would be achieved by the development of a wireless sensor unit that will communicate with a centrally-mounted logic circuit board that would be able to analyze the acquired data and diagnose the condition of the bearings that are outfitted with a wireless sensor unit.

The three essential parameters required for a complete bearing health assessment are: temperature, vibration, and load. The UTRGV RRG has dedicated years to the research and testing of a complete bearing health monitoring system known as the Smart Adapter©. The work presented in this thesis focuses on the design and implementation of a load sensor insert embedded in a Smart Adapter© that incorporates raceway temperature data collected by two analog voltage temperature sensors into a multivariate regression calibration to accurately measure and monitor the load applied to the bearing. It will incorporate two of the three assessment measures, therefore, providing for a reliable, onboard freight car load monitoring system that can be readily implemented and calibrated with minor modifications to the present bearing adapter assembly.

1.1 A Brief History of the Railroad Industry

From its inception in the 1830s, with Peter Cooper's steam powered locomotive, to the introduction of the extreme regulations of the 1930s, the railroad industry prospered. In the year 1850, there was slightly over 9,000 miles of railroad in operation. This number has increased to the 138,623 miles that are currently found across the United States [7], as can be seen in Figure 2. Not only does this system transport more cargo than any other freight transportation in the world, but it additionally provides 221,000 jobs across the United States and provides indirect benefits such as the reduction of both greenhouse gas production and highway congestion and accident fatalities [8].

The railroad industry hit an all-time low and was on the verge of collapse just prior to the 1980s.The majority of rail companies were bankrupt and the return of investment was extremely low, approximately 2%. Over 20% of rail mileage was owned by penniless companies, which resulted in the degradation of safety and maintenance standards [9]. The latter resulted in nearly

47,000 miles of rail line reduced to strictly low speed operations. The aforementioned was attributable to the strict federal regulations that were imposed beginning in the 1930s, which included making all business deals public knowledge and barring the industry from determining its own shipping rates.

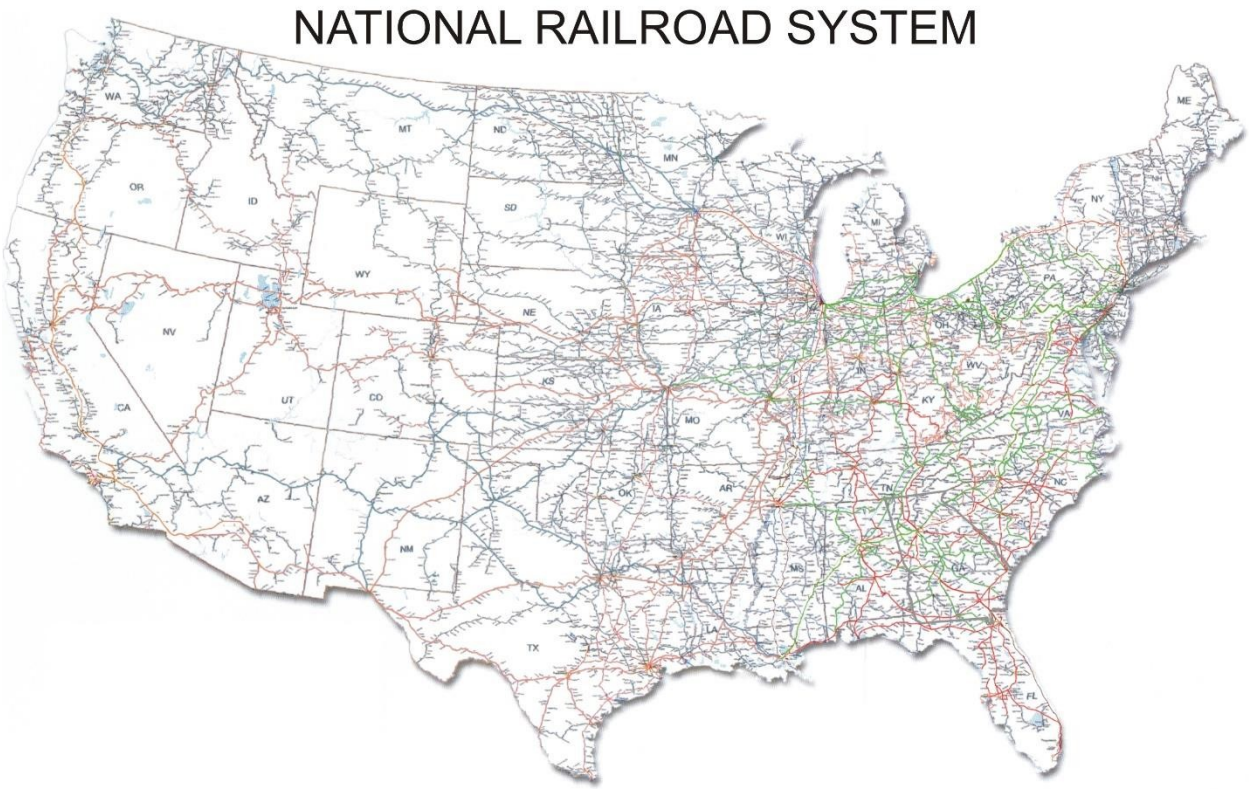

Figure 2. Modern United States Railroad System [10]

The Staggers Rail Act of 1980 followed the Railroad Revitalization and Regulatory Reform Act of 1976 which initiated the deregulation of the railroad industry. The latter was put in place to re-energize the slumping industry by introducing new regulations that would expand its opportunities. The Staggers Rail Act allowed the industry to dictate which routes to operate, rates to charge, and services to offer. This act ushered in a period of resurgence for the rail industry; rates decreased and freight volume rose, leading to the modern rail industry seen today [11].

Although the Staggers Rail Act of 1980 gave significant control back to the industry, Congress still retained the authority to protect shippers from unreasonable pricing and ensure that the industry acted with integrity. Following the implementation of the act, the railroad industry invested approximately $500 billion to establish a more secure and practical network. Since then, there has been a resurgence in freight transportation, leading to an increase in competition. In 2007 the Government Accountability Office reported to Congress that "the railroad industry is increasingly healthy and rail rates have generally declined since 1985" and "there is widespread consensus that the freight rail industry has benefitted from the Staggers Rail Act" [12]

In 2008, the Rail Safety Improvement Act was passed, which mandated that by 2015, Positive Train Control (PTC), a system of functional requirements to improve safety, must be implemented. PTC would effectively automate the yielding or stopping of a train in to lessen the accidents that are a result of human error which can include: train-to-train collisions, speed derailments, or traveling through switches that are in the incorrect position. In order to satisfy the accommodations listed, the railroad industry would have to invest an estimated $13.2 billion dollars. Unfortunately, from the outset of 2015, the original deadline proved to be arbitrary and unworkable, which was compounded by various technical and legal complexities. In response to outcries from the Railroad Industry, Congress passed the Surface Transportation Extension Act of 2015, which provided a three year extension for the installation of PTC [13].

1.2 The Technological Shift towards Onboard Health Monitoring

In the rail industry, it is common knowledge that overworked suspension elements can be detected by monitoring the health of bearings. A majority of diagnostic information can be found by gathering the temperature, load, and vibration states of the bearing. However, despite this

knowledge, the currently accepted method is found in different varieties of wayside detectors. These non-contact devices are set along the side of the track, and depending on which type of detector, can measure acoustic or infrared emission properties of the bearings that travel by the system. The Federal Railroad Administration (FRA) has claimed that wayside detectors enhance and supplement existing manual inspection procedures to facilitate early detection of rail defects [14].

The infrared wayside detectors, termed "Hot-Box Detectors," seen in Figure 3, are used to flag a bearing if the temperature becomes greater than 170°F (94.4°C) above the ambient temperature. The temperature of the bearing is typically associated with being a direct indication of the health of the bearing. Although this method does not find the root cause of the problem, it does provide a warning signal as to when the bearing should be closely monitored or removed. These devices employ two infrared "eyes" that sit on each side of the track positioned so that the train's bearings will pass above them. Recent improvements have the system instead flag bearings that have an operating temperature above the comprehensive temperatures of the aggregation of the bearings. Once flagged as a "trending" bearing, the entire axle assembly is removed and replaced. This process requires the train conductors to pull over and employ workers to manually remove the axle in question, which is then sent for a complete disassembly and examination to determine the cause of the bearing temperature increase. Hot-Box Detectors (HBDs) are currently set in 15 to 30 mile increments, placing a limitation on the quantity of temperature data received for each railcar [15].

During operation, however, even a relatively healthy bearing can experience fluctuations in operating temperature. These fluctuations, even when exhibiting behavior similar to that of temperature trending, are not entirely indicative of a bearing in distress or that approaching

catastrophic failure. Most currently utilized monitoring systems are unable to provide accurate predictions of the impending life of the bearing, which can be due to a number of factors such as: the device setup, the targeted area of the bearing where the temperature measurement is taken, the bearing cup discoloration which affects its emissivity, and the weather conditions that can affect the wayside detection systems. According to data collected by Amsted Rail from 2001 to 2007, "an average of nearly 40% of bearing removals are non-verified. A non-verified bearing is one that, upon disassembly and inspection, is found not to exhibit any of the commonly documented causes of bearing failure such as spalling, water contamination, loose bearings, broken components, lack of lubrication, damaged seals, etc." [16]. A more reliable and efficient monitoring system would prevent the costly delays resulting from unnecessary train stoppages and premature removal of healthy bearings. Therefore, due to its shortcomings, the current method of wayside detection fails to precisely identify the onset of bearing failure and accurately predict the bearing health. With freight volumes expected to increase over the next three decades, major consequences could arise if a more reliable bearing condition monitoring system is not implemented.

There has also been limited research into the employment of load sensing wayside detectors. In 2005, Nenov et al. [17] published works regarding a procedure used to measure the load experienced by the wheels of a moving railcar. A pair of strain gauges were affixed along the rail in the direction of travel. The data obtained was processed through an algorithm that would average the two strain gauge voltages and correlate that value to an estimated load. Problems arose during the analog-to-digital conversion of the signals which was later resolved by utilizing a compensating value which allowed the linear relationship of the signals to remain intact. Despite the initial promising results, implementation of the technique as a complete health

monitoring device was impractical due to the inefficiency of setting these devices in short mileage intervals.

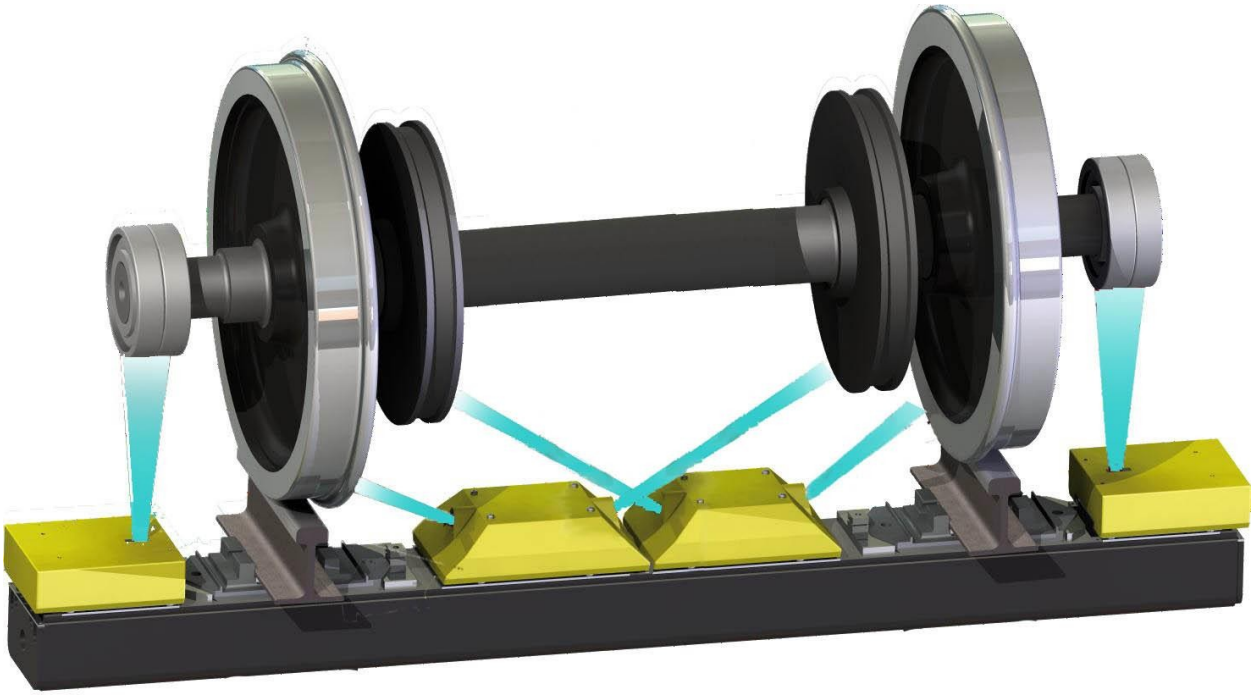

Figure 3. Depiction of Hot-Box Detector (HBD) [18]

The aforementioned limitations of the employed detectors has led to the development of what have been termed “smart products,” which continuously monitor various properties of the system. One of the first milestones in the development of onboard monitoring that occurred before the implementation of wayside detectors was the conception of the SmartBolt ™. This system consists of a thermal sensor/actuator connected to a piston and power supply in the form of an endcap bolt. It was initially proposed in 1990 to actively monitor the internal temperatures of the component of the bearing with the least heat resistance; the seal. Once the seal temperature reached 250°F (approximately 121°C), a signal would be transmitted to the train operator. Despite its potential, this product had a significant drawback; it could not detect sudden increases in temperature. Additionally, outside of a physical inspection, there was no means of resetting

the device once the threshold temperature was reached. There were consequently numerous time delays and costly product replacements [19].

Another such example is the onboard Wireless Sensor Node (WSN), which has the capability to continuously monitor temperature and send the results to a localized computer onboard the railcar, termed the Central Monitoring Unit (CMU). The CMU can then send information wirelessly by satellite or cellular network and inform the conductor to take preventative actions to avoid any possible derailment or safety issues [20]. The WSN has the ability to: maintain process tolerances, detect maintenance requirements, prevent catastrophic failures, and request maintenance based on a prediction of failure [21].

Another smart product that has been developed is the Timken "Guardian Bearing ™," which has the capability to measure both the temperature and vibration of the bearing assembly and is considered an ideal tool for condition monitoring and preventative maintenance. The sensors have the resolution necessary to diagnose wheel and bearing failure, along with stuck hand brakes, which are a major factor in the overheating of railcar rolling elements [22]. The Guardian Bearing is self-powered and has an internal microprocessor and radio transmitter, which can decipher the data received from the sensors and transmit the results wirelessly. The main drawback from this design is the monetary cost that accompanies the fulfillment of the Guardian Bearing's potential. Assuming that the system is able to effectively detect a potential failure, the complete axle assembly must be removed and inspected thoroughly, which does not allow the railcar owner the option to reuse any of the suspension elements, including the Guardian Bearing [23].

The majority of rail companies believe that bearing monitoring is essential to the preservation of the industry. As a result of federal regulation, however, onboard health

monitoring systems remain in their infancy. The ideal system for bearing health monitoring would include vibration, temperature, and load sensing capabilities. Vibration monitoring has the ability to detect the onset of spall initiation and track its growth with service life, temperature monitoring is perceived to detect impending catastrophic failure, and load monitoring can help detect potential overloads or shifts in bearing loading, the effects of which, would only be evident in the vibration and temperature data at later times. Currently, temperature can be measured by most sensing units, and only a handful have the capability of measuring vibration. The only onboard load sensing mechanism presently available to the industry involves mounting load cells to the bottom of the rail car above the center bowl, making maintenance to the system near impossible, and the load monitoring of individual bearings nonexistent [24].

1.3 Motivation for an Onboard Load Sensing Mechanism

The current methods of load measurement typically involve the use of weighbridges, as depicted by the blue section of rail in Figure 4. While railcars drive through a "rail-yard" or a specified section of track, companies will use computerized systems to determine the weight via large capacity load cells. The majority of weighbridges stipulate that the car either stop or travel at low speeds (around 6 mph or 10 km/h) [25]. In many cases, for the most accurate measurement, the cars will be uncoupled and weighed separately [26].Therefore, not only are the rail companies charged for this service, but a large portion of profit is lost in travel time [27]. The load information received from the weighbridge is taken and stored in a database and if the train is overloaded, the company will then be charged a fine to ensure that future railcars will transport the appropriate weight, providing safety to the track, suspension elements, and wheels. Unfortunately, weighbridges are even less frequent than hot-box detectors (HBDs), which limits their impact on the industry.

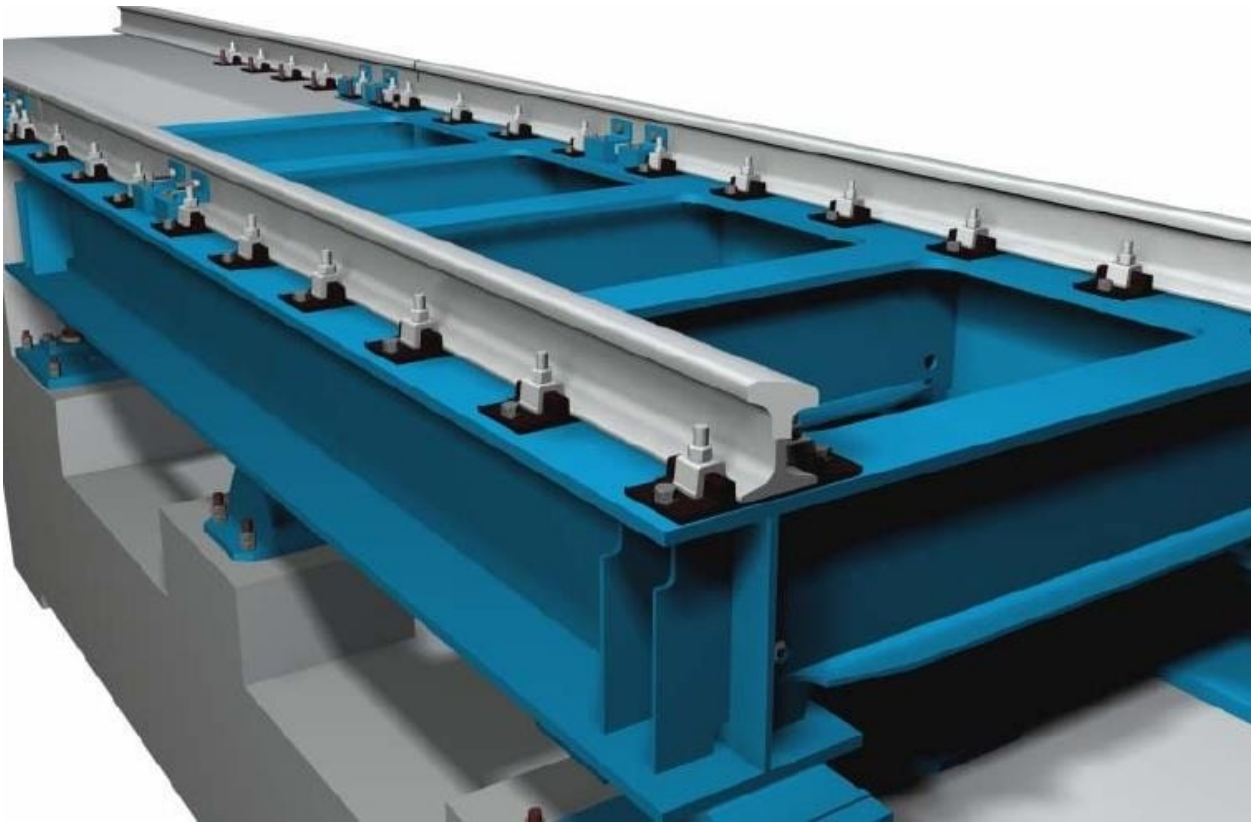

Figure 4. Depiction of a Railcar Weighbridge [28]

Due to the limitation in the current technology, there is a high demand for an onboard load monitoring system. The incorporation of load sensor readings along with temperature and vibration data can lead to promising developments in railcar safety operation management. Onboard load sensors embedded into each of the eight bearing adapters found in the two undercarriage-suspension (Figure 5) assemblies would allow for potential equal cargo distribution and will furthermore have the capability to give instantaneous developments to the train operator on how the freight has shifted throughout the travel period. Furthermore, it could benefit not only the consumer, but also the Association of American Railroads (AAR) and the Federal Railroad Administration (FRA) in their continuous search for improved safety protocols.

The rail industry would also like to improve upon the traditional method of filling a railcar up to a specified limit, known as volume loading. This crude method is typically employed when transporting cargo that has a constant density, such as with grain or hazardous chemicals, and will rarely fill the car up to the maximum load due to the human error involved in determining when to shut off the loading mechanism [25]. Finding a more precise and accurate method could effectively save the rail industry from large expenditures simply due to more efficient loading, while also protecting the rail track from overloading. By using an accurate onboard load sensor, once the combined weight felt by the eight bearings reaches 99% of the allowed load of a freight car, a signal could be output to cease filling, effectively loading each railcar to a safe and monetarily efficient weight.

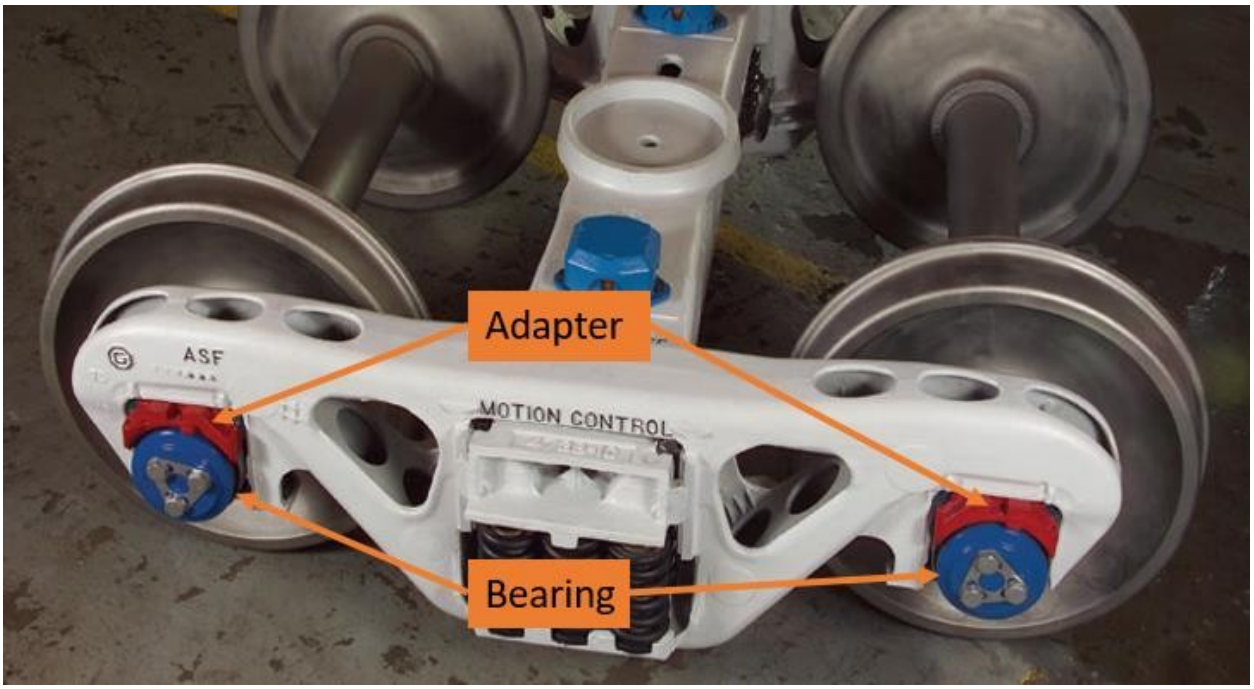

Figure 5. Undercarriage-Suspension Assembly [29]

The sensor would also be able to inform the railcar operator of any cargo that is lost or any leaks present in the railcar. The latter is crucial in the transport of liquid freight where in many

cases the cargo is hazardous and has the potential to result in costly damages to cities or the environment. When transporting crude oil, especially, an undetected leak in the tank car can initiate a derailment, which can result in huge financial losses due to fire damage, and in extreme cases, disastrous fatalities.

Another advantage of the implementation of the load sensor is the capability to incorporate this measurement into other aspects of the car, such as the braking system, shown in Figure 6. The application of the appropriate braking pressure is crucial to the sustainability of both the railcar and track. If the wrong amount is applied, then wheel flats can develop, which can lead to damages to the railcar and track. The rail industry has put into effect Wheel Impact Load Detectors (WILDs) to account for this serious problem.

The current braking system on conventional freight railcars involves the use of a double brake cylinder, as depicted in Figure 7, with compressed air acting on the large cylinder if the railcar is loaded and the smaller cylinder if the railcar is unloaded (estimated at 17% of full-load) by using what is termed an "empty load device" [30]. This braking method can easily over- or under-estimate the appropriate amount of pressure. For passenger trains, however, a proportional braking system is used, which receives an input from the deflection of the suspension springs and is then used to calculate and apply the appropriate amount of pressure [31]. Taking inspiration from the passenger train, a highly accurate proportional braking control system which utilizes the load sensor's accuracy to apply the appropriate amount of braking pressure needed to subdue the momentum of the railcar could be designed. The implementation of such a process would help prevent the development of wheel flats on trains and result in extended track and railcar service life.

Figure 6. Depiction of Rail Braking System [30]

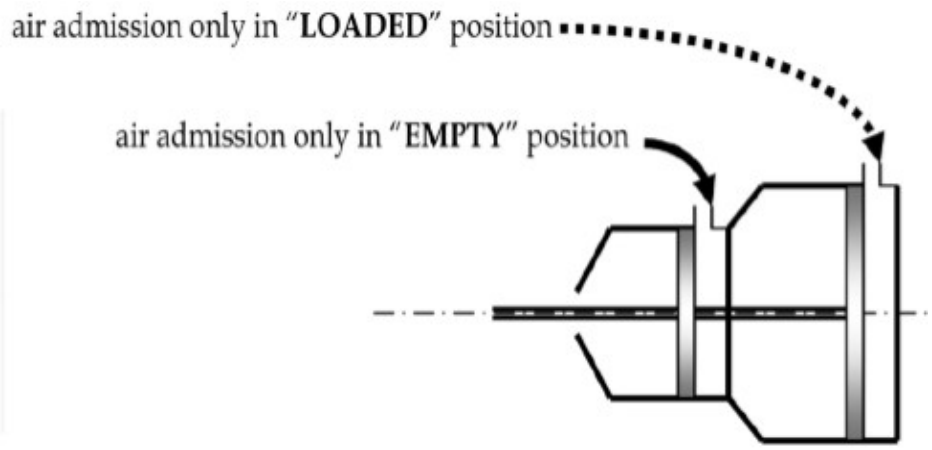

Figure 7. Double Brake Cylinder [25]

1.4 Sensor Requirements

The design qualifications require that the sensor be capable of elastically deforming with a load ranging from 5,850 lb_f (26 kN) to 34,400 lb_f (153 kN), the estimated unloaded (empty) and fully-loaded weights, respectively, of a railcar bearing (the total weight of a railcar can be calculated by multiplying these values by eight). The sensor would need to survive impact forces and transmit a signal that is unaffected by these extreme forces. It would additionally need to

have the capability to be functional with bearings that have developed spalls or other defects, and output a signal that is unimpeded by the resulting vibrations.

The sensor insert would also need to incorporate temperature sensors that have the capability to detect extreme bearing operating temperatures, i.e., -40°F to 300°F (-40°C to 150°C). The temperatures around the circumference of the bearing vary, but the highest temperature will typically be observed at the region of load application, and consequently the lowest temperature will be seen at the opposite end. These sensors would need to be placed at the top, where the load is being applied, near the center of the inboard and outboard raceway portions of the adapter to estimate the highest temperature region of the bearing.

Figure 8. Unmodified Adapter-Pad Assembly [32]

The thermoplastic polyurethane (TPU) steering pad, shown in Figure 8 (blue component that sits on top of bearing adapter), is used to prevent metal-to-metal contact in the suspension system of a freight railcar. In other words, it is meant to act as a compliant member that will reduce the frictional forces involved when the railcar navigates turns. This TPU steering pad

results in reduced wear on wheel flanges and reduced loads on each of the suspension elements [32], however, it also poses an issue for the proposed load sensor. The steering pad adds an element of creep, which creates a time-dependent logarithmic signal when a step load is input. It is theorized that incorporating temperature into the load correlation will allow a suitable relation to account for the flow of the TPU. This creep must additionally be taken into account when analyzing the effectiveness and reliability of the developed load sensor.

1.5 Continuing Towards Safer Railways

This thesis builds upon the extensive work by Ley [3], Saenz [33], and Diedrich [25] from the University of Texas Rio Grande Valley (formerly the University of Texas-Pan American), who systematically explored the best path towards creating an onboard load sensor that has the capability to survive the most extreme environments that railcars are subjected to, as well as, providing reliable and consistent data collection. Diedrich [25] was able to further refine the previous work by creating a second-order correlation that accompanies the sensor insert prototype which is embedded between the adapter and steering pad, as displayed in Figure 9. The bearing adapter was machined in such a way that allows the prototype to be placed in a groove and slightly protrude above the top of the adapter surface. However, it was left “free floating” and was not mounted to the adapter in any way. This process gave the sensor the ability to resist the movement induced by oscillatory events while consistently maintaining load detection, but prevented it from obtaining precise results.

The work done for this thesis study differs from earlier works in that:

(1) It will further improve upon the accuracy, reliability, and repeatability of the previous work by incorporating a multivariate correlation into the load sensor network.

(2) It will provide a correlation that can be implemented for freight car loading scenarios that can effectively display the instantaneous loading of a railcar.

(3) It will account for the structural reliability of the developed sensor under extreme field service operating conditions.

(4) It will demonstrate a real-life deployment simulation, in which a pre-test, calibrated sensor will be evaluated for its ability to detect subtle changes in railcar loads.

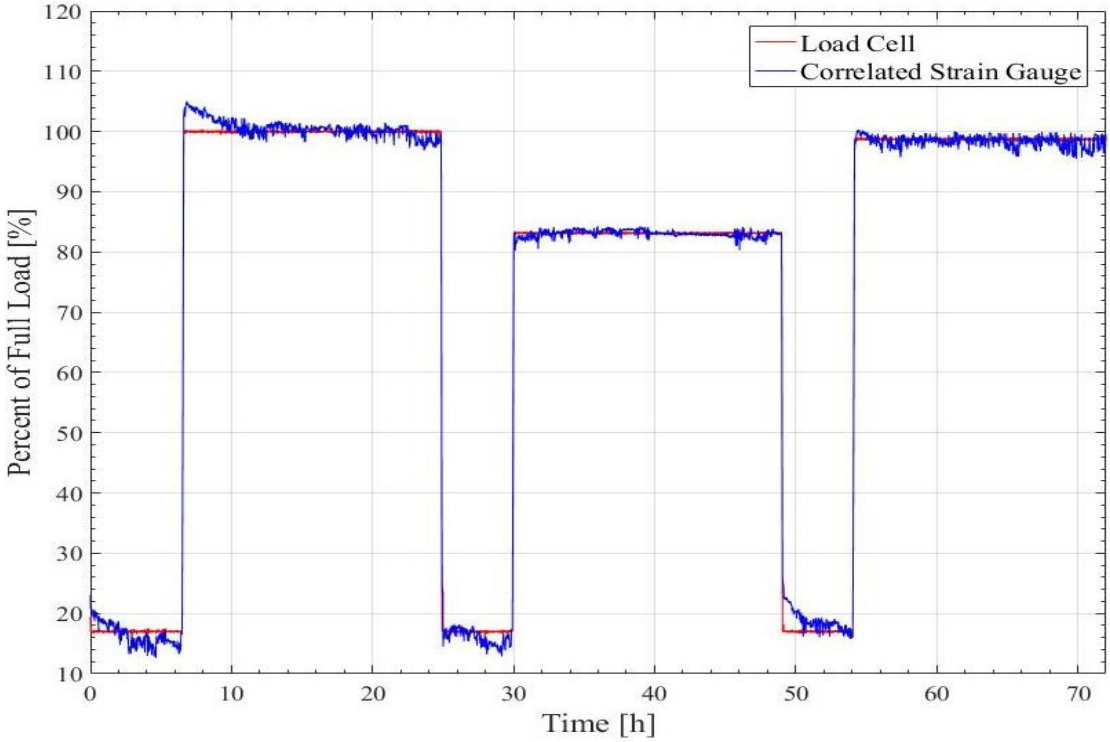

Figure 9. Previous Testing Conducted by Diedrich [25]

In Chapter II, a detailed description of the experimental setup and instrumentation is given. Chapter III explains the procedure followed to correlate the load cell voltage and analog temperature readings to the actual load measured by a calibrated load cell. In addition, a ramping test and corresponding correlation are acquired which will allow the operator to accurately determine at what point a loading system should be shut off during the filling process. In Chapter

IV, impact and reliability tests are performed, evaluating the survivability and long term performance of the load sensor prototype. Finally, Chapter V provides details and recommendations for future work that is needed to take this prototype to full production.

The ultimate goal of the Railroad Research Group at the University of Texas Rio Grande Valley is to incorporate the three main diagnostic components of safety: vibration, load, and temperature, into a single adapter-mounted condition monitoring device. This device would have the capability to wirelessly send the data to an onboard electronic logic unit, which can perform the required analyses. Once this device is complete and in full production, any railcar that utilizes a Smart Adapter© will promote a safer tomorrow for the railways.

CHAPTER II

EXPERIMENTAL SETUP AND INSTRUMENTATION

The primary thrust of the experimentation discussed throughout this thesis is the implementation of a Smart Adapter©-based load insert that has the capability to provide accurate feedback of the applied load on a typical railroad bearing. This objective will be achieved by the use of an experimentally acquired multivariate correlation that incorporates a full-bridge strain gauge and two analog temperature sensors that are set to read the operating temperatures of the inboard and outboard raceways of the bearing. All the research that follows was conducted on Class K bearing-adapter assemblies with AdapterPlus™ thermoplastic polyurethane (TPU) steering pads. Two differing load cells and three differing signal conditioning boxes were used throughout the testing seen in Chapters III and IV, details of each of which will be provided and discussed in the following sections.

Each bearing class has a designated maximum service load seen by each component. The corresponding 100% load on a Class K bearing as stated by the Association of American Railroads (AAR) is equivalent to approximately 34,400 lb_f (153 kN) and the corresponding 17% load, or that representative of an unloaded (empty) railcar, is approximately 5,850 lb_f (26 kN). These reference loads are used throughout the optimization analysis conducted in this thesis and

should be noted. The principles of testing in the following sections can be applied to any railroad bearing class, and the experimental setup and signal processing readily repeated.

2.1 Initial Development of the Load Insert

Various methods of load sensing were explored by Ley [3], including methods that utilized the polymer nature of the steering pad via microelectromechanical pressure sensors and piezoelectric sensors. Each of the advanced technologies that were examined presented significant drawbacks. As an outcome of the numerous trials and instrumentation that were explored, the strain gauge was chosen for the load measuring system due to its accuracy and ease of incorporation into the Smart Adapter© assembly. Through the proof of concept and improvement of design carried out by Saenz [33] and Diedrich [25], a simplistic and reliable load sensor was developed which had the necessary durability to survive the harsh environments that railcar bearings are exposed to in field service. However, with this type of load sensor, the creep from the TPU steering pad detrimentally affects the raw voltage output. While Diedrich [25] was able to improve upon the correlation and design of the sensor created by Saenz [33], there was still a significant error in the load measurements for static testing. It is theorized that by incorporating the bearing raceway operating temperatures, the relationship between the creep of the polymer pad and the pressure distribution can be estimated, and correlations can be devised that are accurate for both dynamic and static application scenarios.

2.2 Laboratory Setup

2.2.1 Bearing Nomenclature and Sensor Setup

The double-tapered roller bearing is the standard bearing of the railroad freight industry. The dimensions of these bearings differ depending on the global market and the specifications and regulations imposed by the governing bodies for the various international rail companies. . The type of bearing utilized for this study is categorized as a Class K bearing and is part of Generation 2000, which are higher quality bearings used to "prevent excessive axle deflections that lead to fretting, back face wear, and loose components." The Generation 2000 railroad bearings utilize hardened steel components in the inboard contact areas to provide additional fretting performance benefits [34].

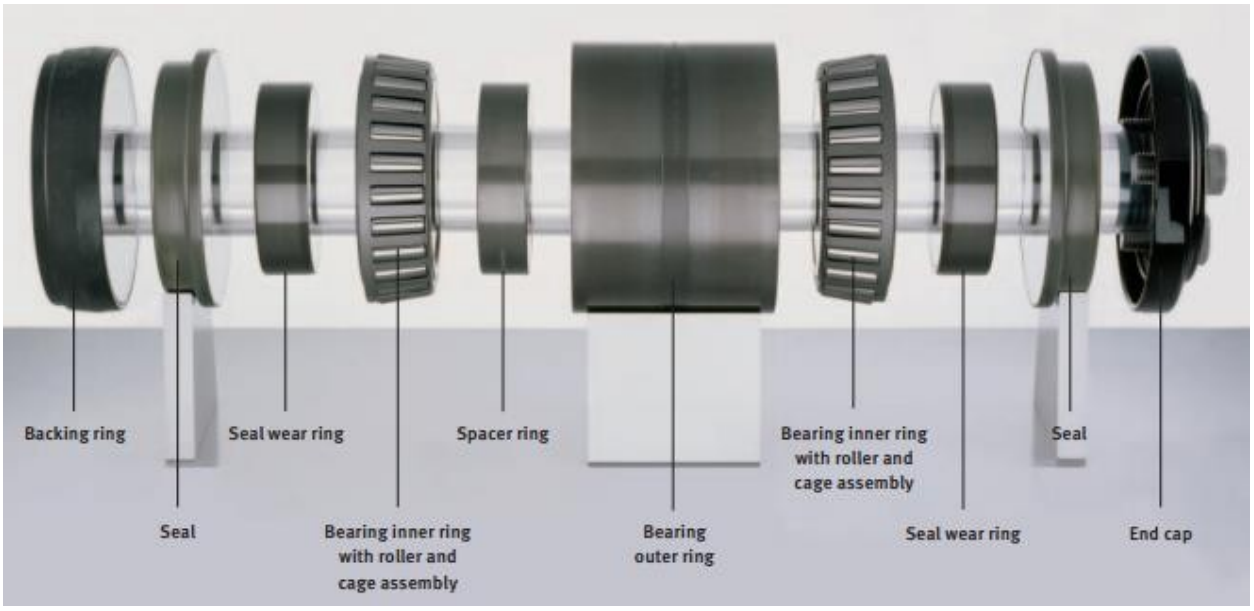

Figure 10. Basic Components of a Railroad Bearing [35]

Double-tapered roller bearings have several unique mechanical design aspects. The two ends of each roller have different diameters which results in a large area of contact and gives the component the capability to withstand large axial and radial loads. The component which

provides the inner raceways in which these rollers operate is known as the “cone” or “inner ring”, while that which provides the outer raceway for the rollers and encompasses the assembly is known as the “cup” or the “outer ring,” as shown in Figure 10. The rollers are separated by a cage, which ensures they are kept a fixed distance apart, guaranteeing smooth operation and even load distribution. The cages used in the experiments that follow were made of polyamide to account for the thermal expansion that occurs during operation. Flanges present on the cone actively prevent the roller-cage assembly from leaving the bearing raceways at high speeds. Spalling, one of the primary defect modes of bearings, can occur on the cup, cone, or individual rollers.

The primary objective of the Smart Adapter© is to incorporate vibration, load, and temperature sensing capabilities for a complete bearing health monitoring system. Two of these three parameters are included in the load sensor assembly, where a strain gauge and two analog temperature sensors are embedded in-between the AdapterPlus™ steering pad and the steel bearing adapter. The aim of this product is to contain a wireless unit recording and reporting the sensor outputs to an onboard electronic logic unit, which can then proceed to run the analysis algorithms and transmit the results and data elsewhere by satellite or cellular network, which eliminates the need for large battery life and complex circuitry to be located on the adapter-bearing assembly itself. The latter would also ensure that if any bearing-related issues arise, there is sufficient time to take preventative action rather than a reactive one. There are a total of eight AdapterPlus™ assemblies in a single freight railcar. To reach the full potential of the load insert, each of the eight bearings typical of a railcar assembly must be equipped with a Smart Adapter© in order to completely monitor the loads and temperatures seen by each bearing, as well as, produce an immediate response for any possible load imbalances, shifts, or leaks during travel

periods. The total load of the freight railcar will be obtained by adding the loads measured by all eight load sensors.

The crucial aspect to the success of the Smart Adapter© load insert lies in the positioning of the sensors. For the most accurate measurements, the load sensor must be placed directly in the path of the applied load. The load travels through the region of application on the steering pad to the steel adapter and further to the bearing and wheelset. By placing the sensor directly between the steering pad and Smart Adapter©, the portion of the load seen by the bearing can be detected by the sensor. However, the issue then becomes the pressure distribution across the polymer steering pad that arises from the imposed forces. Similarly, to obtain the most accurate results, the temperature sensors need to be placed directly above the center of the inboard and outboard raceways and as near to the bearing as possible to ensure that there is optimal heat transfer to the sensors with minimal thermal lag.

2.2.2 Single Bearing Test Rig

The experiments that follow have been conducted on a Single Bearing Test Rig, depicted in Figure 11. This particular type of rig has numerous capabilities, making it the favorable laboratory test rig for conducting controlled experiments for the load insert. It has the ability to simulate numerous conditions a railroad bearing employed in the field might experience, and allows for both static and dynamic testing with speeds varying from 5 mph to 85 mph. Additionally, the rig has the capability to simulate impacts, such as those caused by wheel flats or rail joints and defects, and lateral load, which results from a railcar navigating curved sections of the track. By utilizing this test rig, the angular speed of the bearing can accurately be simulated and incorporated in constructing a correlation for the load sensor and the effect of impacts on the survivability and signal output can be studied. As of this point no lateral load

studies have been performed in tandem with the load insert, but these might be highly beneficial in the future when simulating the shifting of cargo while entering turns.

The maximum load that a Class K bearing should experience during typical operation in the field is approximately 34,400 lb_f (153 kN). To simulate this loading condition, a hydraulic cylinder, along with what is designated the "load controller," were designed and fabricated at the University Transportation Center for Railway Safety (UTCRS) at UTRGV. An I-beam was used to distribute the load from the hydraulic cylinder piston across the adapter pad surface. Two different load cells were used throughout experimentation: a heavy duty load cell with a 100-kip (445 kN) capacity (Figure 12) and a rod-end load cell with a 50-kip (222 kN) capacity (Figure 13). Only the load accuracy testing described in Chapter III involved the use of the 100-kip (445 kN) load cell. All other tests were performed using the 50-kip (222 kN) rod-end load cell.

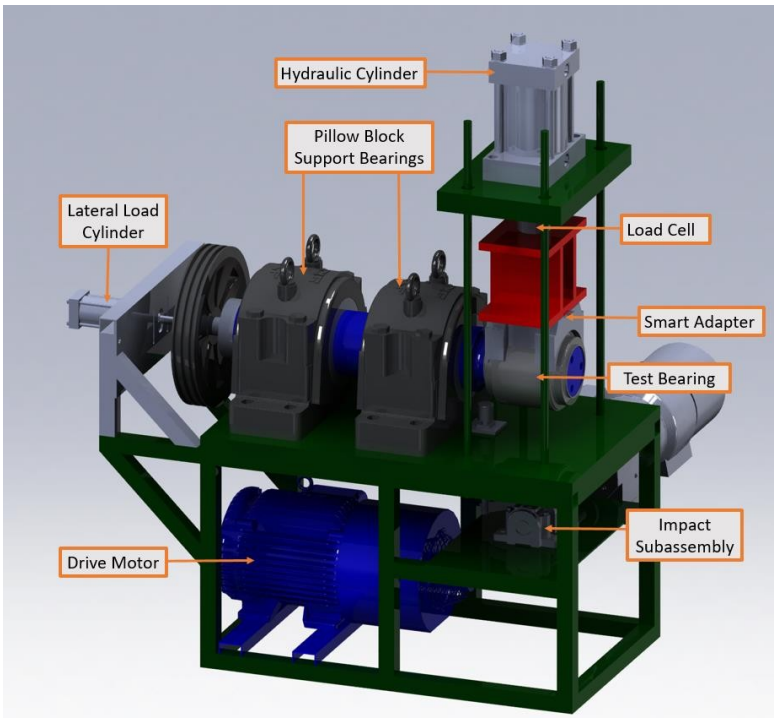

Figure 11. Single Bearing Test Rig

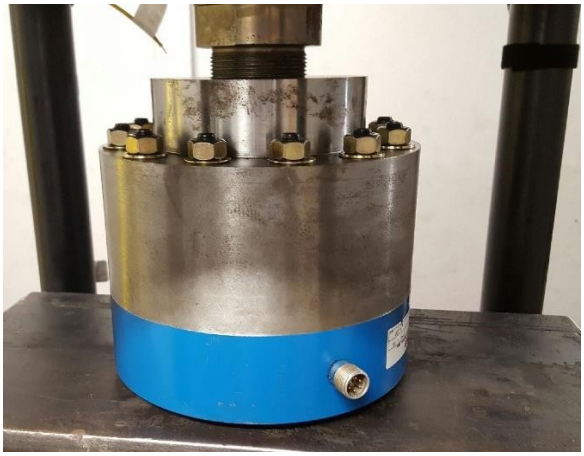

Figure 12. 100-kip Capacity Load Cell

Figure 13. 50-kip Capacity Rod-End Load Cell [36]

2.2.3 Data Acquisition System

The data that will be presented in Chapters III and IV was acquired by a National Instruments™ cDAQ-9474 USB chassis coupled with a NI 9205, 32 channel, ±10 Volt analog input module. A 50 Hz sampling rate was utilized to collect the data, which was post-processed with MATLAB™ with a moving average of 200 data points, which corresponds to four seconds worth of averaged data. The choice of this specific averaging window is intentional in order to align the load sensor data acquisition with that of the vibration sensor. A 5 Volt pulse signal was

sent to the motor controller using the analog output port of a NI USB-6211 DAQ to adjust the load setting, if necessary.

2.2.4 Load Controller

To initially set a target load, an Enerpac™ manual hydraulic pump is pumped until the appropriate voltage is output by the load cell. However, even though the hydraulic cylinder valve is securely closed after ensuring the target load is reached, temperature changes that occur during operation of the bearings induce thermal expansions of the fluid, which result in an increase in the force applied to the Smart Adapter© and consequently impede the ability of the test to accurately simulate a constant loaded railcar. Therefore, an additional method of controlling the pressure of the hydraulic cylinder was needed.

The ideal solution to this problem simply involves the capability to increase or decrease the quantity of hydraulic fluid in the cylinder by small amounts. Additionally, the pressure would need to be accounted for and the necessary alterations made, preferably through a feedback system. The solution developed to counter the effect of the thermal expansion of the hydraulic fluid was to use a 1-1/2 inch (38 mm) bore hydraulic cylinder to pump the small amounts of fluid into the system. The cylinder is driven by a linear actuator which transforms the rotational movement of a DC motor to translational movement through a threaded rod via a gearbox, as pictured in Figure 14. A computer equipped with the DAQ software LabVIEW™ was employed to provide the ability to run extremely detailed testing plans, which would enhance the accuracy of the sensor.

This system has the capability to regulate the load, defined by the load cell voltage, and determine whether the pressure should be increased or decreased by traveling through an error

loop. If the amount of error specified is exceeded, a pulse signal will be sent from the analog output of a DAQ to the motor controller until the force applied is within the specified tolerance. This system is capable of providing a steady, accurate load to within 100 lb_f (445 N), however, this proved problematic when conducting dynamic testing with axle rotation, as the load can fluctuate well beyond 100 lb_f (445 N) due to geometric raceway tolerances and, therefore, an error range of ±350 lb_f (1,560 N) was utilized. The system can additionally execute preprogrammed test plans that simulate loading cycles at varying rates and allows for testing to be conducted at all times of the day, which renders the system independent of human supervision. For simulation purposes, however, the axle rotation was stopped when loading or unloading the bearing in order to accurately mimic actual loading/unloading scenarios.

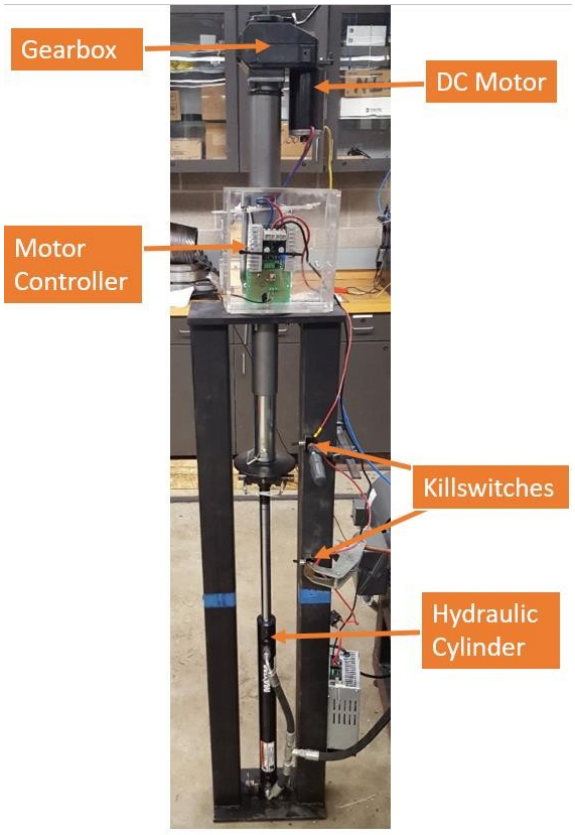

Figure 14. Load Controller Setup

2.3 Load Sensor Design

2.3.1 Strain Gauge

There are two types of load sensors: position monitors and strain detectors. Due to the inherent limitations, a position monitoring load sensor was deemed undesirable. Therefore, a temperature-compensated full-bridge strain gauge was selected. Strain gauge circuitry utilizes a Wheatstone Bridge Circuit. The strain gauge used in the tests that follow is a full-bridge, transducer class with a 350 Ohm nominal resistance and is manufactured by Micro Measurements™. The schematic of a full Wheatstone Bridge Circuit as well as the strain gauges implemented into the load sensor-constructs can be seen in Figure 15.

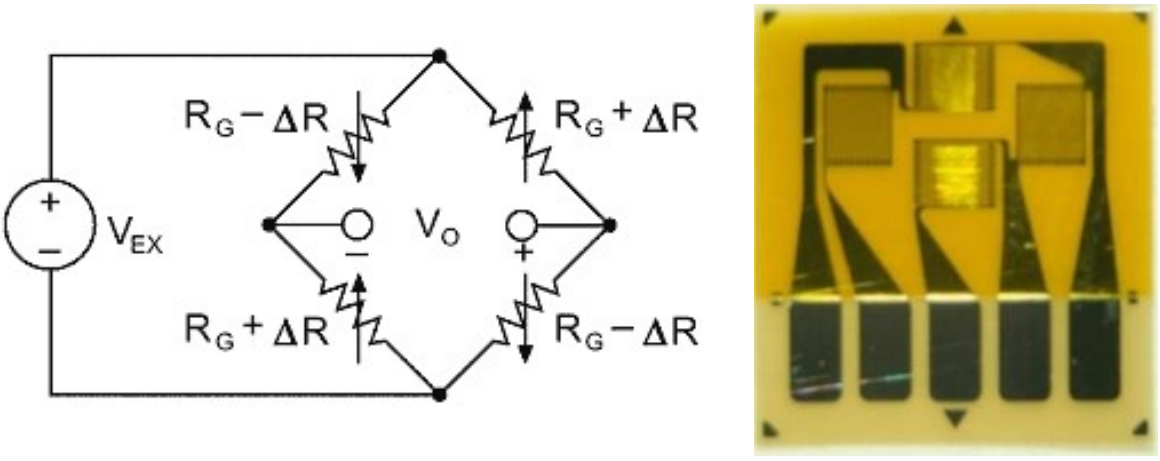

Figure 15. (Left) Wheatstone Bridge Circuit (Right) Strain Gauge [3]

A full-bridge strain gauge is made up of four individual resistors that will change resistance based upon the strain of the surface of the material to which the circuit is mounted. Two of the resistors are considered active or “axial” gauges that measure the strain experienced in the bending direction of the sensor and the remaining two act as temperature compensation or “transverse” gauges for the material and are meant to eliminate any signal changes that occur due to the thermal expansion of the wiring. The transverse gauges are aligned with the neutral or

non-bending axis of the sensor insert. Temperature compensation works by subtracting the voltage potential change due to temperature shifts in the transverse gauges from the output of the active gauges so that only changes due to actual deformation are detected [37]. Although the employed strain gauge is temperature compensating, the temperature-dependent creep quality of the polymer pad has a significant effect on the sensor output.

2.3.2 Flex Circuit

The flex circuit was designed to provide the necessary wiring to the load insert. The design of the insert created numerous constraints that made the flex circuit a suitable choice that would ensure functionality and reliability. It gives the unique ability of the wiring to be located throughout a flexible sheet and provides a secure location for the two analog temperature sensors, which are surface mounted parts and require copper pads to be placed for the sensors to be soldered. Despite its thin appearance, the flex circuit requires a certain amount of clearance between the top and bottom pieces of the insert to ensure safety from damage that can result from the fluctuating loads typical of railroad bearing service operation [25]. It is recommended that, in final production, the entirety of the flex circuit be housed as it is not mechanically resistant to axial forces.

2.3.3 Development of Final Design

The previous insert design, developed by Saenz [33], was located in the middle of the bearing adapter due to the pressure film analysis that was performed and was further able to produce semi-accurate results during a static test. The data, however, required a more practical correlation due to the characteristic logarithmic increase in the sensor voltage output over time. Saenz [33] believed that this logarithmic trend can be attributed to the creep of the thermoplastic

polyurethane steering pad, which would give the appearance of an increase in load despite the constant force applied to the bearing. It was observed through the various laboratory tests outlined in his thesis that the sensor designed by Saenz [33] was inaccurate at loads below 50% of the simulated full-load of a railcar. The 70-100% loads where the sensor was accurate, however, would be able to warn train operators of overloaded bearings and was a suitable first step design. Although the design met the basic requirement for accuracy at loads ranging from 70 to 100% of the full-load (24,080-34,400 lb_f or 107-153 kN), a sensor capable of measuring the full range load a railcar bearing is subjected to, including the unloaded weight (17% of full-load), is preferred and would open the possibility for a sensor that not only has the capability to be used during travel periods, but additionally, when the railcar is being loaded with cargo.

The sensor redesign carried out by Diedrich [25] allowed for numerous improvements to the insert including: a slight adjustment in temperature sensor placement, optimization of machining time, and reduction in the raw materials necessary for assembly. The temperature sensors were a critical issue, with necessary slots being machined to place the temperature sensor as near to the adapter surface as possible. The new optimized length of the sensor was 4.15 inches (105 mm) compared to the previous 5 inch (127 mm) design. The shorter length resulted in reduced machining time that is necessary to alter the steel adapter for inclusion of the sensor insert by effectively shortening the length of the sensor canal.

Once the top and bottom components are machined, the load insert can be assembled, as shown in Figure 16 and Figure 17. The flex circuit is aligned with the machined dowel pins in the lower component and adhered in place. The strain gauge, mounted on the upper component, is soldered to the flex circuit, and the entire assembly can then be welded together. In order to weld the upper and lower components, an aluminum heat sink is needed to ensure that the heat

from the welding process does not damage the flex circuit or sensors housed in the insert. Great care was taken to ensure that when constructing each sensor, the strain gauge was placed with a similar orientation, so as to limit the human error involved in future results. Despite the cautionary assembly, different voltages are output by the sensors under similar loading conditions.

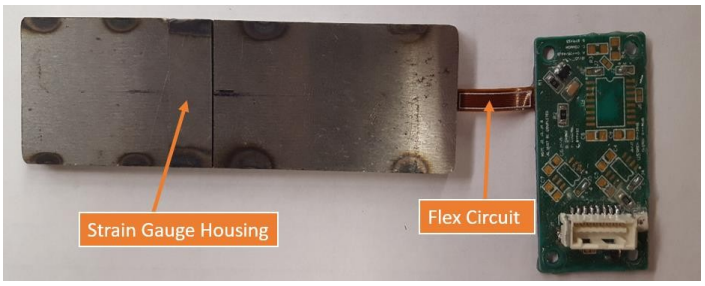

Figure 16. Load Insert (Top View)

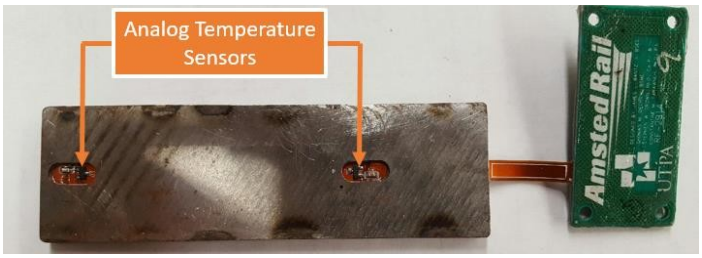

Figure 17. Load Insert (Bottom View)

The steel adapter had to undergo a series of machining processes to implement the necessary features for the insert, as shown Figure 18. A canal was machined where the insert would be placed, and mounting locations were machined for the circuitry port of the sensor. Eight individual Smart Adapter© assemblies were machined and fabricated, however, for brevity, only four of those assemblies will be examined throughout the various tests performed in Chapters III and IV. These four adapters will be referred to as Adapters A, B, C, and D.

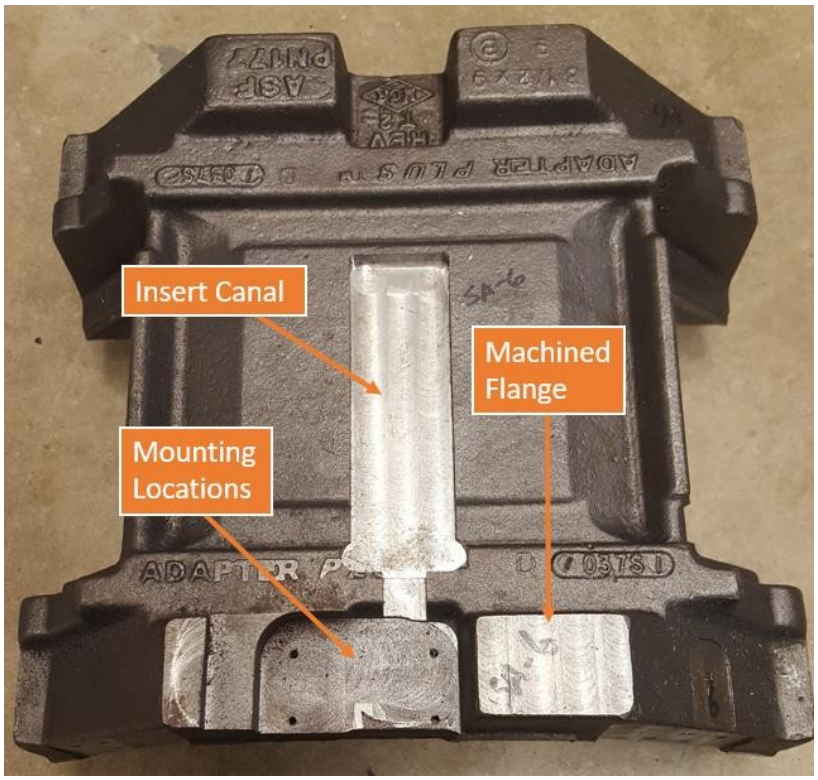

Figure 18. Steel Adapter Machined for Load Insert Capability

2.4 Load and Temperature Signal Conditioning

The original design of amplification circuitry, completed by James Bantz III, a former electrical engineering graduate research assistant, needed to account for the eight Smart Adapter© sensors that would be seen on one freight railcar during field testing. Therefore, a "signal conditioning box" was designed that had the capability to carry out the load amplification necessary for four sensors. For field testing purposes, two boxes would be used: one in the front compartment of the railcar and one in the back compartment, which would consequently ensure that eight load signals and sixteen analog temperature signals would be recorded simultaneously during the testing period.

Due to the transition of this project from one funded by Amsted Rail to one funded by the University Transportation Center for Railway Safety (UTCRS) at the University of Texas Rio Grande Valley, there was no need to incorporate the four separate load and temperature signals typical of a field test. Due to the current capabilities of the single bearing test rig, it was decided that one load and two temperature signals would be sufficient. Therefore, a redesign was carried out by Gerika Prado, an electrical engineering graduate research assistant, who compacted the previous design into a circuit that would incorporate one load signal, two analog temperature signals, and four accelerometer signals. This redesign eliminated unnecessary components and optimized the board size necessary for the circuitry. In each testing description, emphasis will be placed upon which signal conditioning box was used. The three boxes used will be designated as: B-1, B-2, and P-1, the last initial of the designer followed by a numeral. The schematics for each board as well as the data sheets for the electrical components can be found in Appendix F.

2.4.1 Schematics

The initial signal conditioning box schematic as well as the components selection was created and carried out by James Bantz III. Once the initial schematic was drafted, it was transferred to DipTrace™, a printed circuit board design software. Through this program, a simplistic schematic was created which could be transferred to a company for board production. The original signal conditioning box ran the load signal through a circuit with a gain of 400 and contained the capability to measure four load signals and eight temperature signals simultaneously. The box additionally incorporated a capacitor, which allowed for manipulation of the filter cutoff frequency.

The simplification of this design was carried out by Gerika Prado. To mimic the original output of the circuitry for comparison, the redesigned signal conditioning box incorporated a

gain of 400. The design by Prado has the capability to measure one load signal and two temperature signals, however, it also allows for the incorporation of four vibration sensors. Additionally, to incorporate adjustable cutoff frequency components, a potentiometer was added to the circuitry. This board is purposed specifically for laboratory testing. If a field test were to be conducted, a new board would need to be produced which could account for the necessary amount of inputs. The redesigned load and temperature circuits are displayed in Figure 19 and Figure 20.

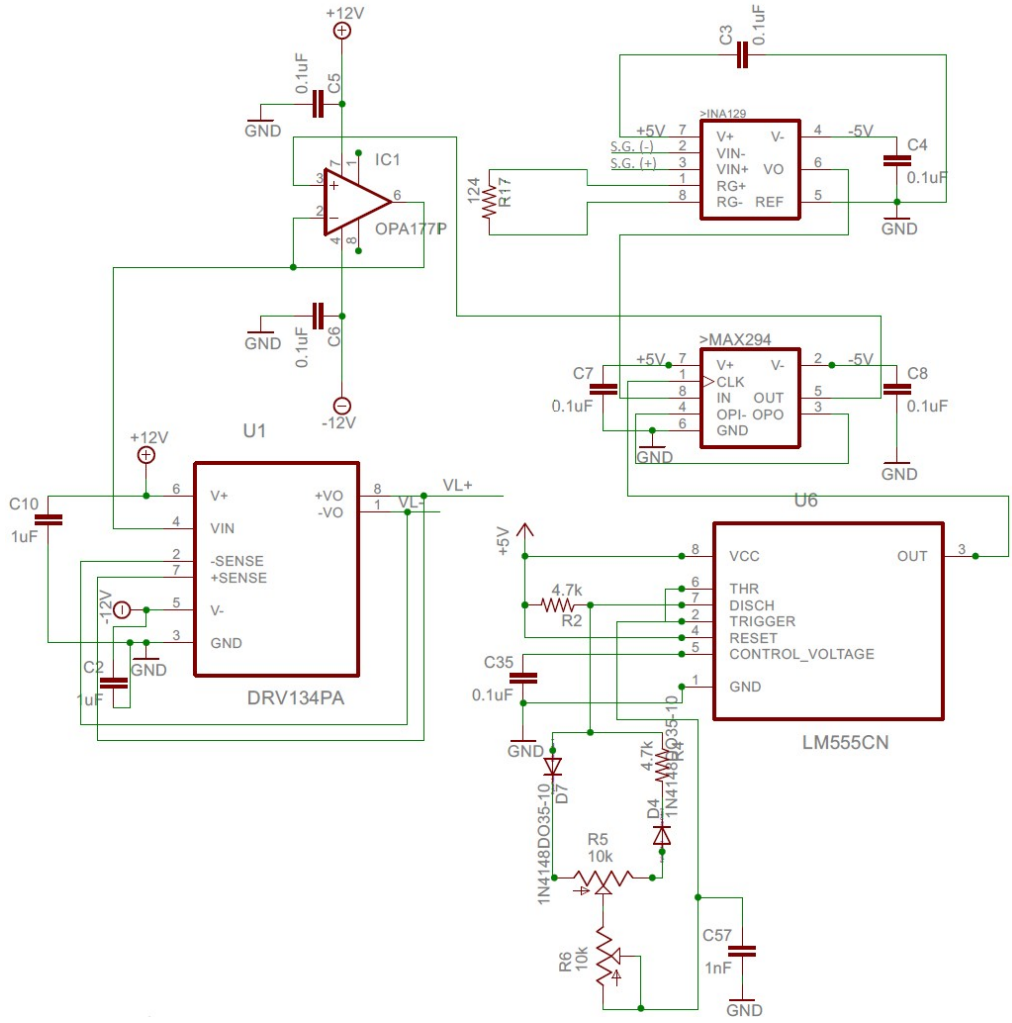

Figure 19. Redesign of Load Circuitry

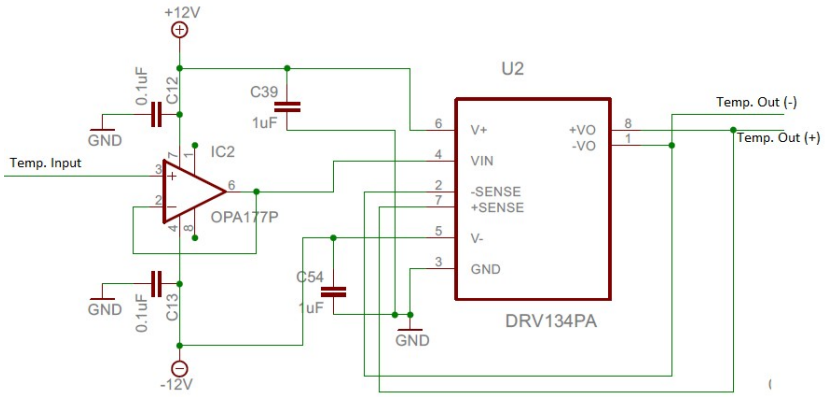

Figure 20. Redesign of Temperature Circuitry

2.4.2 Amplifier

The output voltage of the strain gauge is on the order of millivolts. To generate a suitable signal in the range of 3-10 V, it was necessary to amplify the very small output of the strain gauge. For the past and current designs of the circuitry box, an INA 129 instrumentation amplifier produced by Texas Instruments (Figure 21) was integrated into the signal conditioning box design. This component is a low power, yet high accuracy amplifier that harbors adjustable gain by means of a single resistor and has the capability to reach a maximum gain of 600.

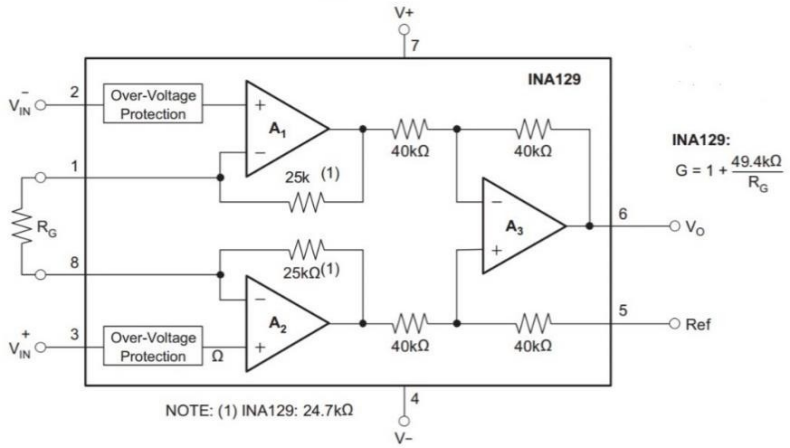

Figure 21. INA 129 Amplifier Schematic

2.4.3 Filter

The testing environment in which the sensor is deployed is vulnerable to noise from the variable frequency drive which controls the motor rotation of the test rig. After the amplification of the output of the sensor, this noise must be filtered from the signal. The MAX 294 8^{th} order, low pass filter designed by Maxim Integrated Products Inc. was used to filter out the electronic noise on both signal conditioning boards and consequently removed any 60 Hz interference in the signal that is produced as a result of the testing environment.

The adjustable cutoff frequency of the filter can be set by one of two ways. The first involves placing a capacitor of a designated value on the corresponding pin signified by the datasheet of the filter. The second is by applying a clock frequency to the clock pin of the amplifier. The primary benefit of using the capacitor method to set the cutoff frequency lies in simplicity of switching one component, however, this will detrimentally lock the cutoff frequency at a set value. By utilizing a clock frequency produced by a microcontroller, the cutoff frequency can be altered easily by reprogramming the microcontroller. For the purposes of laboratory testing, however, a cutoff frequency of 60 Hz is optimal and the capacitor method is suitable, despite its permanency. For the redesign of the signal conditioning box conducted by Prado, an external oscillator was used to filter the signal. A '555' timer creates a pulse waveform and is controlled by a potentiometer, which allows alteration of the cutoff frequency.

The final design of the load sensor will involve its incorporation alongside accelerometers and battery power. A thorough analysis of the final integrated circuit and the noise experienced in the field would need to be conducted. From previous field testing analysis conducted by Gonzalez [38], there was a significant amount of 0-100 Hz noise in train operation, which could affect the signal of the load sensor. Therefore, it is recommended that, for the final

integration of both the load and vibration elements, the necessity of this component be analyzed and eliminated if necessary.

2.4.4 Line Driver

The line driver was originally implemented for the sole purpose of having the capability to collect accurate data during field testing. With the load insert fixed to the Smart Adapter©, the signal output must be sent to the instrumentation car, which is typically located ahead of the freight car for the duration of a field test. A typical railcar is over 60 feet long, therefore, the signal conditioning box must ensure that the output of the sensor can be transmitted through a maximum of 80 feet of cable to the data acquisition system located within the instrumentation car.

The primary function of the line driver is to improve the strength of the signal throughout the length of the cable in an effort to discourage voltage drops typical of signals traveling through long lengths of cable. The DRV 134 line driver produced by Texas Instruments™ was selected as the best choice for circuit integration, which is a differential output amplifier that converts a single-ended input to a balanced output pair. Because the line driver requires a high current signal to the integrated circuit, an operational amplifier, OPA 177 from Texas Instruments™, was used to buffer the voltage to provide the required current. These components were included in the signal conditioning redesign by Prado.

2.4.5 Characterization of Circuitry Voltage Offset

When alternating the signal conditioning boxes in preparation for a field test, it was discovered that simple inconsistencies in the board resulted in a difference in the output voltage from the signal conditioning box. When analyzing the data to devise a correlation, it was found

that there was a difference in the “fully-loaded” reading of the strain gauge, where the output voltage differed by approximately 0.3 V. This error would consequently affect the final product if different signal conditioning boards were used in calibration and implementation. If each board represented a different unknown offset, the integrity of the final product would be diminished.

To ensure that a voltage difference was present, a test was devised where the strain gauge signal of Adapter D was sent to the signal conditioning boards of both Bantz and Prado simultaneously (B-1 and P-1). The output voltages were collected and recorded by LabVIEW™, and it was determined there was a significant difference between the two signals throughout the short testing period. The overview of this test is displayed in Figure 22, which shows the load experienced by the bearing-adapter assembly throughout the testing period. Figure 23 displays the raw voltage outputs of the circuitry boxes and Figure 24 displays the difference between the signals throughout the testing period. It can be seen that there is a fairly constant offset between the signal conditioning board outputs. These results encouraged a characterization test to determine the inherent offsets in each of the boxes.

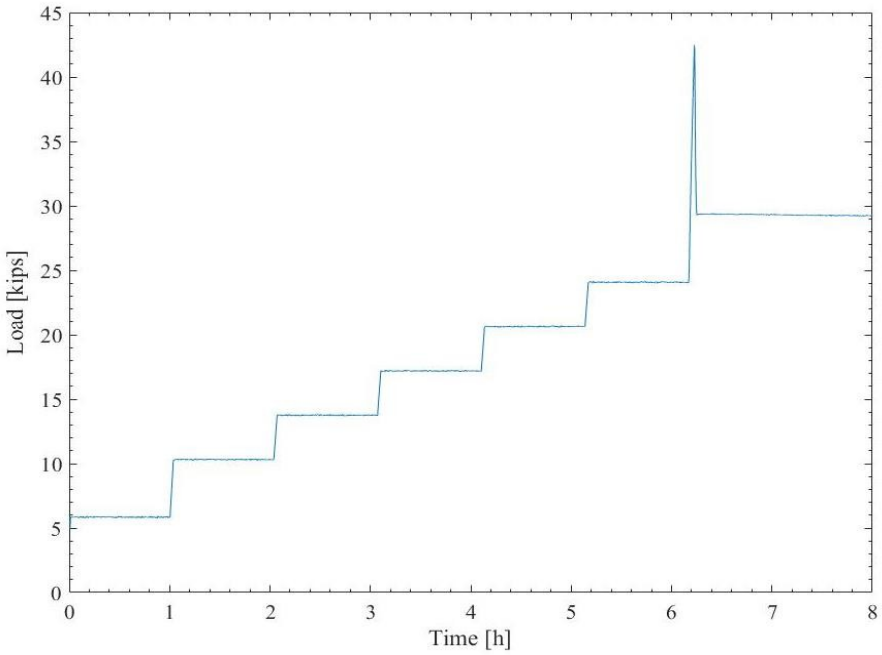

Figure 22. Signal Conditioning Test, Load Cell Output

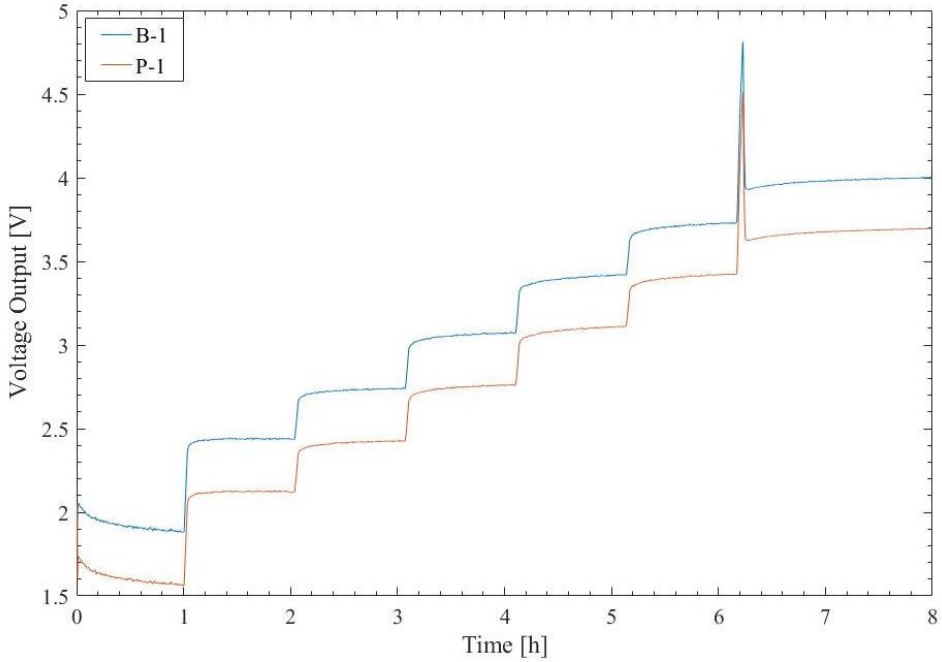

Figure 23. Signal Conditioning Test, Box Outputs

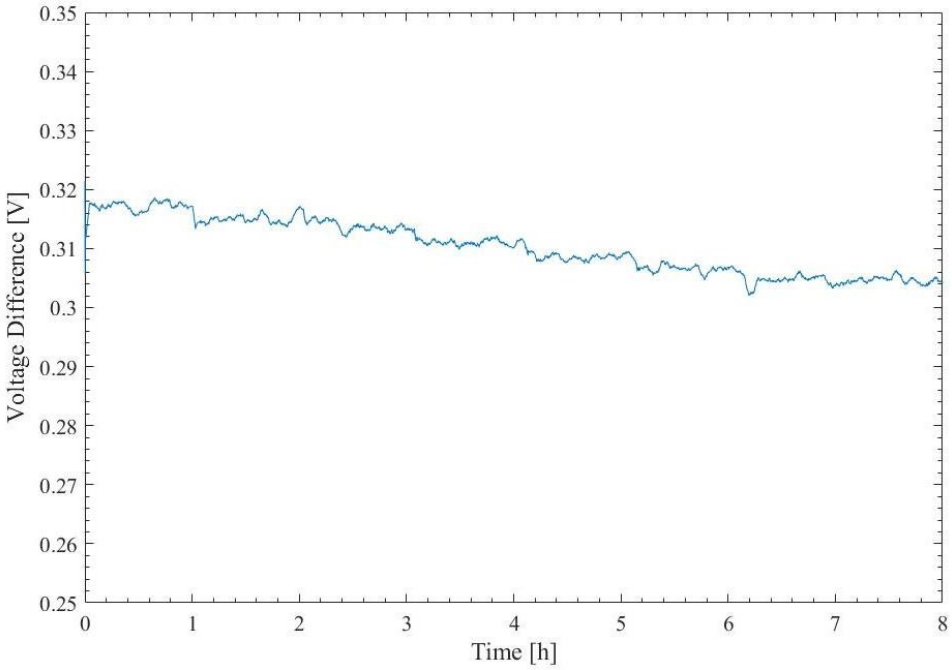

Figure 24. Signal Conditioning Test, Voltage Difference

Figure 25. Environmental Chamber

In order to evaluate this offset, the output voltages of the three circuitry boxes used throughout this thesis were tested on an adapter with no load at 32°F (0°C) using a CSZ Sub Zero Environmental Chamber™, as shown in Figure 25. The inclusion of temperature as a parameter was to ensure that there were similar testing environments for the duration of the signal conditioning characterization tests. A thermocouple was additionally encased within the chamber to confirm that the temperature was 32°F (0°C). Three boxes were characterized for the purpose of this thesis, however, more have been produced since then and the same methods of characterization can be employed. The results of the characterization testing are displayed Table 1. This indicates that every signal conditioning box would have an inherent offset that would need to be characterized for field implementation.

Table 1. Results of Voltage Offset Testing

Circuitry Box Designation	Voltage (V)
B-1	2.78
B-2	2.39
P-1	2.45

2.5 Creep of the Thermoplastic Polyurethane (TPU) Pad

The AdapterPlus™ steering pad is an injection molded thermoplastic polyurethane (TPU) product produced by Steinmetz, Inc. It is classified as a viscoelastic material which will exhibit creep under a constant load and relaxation when the load is removed. Creep is one of the modes in which a material can respond to an applied external force. In this case, the material will

respond to the stimulus by flowing away from the point or region of force application. The properties of the steering pad material are similar to those of TPU Elastollan 1154 D10, which can be found in the Appendix B.

Findles et al. [39] describe how the changes experienced by a viscoelastic material subjected to stress and strain are time dependent. The empirical formula derived for Bakelite, a thermoset created by a condensation reaction of phenol with formaldehyde is as follows:

$$\varepsilon = \varepsilon^0 + Alog(t) + Bt$$

where the terms ε^0, A, and B are coefficients of stress, temperature, and material respectively. The coefficient associated with the logarithmic term is that associated with temperature, which poses an interesting observation concerning previous empirical results. Therefore, it is theorized that by incorporating temperature into the strain gauge voltage calibration, a more accurate correlation which accounts for the shifting pressure distribution that results from the creep flow of the polymer pad can be developed.

In the previous work conducted by Diedrich [25], a pressure sensitive film manufactured by Sensor Products, Inc. Fujifilm Prescale™ was used to map out the pressure distribution between the AdapterPlus™ Steering Pad and the bearing adapter. This film is composed of two sheets: an activator, and an absorber. The activator has tiny capsules that are embedded on the surface of the film and the absorber absorbs the resulting dye that is released when the miniature capsules in the activator-layer rupture. Using a color scale, the pressure experienced in the area of contact with the sheet can be estimated visually by the intensity of the color present. This film was additionally sent to Sensor Products, Inc. to obtain a more detailed analysis of the sample. The results showed that at 50% of full-load of a railcar, the majority of the force is carried by the

interlocking ridges of the steering pad. Other interesting observations that were revealed by the results were that for unloaded conditions, a minimal force is seen in the center of the AdapterPlus™ Steering Pad, where the sensor is located, and at 100% of full-load, the interlocks still carry the majority of the load, however, a portion of the force is distributed over the center. Diedrich [25] provided evidence that supported the theory that the creep of the elastomer pad was linked to the increase in the sensor output voltage when under a constant load, which can be observed in his results in Figure 26, and was found to primarily be an issue when performing static testing.

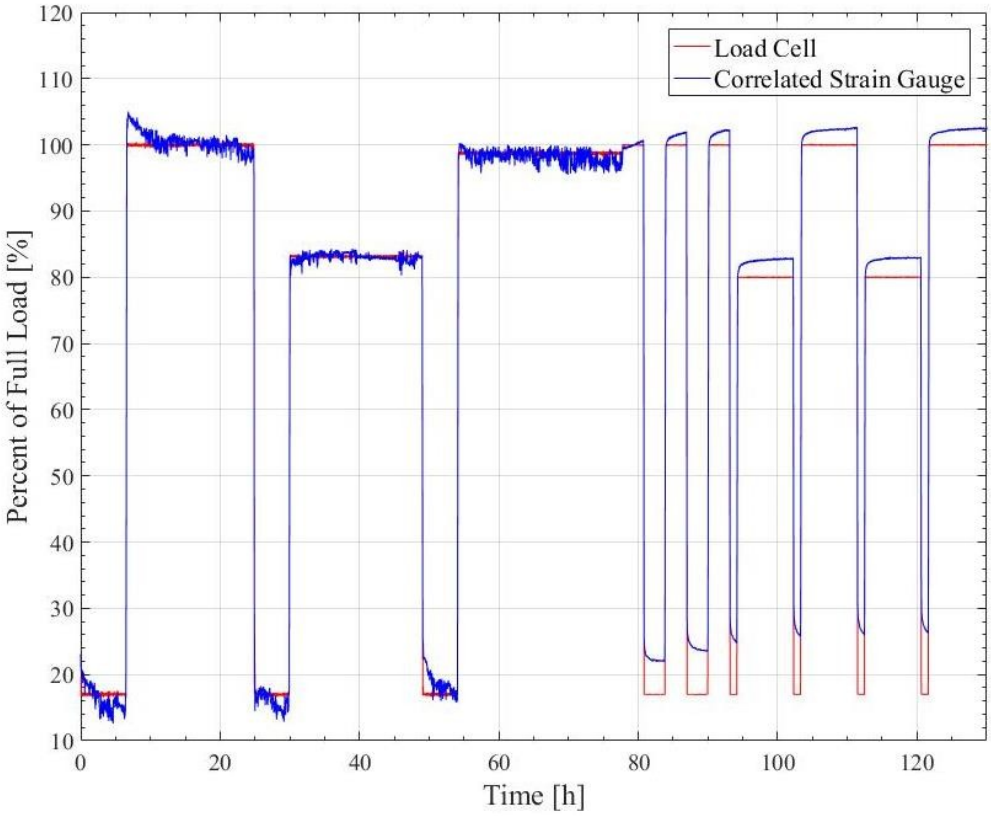

Figure 26. "Adapter C" Results of Diedrich [25]

Diedrich [25] redesigned the sensor in an effort to improve the performance at loads below 50% of full-load and produce a signal. Through his new design, he was able to observe

loads covering the full range seen by a railcar, yet his results still suffered from the creep of the steering pad, which can be observed from the results of the shim testing performed in his thesis. Diedrich [25] placed a shim under the load insert to raise it above the machined adapter surface, which effectively reduced the creep problem and produced more accurate results, however, there still remained a 2-4% error involved with the creep of the pad. Different shim heights were tested to find the optimum height of the sensor with respect to the machined surface. From the previous results, a sensor height of approximately 12 one-thousandths of an inch (0.305 mm) above the adapter surface was found to be the optimal height.

2.6 Calibration Terminology and Methodology

Without integrating a proper calibration into the methodology of the sensor, the overall functionality would be diminished. This calibration transforms the voltage output from the signal conditioning box into a measurable force output. To devise a second-order calibration, several iterations of known load conditions are placed upon the adapter assembly and the voltage output is measured. This data is recorded at a known sampling rate and a correlation is formed between the two. A multivariate correlation follows this same process, but adds a regression method which defines the relationship between the voltage and temperature data.

Diedrich [25] used a second-order correlation that transformed the voltage output of the circuitry into force, and a calibration method that concentrated on the loaded conditions of a railroad bearing. This thesis will propose a multivariate correlation that integrates both temperature data from the inboard and outboard temperature sensors and the voltage output of the circuitry into a measurable force output. This correlation method will largely mimic that performed by Diedrich [25] in an effort to perform a sensible comparison between the two

methods. This section will describe the procedures and nomenclature that were adopted to devise an initial calibration procedure for the proposed load sensors using a single bearing test rig.

2.6.1 Steering Pad Settling

Before a proper reading can be obtained from the strain gauge voltage data, the AdapterPlus™ steering pad must be allowed to adjust to the stresses imposed by the railcar, simulated by the hydraulic cylinder. The adapter is loaded up to the proportional full weight of a railcar (34,400 lb_f or 153 kN), and run at the equivalent of 25 mph (40 km/h) for at least 24 hours before testing can begin. This process allows the elastomeric material of the steering pad to conform to its "loaded orientation" that lasts throughout the testing period. For a shorter settling time of 4 hours, the assembly can be run at 50 mph at the respective full-load of a railcar. The high temperatures that result from the increased speed allow the creep flow of the thermoplastic material to increase.

2.6.2 Static vs. Dynamic Testing

Dynamic testing refers to that which involves the rotation of the axle and will most closely mimic the environment of the moving railcar and has the inherent vibrations that are involved in the rotation of the cup and rollers of the bearing. These vibrations can result in the sensor oscillating well over 1% of the full-load which can increase significantly when the simulation shifts to an unloaded scenario. The impact testing described in Chapter IV will only involve dynamic testing to mimic impacts that occur in the field.

Alternately, static testing refers to that in which the axle does not rotate. This testing procedure is consistent with that used by the majority of filling stations, in which the railcar will stop for a short duration while the loading process is carried out. Loading is typically never done

while the railcar is in motion, and thus, the testing and calibration should mimic the conditions of the filling process. Static testing is the singular form of testing that is performed when developing the "ramping" correlations seen in Chapter III.

2.6.3 Notes on Calibration and Results

The basis for the second-order correlation and multivariate correlation are shown in Figure 27 and Figure 28, respectively. It can be observed that the second-order correlation has two parameters, based on the voltage output of the strain gauge (V), and the multivariate correlation has five parameters, based on the voltage output of the strain gauge (V) and the average temperatures of the raceways (T).

Depending upon the desired conditions of the sensor employment, a calibration plan can be devised to properly suit its intended use. Both a second-order and a multivariate correlation are used in conjunction for dynamic and static testing to compare and find suitable applications for each. For example, to achieve the highest accuracy for fully-loaded tanker cars in an effort to detect leaks, a simple calibration with five temperature scenarios occurring at 95%, 100%, and 105% of full-load can be utilized. Unfortunately, this testing plan would cause inaccurate results at loads below 95% and would not be suitable for any application involving unloaded railcars. A system interface could additionally be designed which allows the train operator to select a proper correlation for a specific period of time. For example, when the train is being loaded, the "ramping" correlation could be selected, and when the train is traveling long distances, the "multivariate fully-loaded" correlation could be selected.

For the purposes of testing, an encompassing calibration was devised which would skew towards higher accuracies for loaded railcars whilst retaining a suitable amount of accuracy for

unloaded railcars. Steps at 17% (unloaded simulation), 80%, 95%, and 100% were utilized for dynamic testing purposes, while static testing conditions required steps at 17%, 80%, and 100%. For the development of the multivariate calibration, this was required to acquire different sensor outputs at various temperatures.

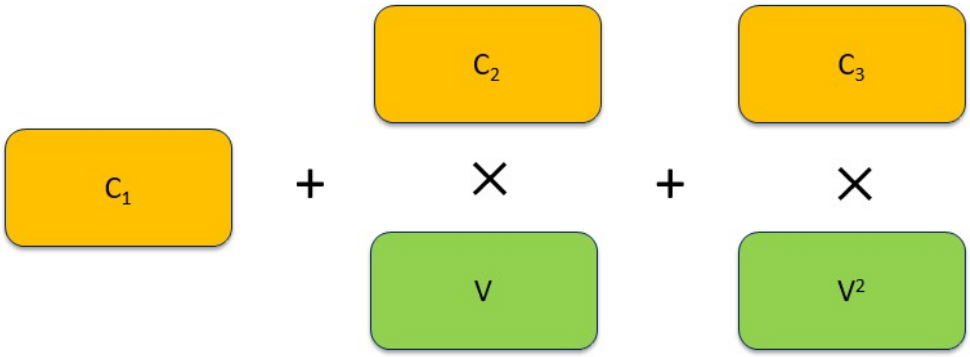

Figure 27. Second-Order Correlation

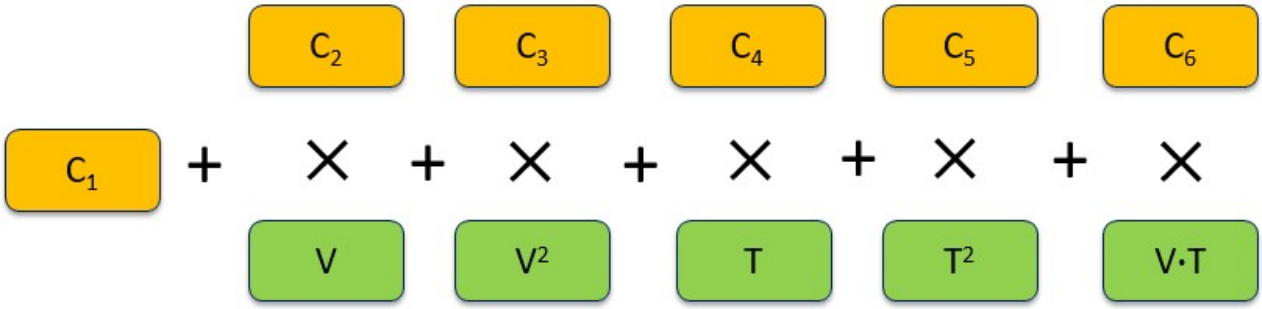

Figure 28. Multivariate-Correlation

The “average error” that is described in the tests that follow is computed by taking the root mean square of the difference between the correlated and actual load, and dividing by the full operating load of a Class K bearing. Therefore, all respective errors can be multiplied by a factor of 34.4 kips to determine the difference in pounds between the correlated and actual load.

It should be noted that the data collected up until five minutes after a loaded period is excluded from the error calculation. Additionally, the “steady-state error” is the error of the difference in the correlated and actual loads with respect to a fully-loaded railcar after three hours under a constant load.

CHAPTER III

ACCURACY TESTING

Four adapters designated A, B, C, and D will be evaluated under the influence of various scenarios and correlations. Initially, a test analyzing the effect of axle rotation and loading variation on the sensor will be examined. This set of testing will compare a second-order voltage correlation method and a multivariate regression method which incorporates the average of the raceway temperatures into the data processing step. Afterwards, a test simulating the filling process of a railcar is examined, in which a third order voltage correlation method was utilized to simulate a railcar loading scenario.

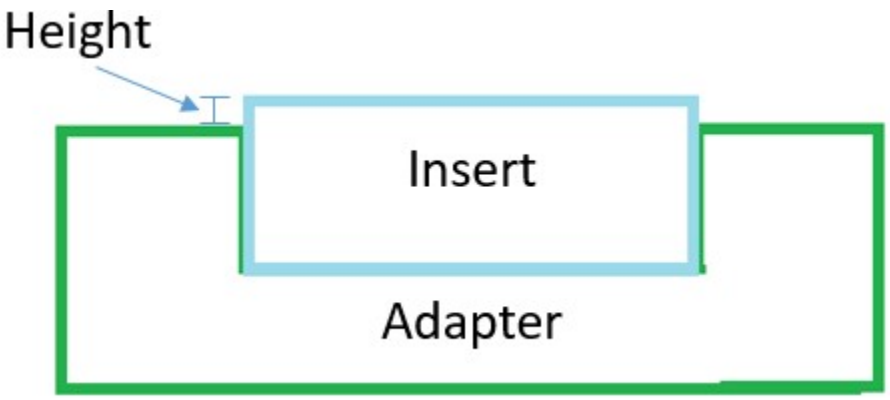

Figure 29. Adapter-Insert Assembly Profile Demonstrating "Insert Height"

Each sensor was characterized by its specified height above the adapter surface, as seen in Figure 29, termed the “free floating height,” as the sensors were not mounted to the adapter

and simply rested in the machined “insert canal”. The heights of each of the sensors above the adapter surface are displayed in Table 2.

Table 2. "Free Floating" Heights Above Adapter Surface

Height Above Adapter Surface (1/1000 inch)		
	Left Side	Right Side
Adapter A	9	12
Adapter B	8	9
Adapter C	8	10
Adapter D	15	18

3.1 Proof of Concept

As discussed by Diedrich [25], the majority of previous testing revolved around constant load and speed, and was an initial, yet necessary, step in the design of the load sensor. However, to be employed in field operations the sensor would need the capability to maintain a steady signal under fluctuating speeds and various loading conditions. Figure 30 illustrates the load sensor response to varying speeds under a constant full-load. It demonstrates a variation of approximately 4.5 % with respect to a fully-loaded railcar, as demonstrated by the horizontal green lines within the figure. High speeds were sequentially interceded by periods of slow speed, accentuating the relationship between the speed, temperature, and perceived load.

Diedrich [25] determined that as the speed fluctuates, the load insert experiences inconsistencies in the perceived load, however, this is not a clear indication as to why the sensor output remains constant at some speeds and decreases in others. It was hypothesized that this change could be attributable to the temperature of the adapter assembly. Due to the foresight of the introduction of two analog temperature sensors into the load insert, the effect of temperature

on the sensor output could be evaluated with ease. The correlated strain gauge output was plotted alongside the average of the raceway temperatures recorded by the load insert. This dependence is demonstrated in Figure 31, where the temperature axis on the right-hand side was inverted to better illustrate the significance of their relationship.

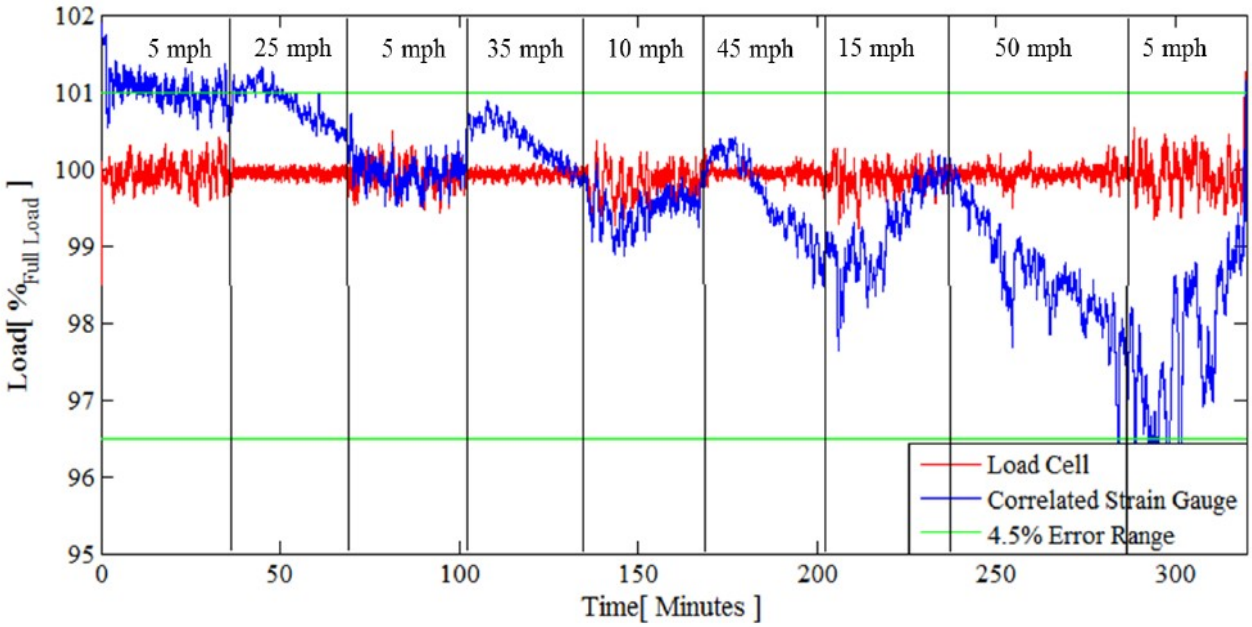

Figure 30. Speed Test Results [25]

By integrating the approximate raceway temperatures of the bearing into the correlation of the load insert, a multivariate linear regression methodology was developed. This regression analysis takes the strain gauge voltage and average of the raceway temperatures to devise a correlation that has the capability to evaluate the load applied to the bearing-adapter assembly as described in Chapter II. This correlation was then applied to the test data as shown in Figure 32. With the use of multivariate linear regression, the entire signal error decreased to within ±0.50%, as demonstrated by the horizontal lines in the figure.

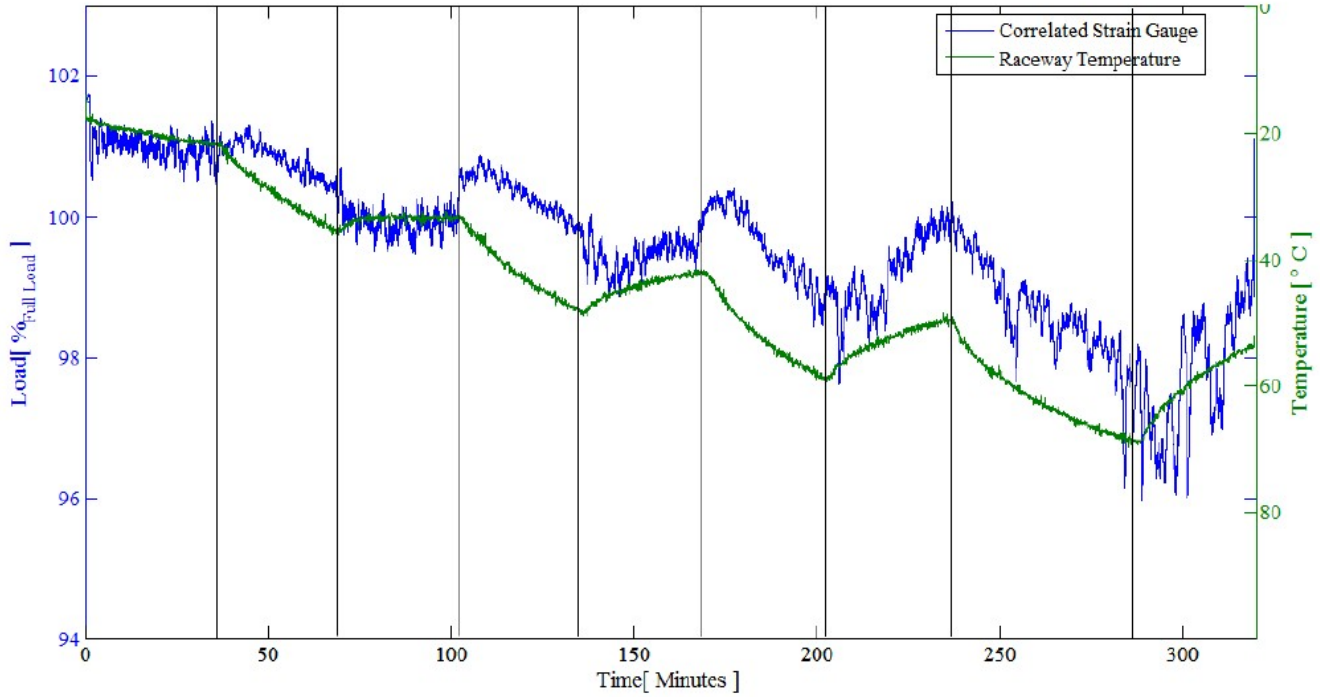

Figure 31. Speed Test Temperature Effect on Strain Gauge Correlation [25]

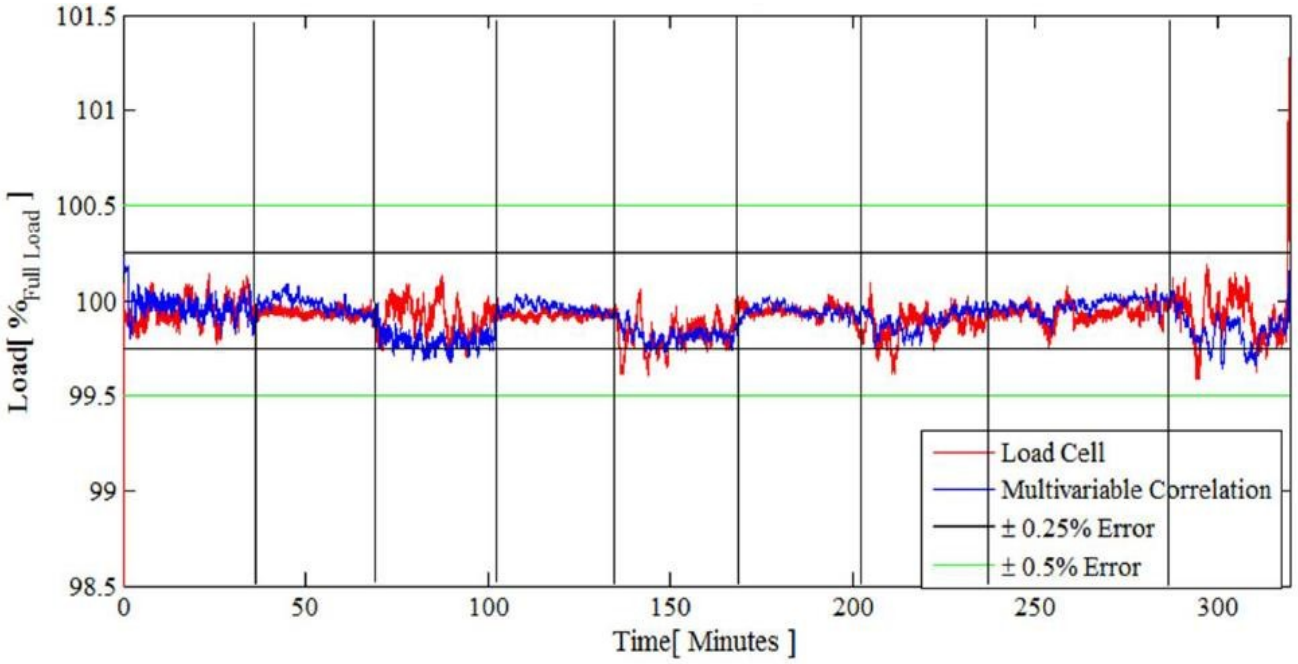

Figure 32. Speed Test Utilizing Multivariate Regression [25]

3.2 Load Accuracy Testing

This section will compare the results of two different correlations on Adapters A, B, and C in an effort to properly compare the accuracies of each adapter. The calibration methodology used to develop the correlations for the "free floating" load inserts, where the sensor rests in the machined canal of the adapter, consisted of a settling portion, a dynamic portion, and a static portion. For the purposes of data presentation, the settling periods will not be shown in the following figures and are not accounted for in the creation of the correlations.

The test that was developed covers the full range of railcar loads from 5,850 lb_f to 34,400 lb_f (26 kN to 153 kN), with an emphasis on loads above 80%, as displayed in Figure 33. All the loading rates were based upon a seven-minute loading speed, or 4,080 lb_f/min (18 kN/min). The unloading time was based upon a three-minute unloading speed from 100% to 17% of a fully-loaded railcar, or -9,520 lb_f/min (-42 kN/min). The reported loading and unloading rates were provided by Amsted Rail as examples used in the rail industry for the loading and unloading of grain.

The settling period required a minimum of 18 hours at full-load with the axle revolutions comparable to a railcar moving at 25 mph (40 km/h). After the settling period, the dynamic portion of the test was conducted at 25 mph (40 km/h). This test consisted of three load steps of approximately 80%, 95%, and 100% with respect to a full-load, which were held for 18 hours each and interceded by six hour unloaded periods. These step loads were slightly altered for each adapter to see if there was a positive or negative effect on the accuracy of the developed correlation. Five minutes before any change in load, the axle rotation was stopped to simulate an realistic loading/unloading scenario. After the load was changed to the specified condition, the axle remained stationary for an additional five minutes before rotation resumed.

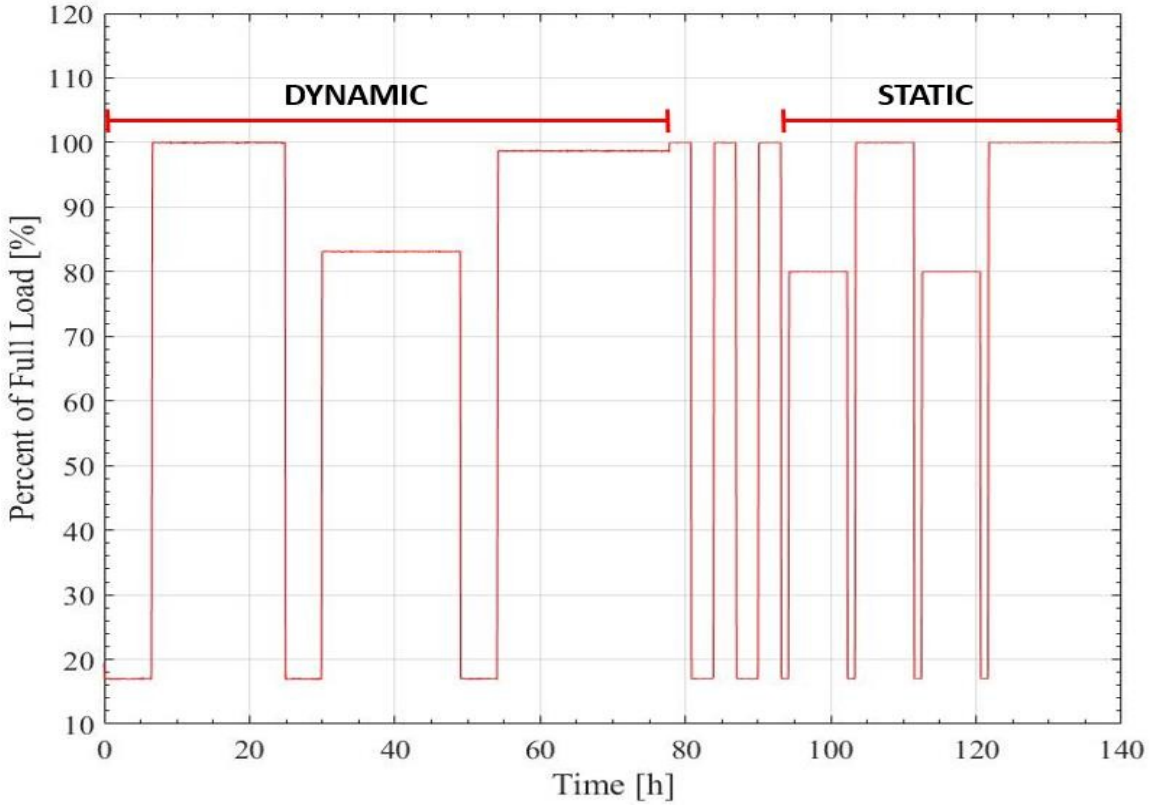

Figure 33. Load Accuracy Test Apportionment

The static portion of testing consisted of four loading and unloading cycles where the loaded portions were held for eight hours each with no axle rotation. Due to the functionality of the sensor, the perceived dynamic load is more important than the static load. Error analysis will accompany each portion of testing, but greater emphasis should be placed on the error of the dynamic and loaded scenarios.

The dynamic and static portions of the test, indicated in the following analysis, were used as the calibration range, differing from the method developed by Diedrich [25] which simply utilized the dynamic period as the basis of calibration. This was done for two reasons: the first being that additional temperature information is needed for proper calibration of the multivariate

correlation and the second being that, to develop a correlation that could be used accurately in scenarios where the train is moving and stationary, both data sets are needed.

The average errors of each portion of testing will be examined. Additionally, there will be mention of the "loaded error," which refers to the error involved with portions of testing that are 80% of full-load and above. The signal conditioning box designated B-1 and the 100-kip (445 kN) load cell were employed throughout the duration of the load accuracy testing. The derived correlations and errors for each adapter can be found in the Appendix A.

3.2.1 Adapter A

The full testing performed on Adapter A can be seen in Figure 34 and Figure 35, where the moving average was calculated every 200 data points at a frequency of 50 Hz (4 seconds of data). When compared to the following adapters, the results of Adapter A will look more stable due to the implementation of a power inverter just previous to the testing of this sensor. It can be observed that the second-order correlation tends to underestimate the load during the dynamic period and overestimate the load during the static period, where the signal of the load sensor logarithmically increases. The average error for the second-order method is 2.08% (Figure 34). When utilizing the multivariate correlation, however, the "steady-state error," or that which occurs approximately after three hours under constant load, is within 1% of the actual load for each step and the average error for the full test period is 1.00% (Figure 35).

The dynamic portion of the testing can be observed in Figure 36 and Figure 37. It can be seen that the second-order correlation in Figure 36 tends to under-predict both the loaded and unloaded portions of the test and had an average error of 1.49%. In the unloaded portions, the post-processed sensor output reacts erratically when compared to the loaded portions of testing,

which will be a trend that is common across all testing due to the increased oscillations and creep relaxation found in the dynamic-unloaded scenarios. It can additionally be observed that the 80% step of the dynamic portion of testing has an average error exceeding 2%.

Figure 37 shows the dynamic portion of testing utilizing a multivariate correlation which had an average error of 0.94%. One notable trend typical of the implementation of the multivariate correlation into dynamic scenarios, is when the adapter is initially loaded, the correlation will overestimate the intended load, which is due to the limitation of the calibration procedure that is used for the load accuracy testing and the nonlinear relationship temperature has with creep.

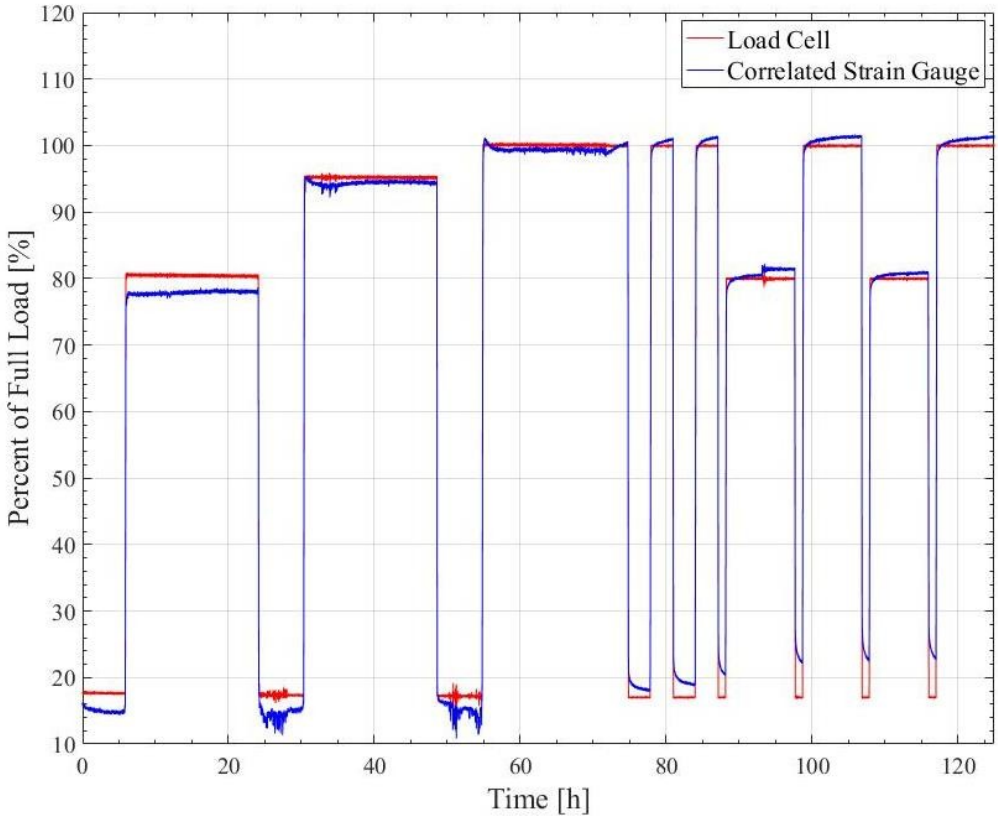

Figure 34. Adapter A Load Accuracy Test, 2nd Order Correlation

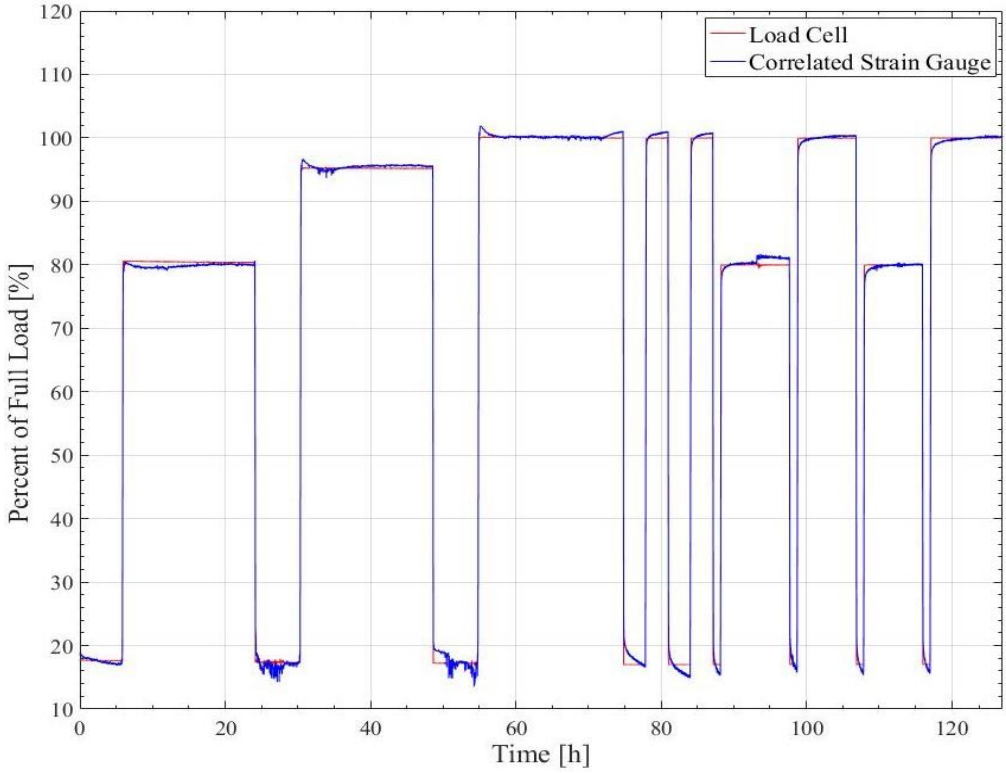

Figure 35. Adapter A Load Accuracy Test, Multivariate Correlation

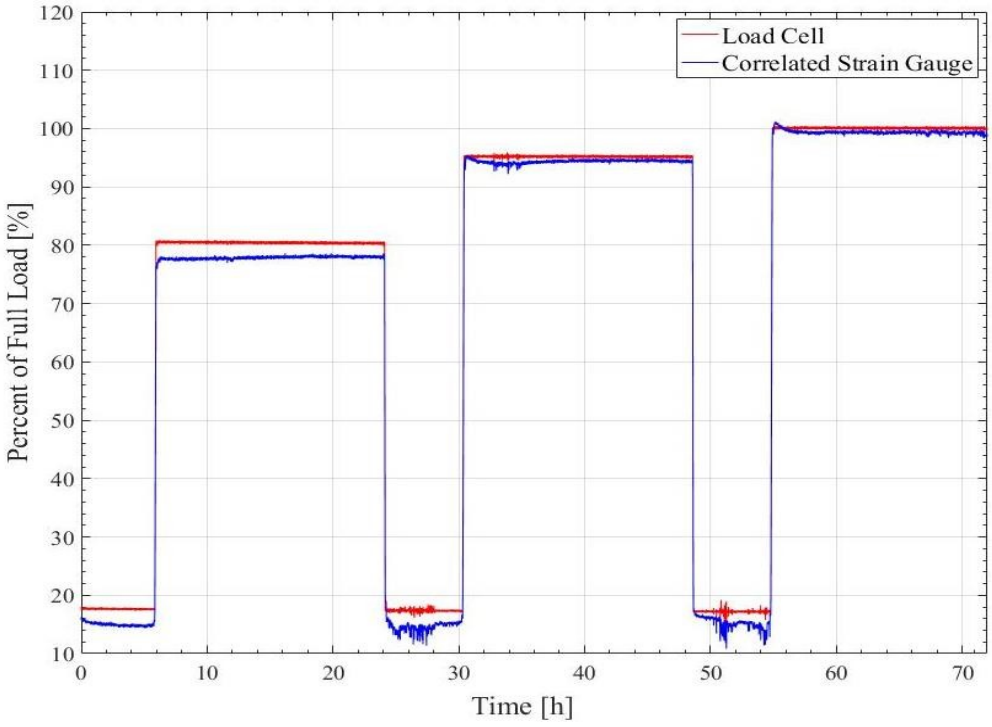

Figure 36. Adapter A Load Accuracy Test, Dynamic, 2nd Order Correlation

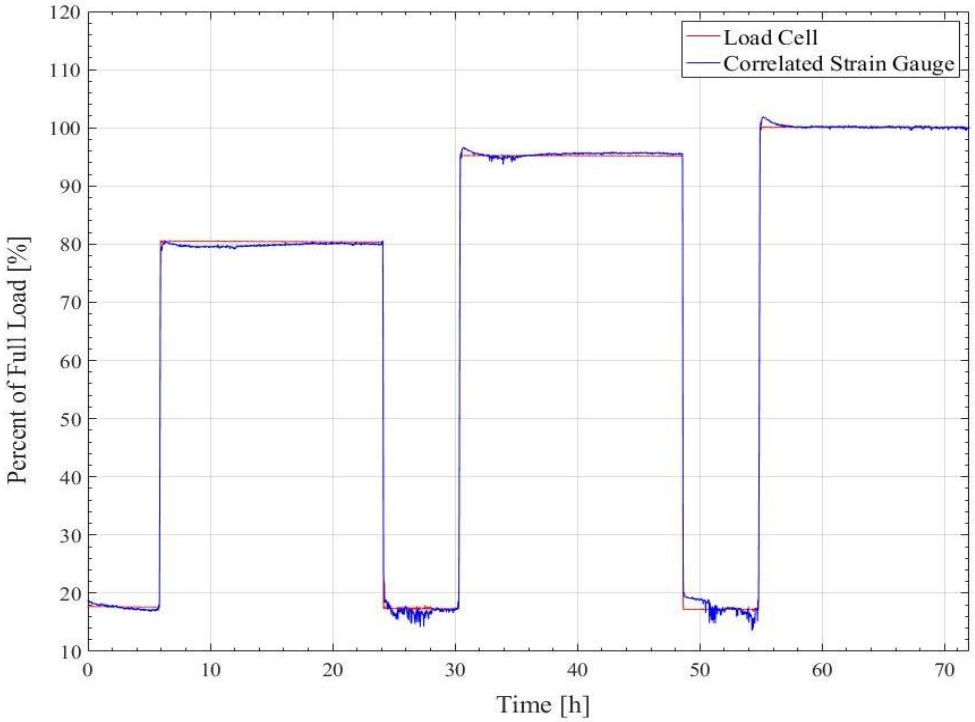

Figure 37. Adapter A Load Accuracy Test, Dynamic, Multivariate Correlation

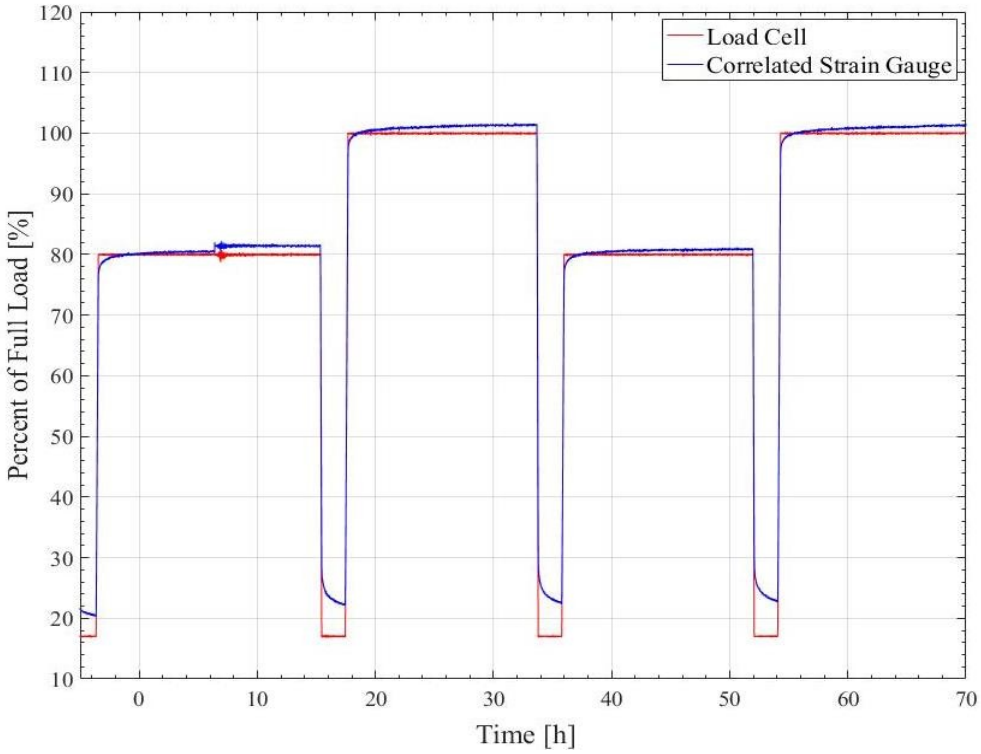

Figure 38. Adapter A Load Accuracy Test, Static, 2nd Order Correlation

The static portion of testing employing a second-order correlation is displayed in Figure 38. The steady-state error for the fully-loaded steps is approximately 1.5% and the steady-state error for the 80% steps is approximately 1%, however, an unusual step increase occurs in the first 80% loaded step. The average error for the full static testing period utilizing the second-order correlation is 2.20%.

The static portion of testing utilizing a multivariate correlation is displayed in Figure 39. The steady-state error for the fully-loaded steps is below 0.4% and the steady-state error for the 80% steps is below 0.5%, however, the small increase that occurred during the first 80% load step resulted in a 1.2% error increase, which was theorized to be due to a change in the grounding of the data acquisition. Even with this uncharacteristic step in voltage, the multivariate regression method had an average error of 1.01% for the static portion of testing.

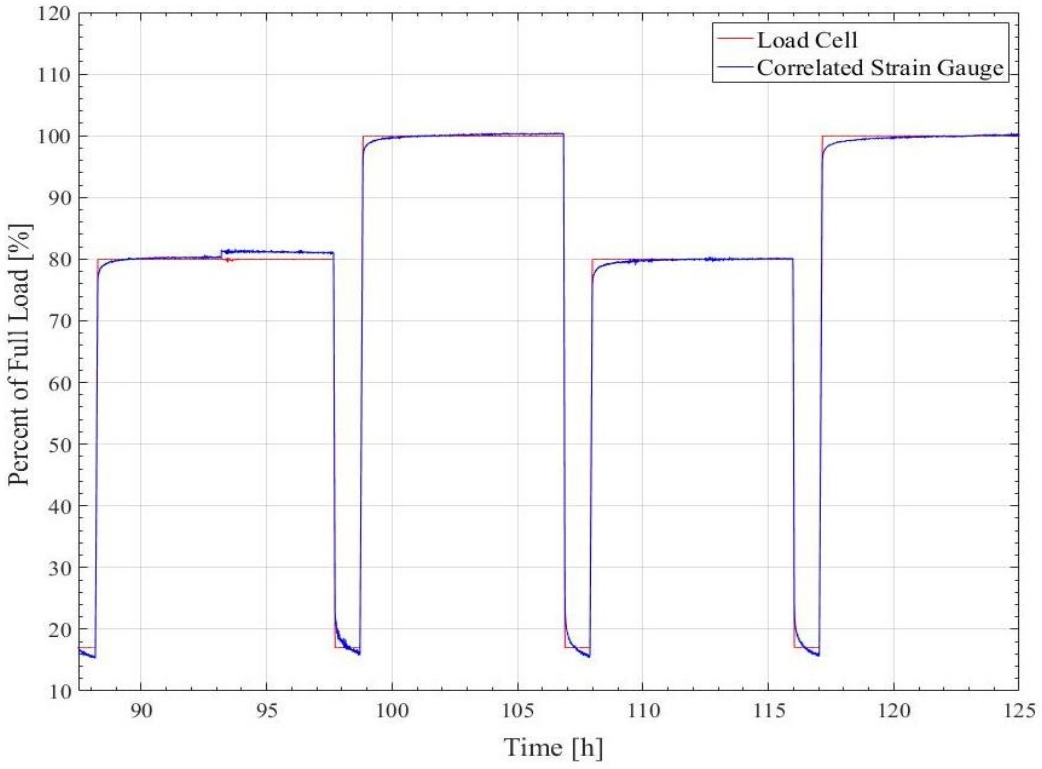

Figure 39. Adapter A Load Accuracy Test, Static, Multivariate Calibration

3.2.2 Adapter B

When conducting load accuracy testing on Adapter B, the moving average was calculated similar to the previous testing, for every 200 data points (4 seconds). The full load accuracy test for Adapter B utilizing a second-order correlation can be seen in Figure 40. This correlation had an average error of 1.82% for the full testing period. It is clear from the data presented that the load controller failed to monitor the load during the dynamic portion of testing. This was a singular occurrence, as the controller uses a carbon brush motor. These brushes wear, and when too thin, they will fail to complete the electric circuit within the motor. This incident allowed further alteration of the proposed dynamic procedure, which resulted in an emphasis on the "fully-loaded dynamic" scenario. The second-order correlation tends to under-represent the load during the dynamic portion and over-represent the load during the static portion of testing, similar to the load accuracy testing of Adapter A. When utilizing the multivariate correlation, shown in Figure 41, a much more accurate correlated output was attained which lowered the average error of the testing period to 0.86%.

In Figure 42 and Figure 43, the dynamic portion of testing utilizing both correlations for Adapter B are shown. It can be seen in Figure 42 that the strain gauge readings correlated with the second-order method tend to under-predict the load observed by the load cell. For the 100% step with respect to full-load, the steady-state error varies between two and three percent. The average error for the dynamic portion of testing utilizing the second-order correlation was 2.00%.

In Figure 43, the dynamic portion of testing utilizing the multivariate regression method is displayed. The average error is 0.87% throughout the full dynamic period and 0.58% when considering only the loaded portions of testing. When compared to that of the second-order

correlation, which is 1.74% for the fully-loaded portion of the test, this would account for a 399 pound (1,775 N) disparity between the two methods of calibration.

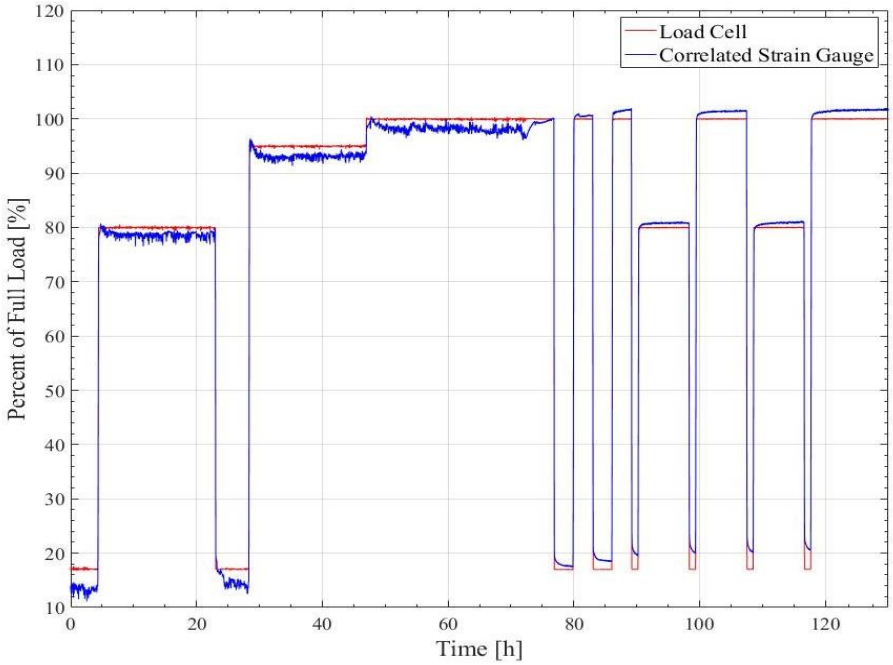

Figure 40. Adapter B Load Accuracy Test, Second-Order Correlation

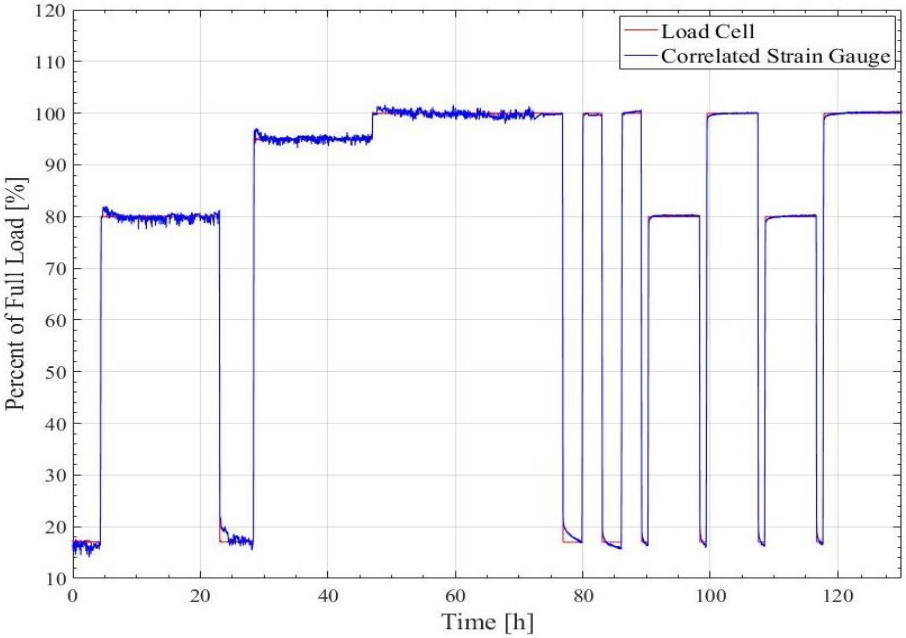

Figure 41. Adapter B Load Accuracy Test, Multivariate Correlation

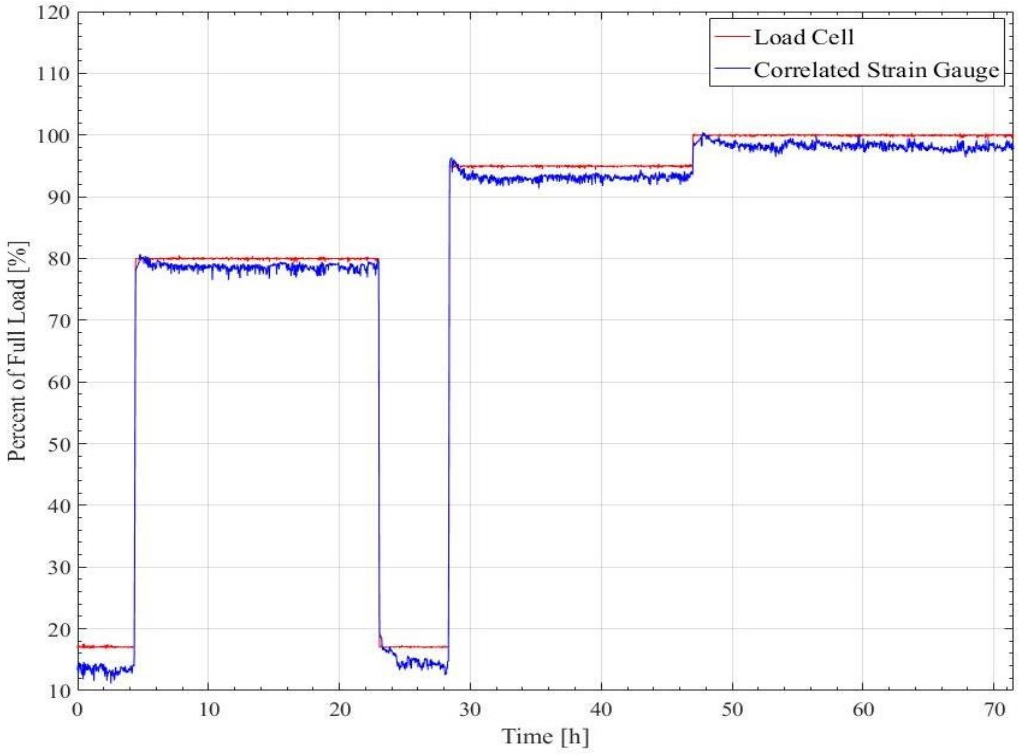

Figure 42. Adapter B Load Accuracy Test, Dynamic, 2nd Order Correlation

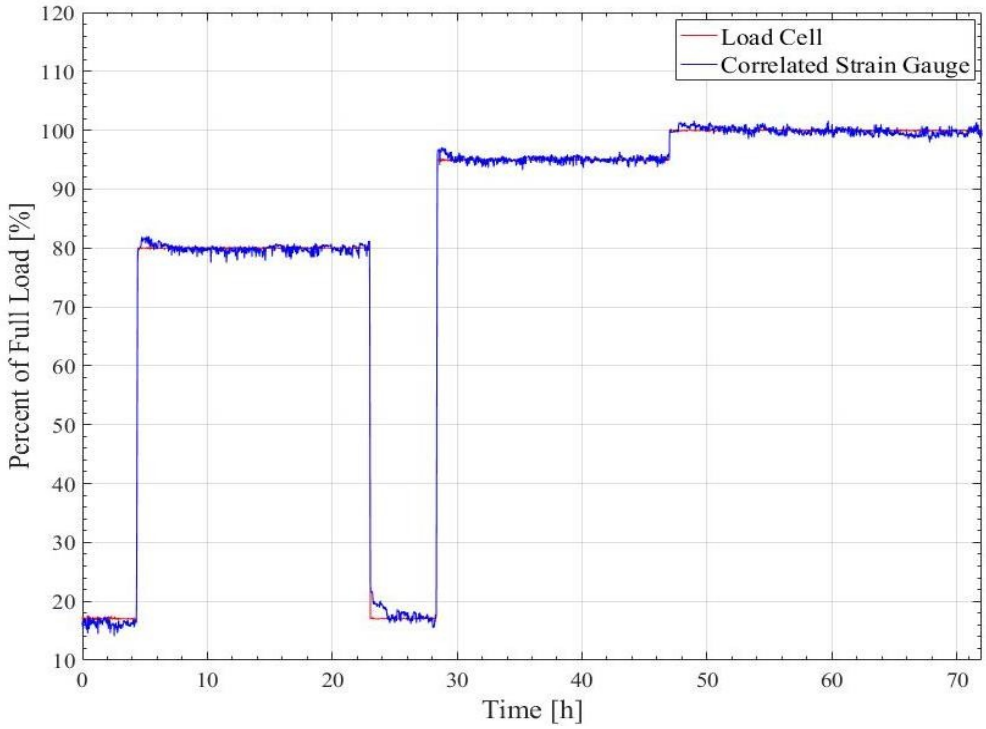

Figure 43. Adapter B Load Accuracy Test, Dynamic, Multivariate Correlation

In Figure 44 and Figure 45, the static portion of testing employing both correlations for Adapter B can be seen. There is again a logarithmic increase in the loaded portions when using the second-order correlation, which increases the loaded error of the testing utilizing the second-order correlation to 1.01%. The total average error throughout the static portion of testing utilizing the second-order method was 1.66%. Figure 45 shows the multivariate regression method applied to the static portion of testing for Adapter B. The average error for this portion of testing was approximately 0.79%, which would result in 299 pounds (1,330 N) of unaccounted cargo if the second-order correlation was implemented rather than the multivariate for static scenarios.

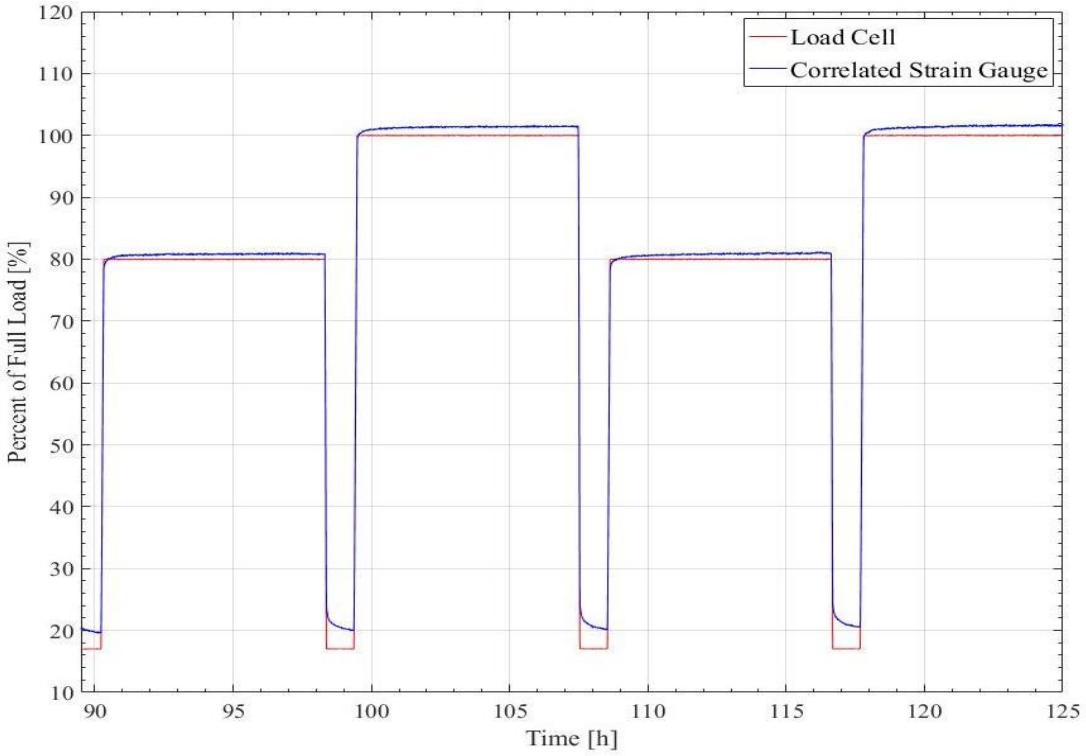

Figure 44. Adapter B Load Accuracy Test, Static, Second-Order Correlation

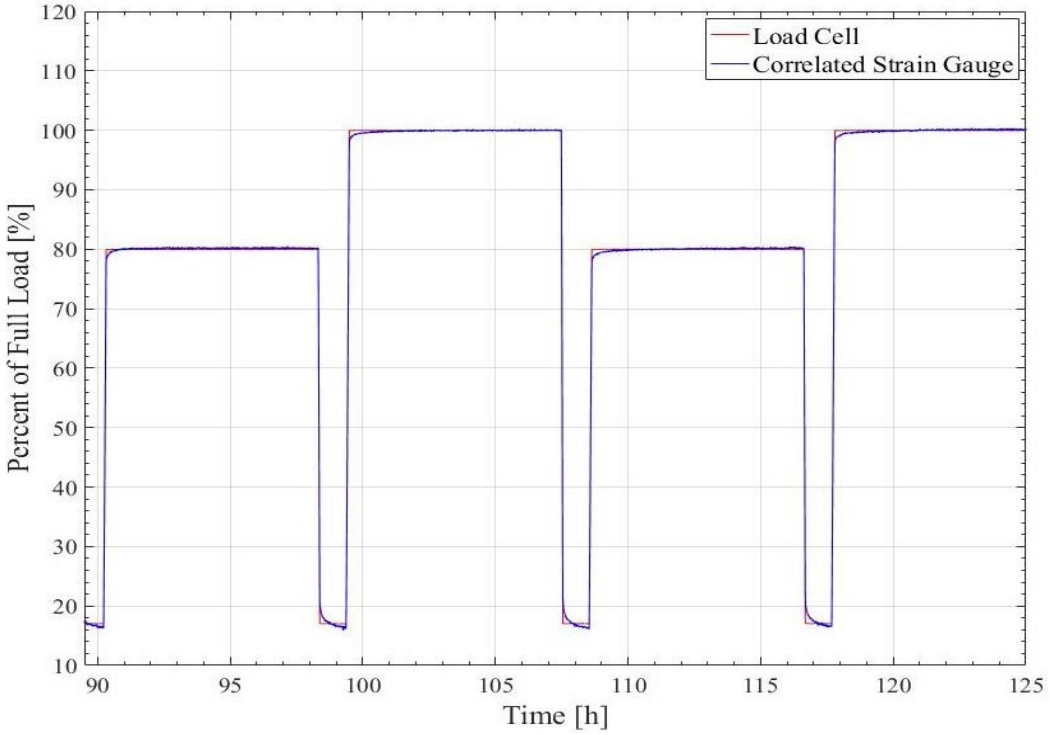

Figure 45. Adapter B Load Accuracy Test, Static, Multivariate Correlation

3.2.3 Adapter C

The overview of testing conducted on Adapter C utilizing a second-order correlation can be seen in Figure 46. When the raceway temperature data was incorporated into the correlation to create the multivariate correlation, as shown in Figure 47, a much more accurate representation of the load was created. The data for this set of testing was post processed with a moving average of 200 data points to ensure similar results when compared to the testing of Adapters A and B. The total average error throughout testing for Adapter C was 2.41% when using the second-order correlation, however, when the multivariate regression was implemented, seen in Figure 47, this average error decreased to 1.56% which results in a disparity of approximately 292 lbs (1,300 N).

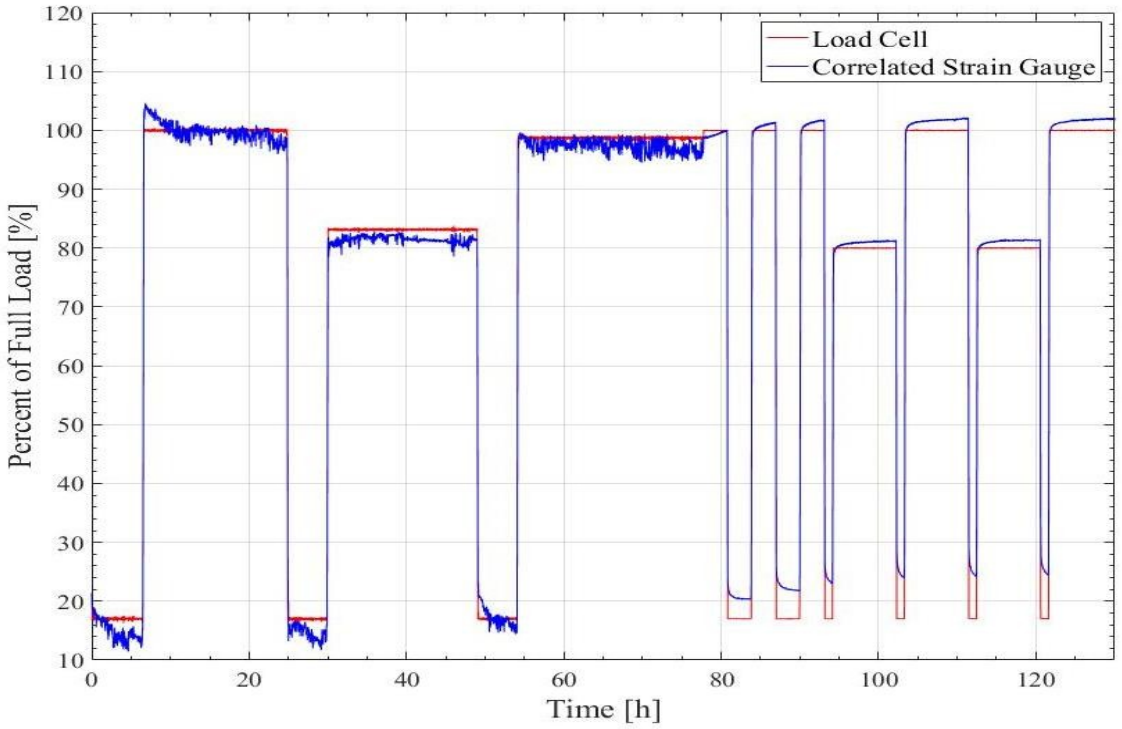

Figure 46. Adapter C Load Accuracy Test, 2nd Order Correlation

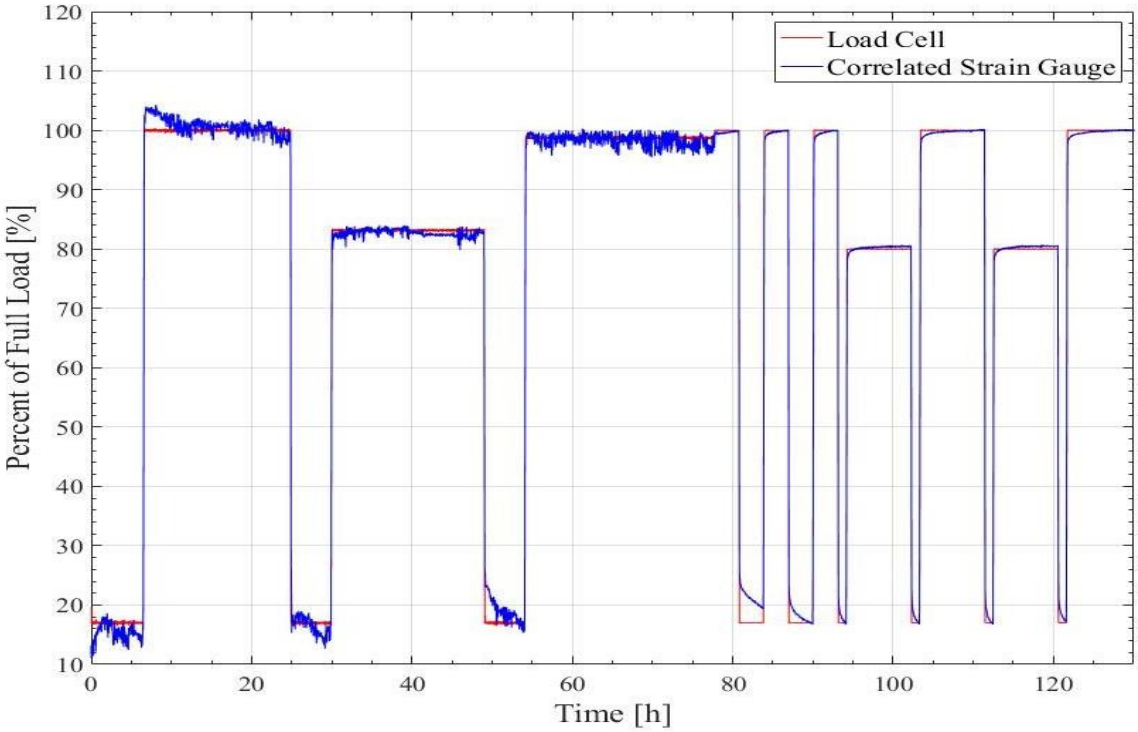

Figure 47. Adapter C Load Accuracy Test, Multivariate Correlation

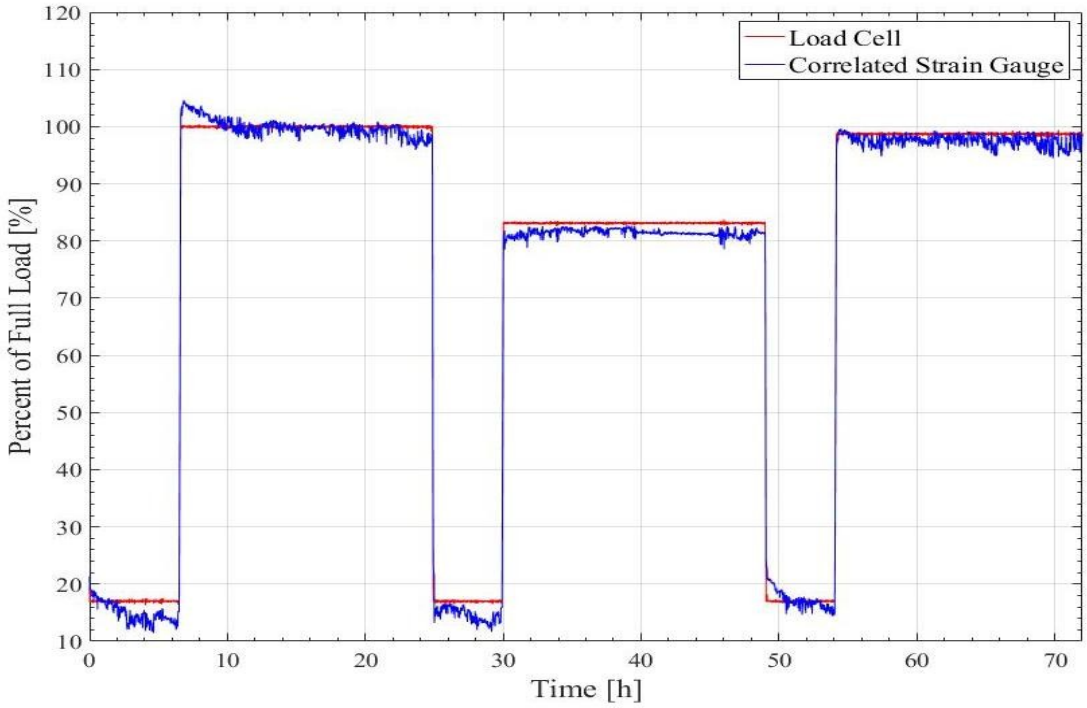

Figure 48. Adapter C Load Accuracy Test, Dynamic, Second-Order Correlation

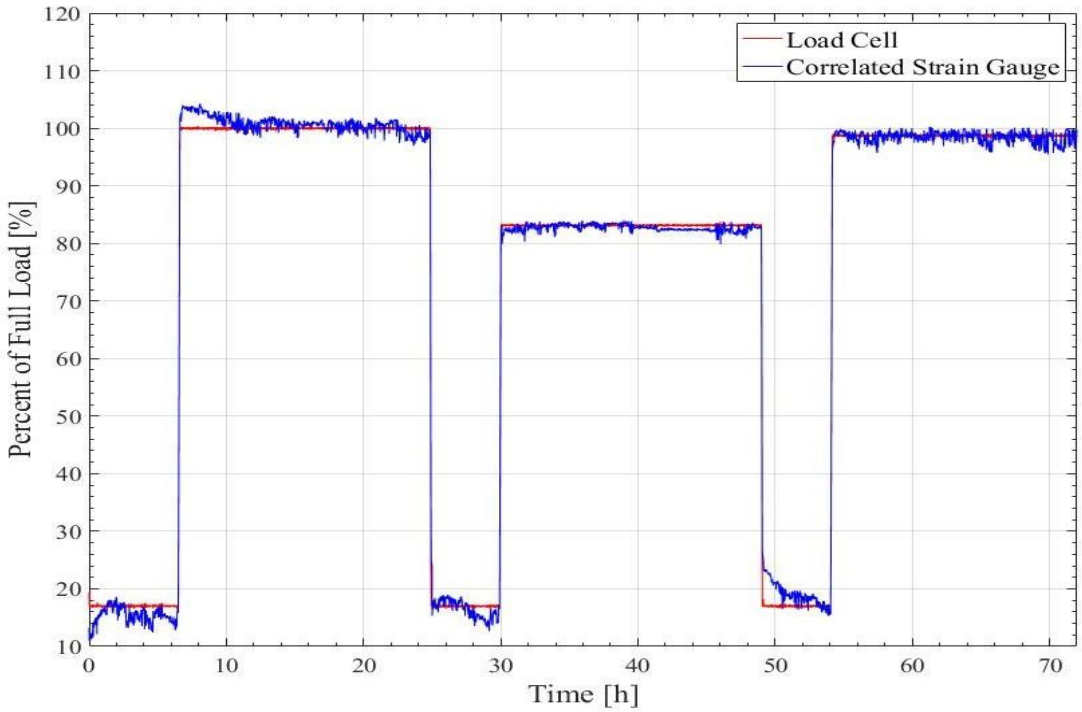

Figure 49. Adapter C Load Accuracy Test, Dynamic, Multivariate Correlation

In Figure 48, the dynamic portion of testing which employs the second-order correlation can be seen. It is demonstrated that this method tends to underestimate the load of the bearing when the axle is rotating. The correlation had an overall "loaded" error of 1.65%, which is representative of a 568 pounds (2,526 N) difference between the correlated load and the actual.

In Figure 49, the test results applying the multivariate correlation can be seen. For both the second-order and the multivariate correlations, during the initial 100% step, the sensor overestimates the intended load for a significant amount of time which is attributable to the loading rate of the system and the resulting high pressure distribution in the region of the applied load for the first several hours while the system is reaching its steady-state operating temperature. It is presumed that this occurs primarily in this evaluation due to the order of steps in the dynamic portion of testing for Adapter C, in which the 100% loaded step was conducted first. This trend, however, is clearly in the voltage data, as it is present in both calibrated figures, which implies that the steering pad might have been at a lower temperature and less able to flow after the initial loading period. The overall average error for the loaded portions of the dynamic test utilizing multivariate regression analysis is 1.12%, which is representative of a 385 lb (1,710 N) error compared to the actual.

Figure 50 shows the static portion of the test employing the second-order calibration method. These results display the tendency of the correlation to overestimate the actual bearing load by over 1%. The average error of all the loaded steps amounted to 1.41%, which is representative of 485 lbs (2,160 N) of cargo when compared to the actual. The results of the multivariate correlation for the static portion of testing are shown in Figure 51. The plot shows that this correlation more accurately reflects the load seen by the bearing and outperforms the second-order correlation by an average approximation of 1.45% (499 lb_f or 2,220 N) over the full

testing period. The average error for the loaded portions of static testing amounted to 0.43%, which is representative of 148 lbs (658 N) of cargo.

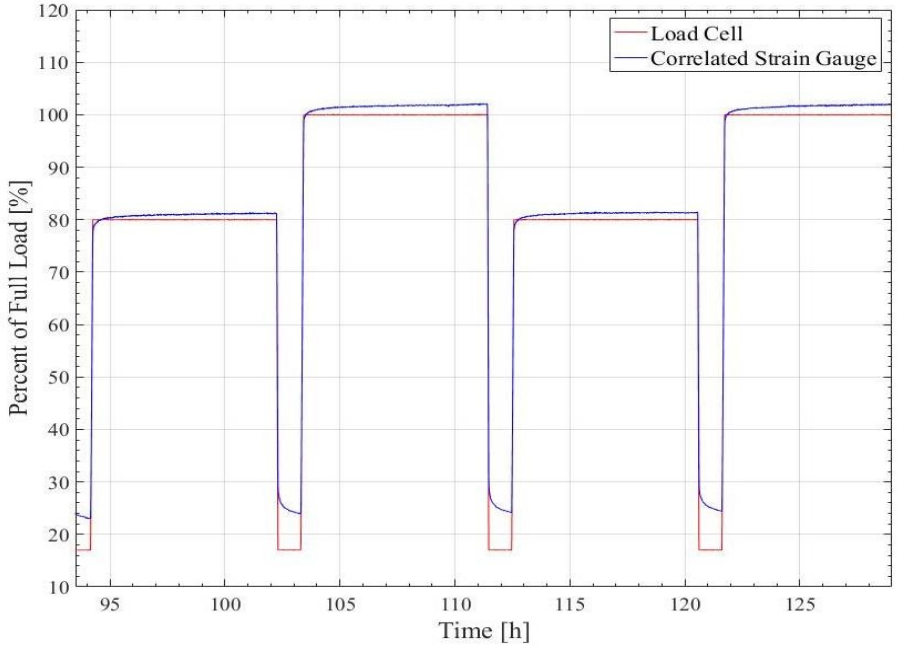

Figure 50. Adapter C Load Accuracy Test, Static, 2nd Order Correlation

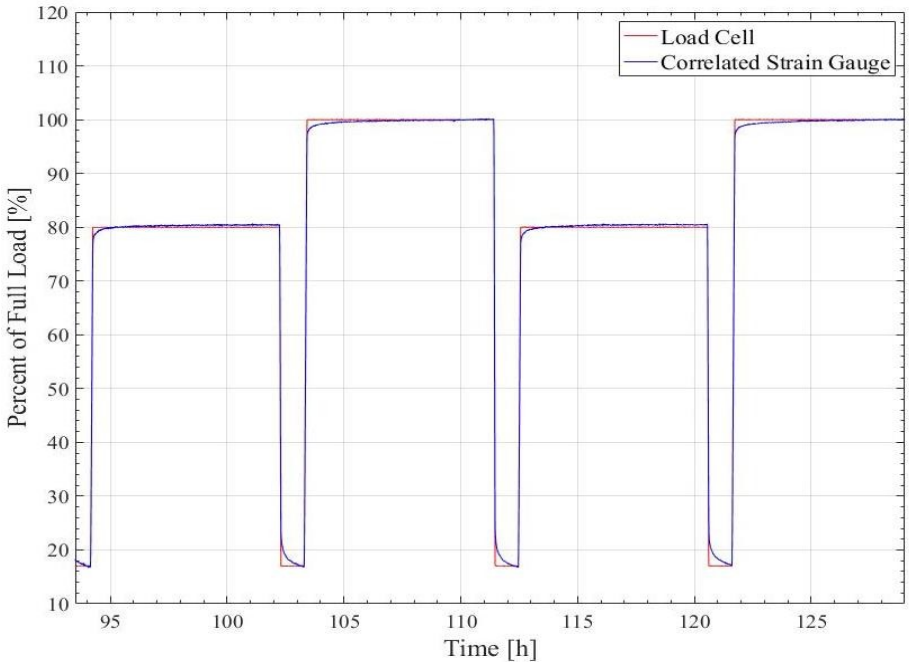

Figure 51. Adapter C Load Accuracy Test, Static, Multivariate Correlation

3.2.4 Summary of Load Accuracy Testing

A summary of the overall performance of each sensor can be viewed in Table 3. The accuracy of the loaded portions of testing as well as that of the full test is shown. When initial development began, it was important to the original sponsor of the project for the load sensor to have an error less than 1% of the fully-loaded weight of a railcar (344 lbs or 1,530 N). From the results of the load accuracy testing, this goal was met for two of the tested adapters and was exceeded in most "loaded" scenarios. In particular cases, the average error of the multivariate correlation is below 0.5% when taking into account only loaded situations which would more accurately simulate that which would be required for field operations.

Table 3. Error Summary of Load Accuracy Testing

	Adapter A		
	2nd Order (%)	Multivariate (%)	Resulting Error Difference (lbs)
Full Test	2.08	1.00	372
Dynamic Loaded	1.65	0.51	392
Static Loaded	0.98	0.64	117
Dynamic	1.49	0.94	189
Static	2.20	1.01	409
	Adapter B		
	2nd Order (%)	Multivariate (%)	Resulting Error Difference (lbs)
Full Test	1.82	0.86	330
Dynamic Loaded	1.74	0.58	399
Static Loaded	1.01	0.27	255
Dynamic	2.00	0.87	389
Static	1.66	0.79	299
	Adapter C		
	2nd Order (%)	Multivariate (%)	Resulting Error Difference (lbs)
Full Test	2.41	1.56	292
Dynamic Loaded	1.65	1.12	182
Static Loaded	1.41	0.43	337
Dynamic	1.82	1.49	114
Static	3.11	1.66	499

3.3 "Ramping" Correlation

A useful application of the load insert lies in the ability to use this technology alongside railcar loading systems. For this objective to be fulfilled, the sensor must have the ability to readily provide feedback necessary to automate loading and would inevitably have the capability replace the crude loading systems that are currently in use that employ fill lines to approximate the volume and weight of the railcar system.

The testing process and performance evaluations that follow were preceded by the normal settling period to allow the adapter pad to conform to the stresses imposed by the test rig. The axle was static throughout the testing period excepting the duration of the settling period conducted at 25 mph (40 km/h) as described in Chapter II, which is done to properly simulate a railcar loading scenario, in which the cars are either stationary, or in a few exceptional cases moving at an extremely slow velocity.

Table 4. Filling Rates (Load per Bearing)

Relative Loading Time (Unloaded to Loaded)	Loading Rate (lbf/min)	Loading Rate (kips/h)
18 s	95167	5710
35 s	48942	2937
1 min	28550	1713
1 min 30 s	19033	1142
2 min	14275	857
2 min 30 s	11420	685
3 min	9517	571
3 min 30 s	8157	489
4 min	7138	428
5 min	5710	343
7 min	4079	245
10 min	2855	171
12 min	2379	143
15 min	1903	114

The loading periods were the only portions of testing used to calibrate the sensor. An example of the loading rates as well as the typical testing outline can be seen in Table 4 and Figure 52, which were taken from the data involving the testing of Adapter D. As can be observed, a one hour loaded period occurs after the loading takes place, which is followed by a three-minute unloading period, followed by a 15-minute unloaded period until the next loading rate is applied. This correlation would only be implemented during the actual filling process and would not be utilized for monitoring load after the loading cycle is complete. Adapters B, C, and D were evaluated through this testing process using signal conditioning box B-2 and the 50 kip (222 kN) rod-end load cell.

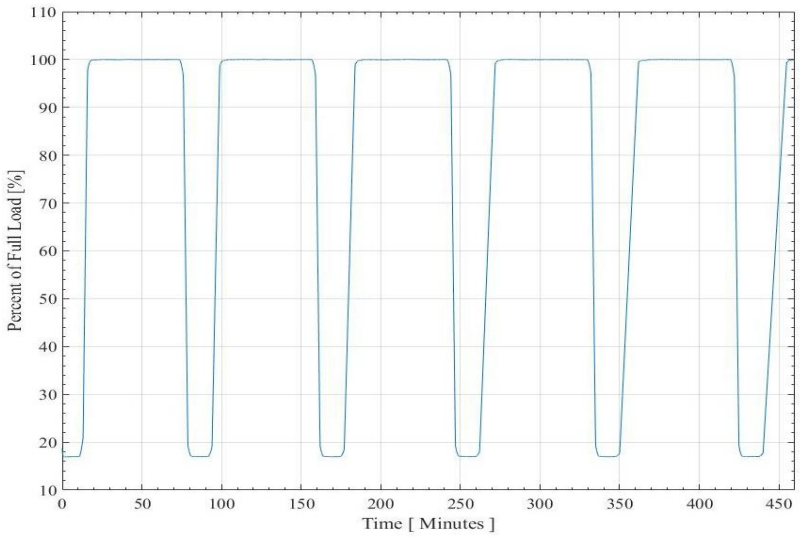

Figure 52. Overview of Ramping Test

3.3.1 Exclusion of Multivariate Correlation

The bearing and adapter were at room temperature throughout the majority of the ramping periods. Due to the limited temperature data, a multivariate calibration was not a suitable choice as the coefficients of the temperature parameters in the correlation would be near zero. The multivariate correlation is additionally not ideal for loading scenarios as the loading

periods for railcars are typically too fast to assume creep flow would occur in the polymer pad. It can therefore be assumed that for the following tests, the polymer steering pad acts as a solid and does not flow for the duration of loading. In the future, additional evaluations of the applicability of the multivariate calibration for loading periods should be conducted to determine the effect of temperature on the sensor without assuming creep flow.

In the face of these challenges, both a second-order and third order correlation were derived. The second-order correlation fomented severe errors, upwards of 5%, with respect to full-load at the end of the loading cycle which would inevitably cause severe inaccuracies if a human operator were loading the car. Therefore, it was decided that the third order correlation was the most suitable choice due to the empirical testing data.

3.3.2 Third Order "Ramping" Correlation

The following graphs will demonstrate the accuracy of the load sensor during loading periods while employing a third order voltage correlation. The results will be displayed in a format that exemplifies the relationship between the progressions of the actual load, as observed by the load cell, with the error between the correlated and actual loads with respect to the full-load (34,400 lb_f or 153 kN). The relationship of the error of the sensor and the actual load are shown for each testing case. The correlations derived from the testing data as well as the errors involved for each loading rate can be found in the Appendix A.

3.3.3 Adapter B

When initially evaluating the implementation of the sensor into loading scenarios, the assumption of a seven-minute loading rate for a grain car, as mentioned in the previous section, was used as a foundation for the initial ramping test conducted on Adapter B, as this particular

sensor was consistently accurate for the set of load accuracy testing. The test design implements various loading rates to obtain an average third order correlation that can be used for all scenarios. The initial test analyzed loading rates of: 3, 5, 7, 10, 12, and 15 minutes. The results of the first set of testing on Adapter B can be observed in Figure 53.

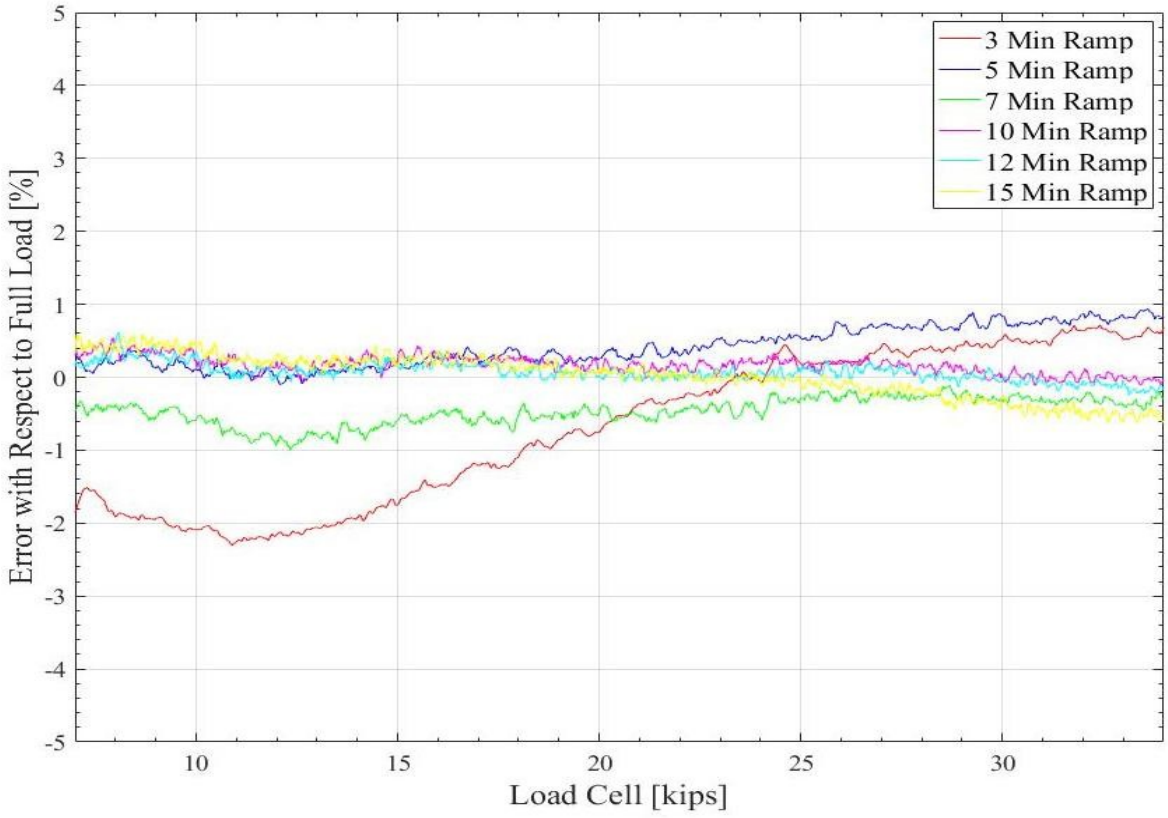

Figure 53. Adapter B Ramping Test Results

Figure 54 shows the region of Figure 53 from 33 kips to 34.4 kips (133 kN to 153 kN). The maximum error seen for the correlation was that of the five-minute loading time (1.57%) and the range of error was -0.06% to 1.57%. One interesting observation is that the rates tend to split into two groups based upon the loading rate. One group contains the faster loading rates of three and five minutes, while the slower rates belong to the other group and evidences that creep could play a role in loading rates exceeding five minutes. This test was run twice, where the

second test reversed the order of the loading rates to see if this was a factor in the results. Both test periods experienced only a 0.5% maximum difference at the end of the loading periods.

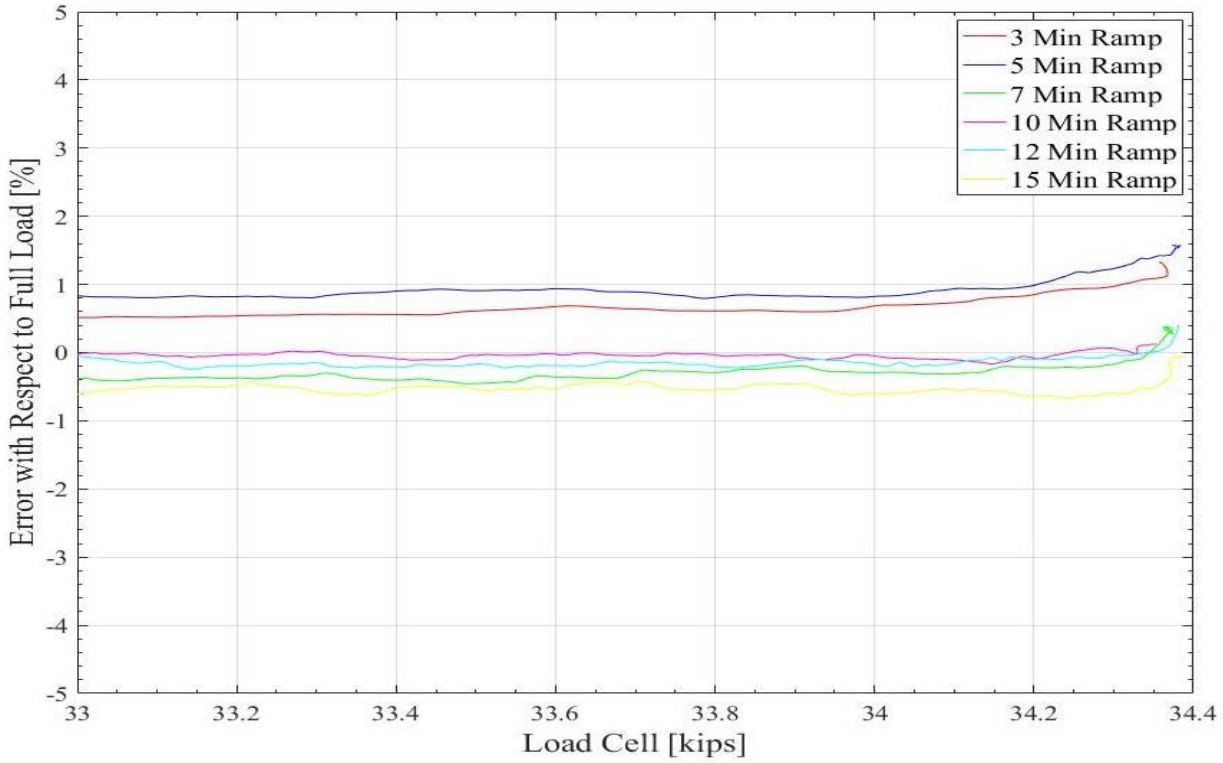

Figure 54. Adapter B Ramping Test Results, End Portion

After the initial ramping test was conducted, additional research was done into industries other than that of grain, which proved that the loading rate provided by Amsted Rail™ was slow compared to the norms of the majority of industries. The fastest rate that was found was 35 seconds to go from an unloaded to fully-loaded state. The fastest our system can achieve was 18 seconds. Therefore, to include the 35 second loading time into the range of testing, the 18 second loading time was selected as the new starting point of the "fast ramping test." The five-minute ramp, as the theoretical cutoff point for the creep factor was selected as the slowest rate. The results of the fast ramping test on Adapter B can be seen in Figure 55.

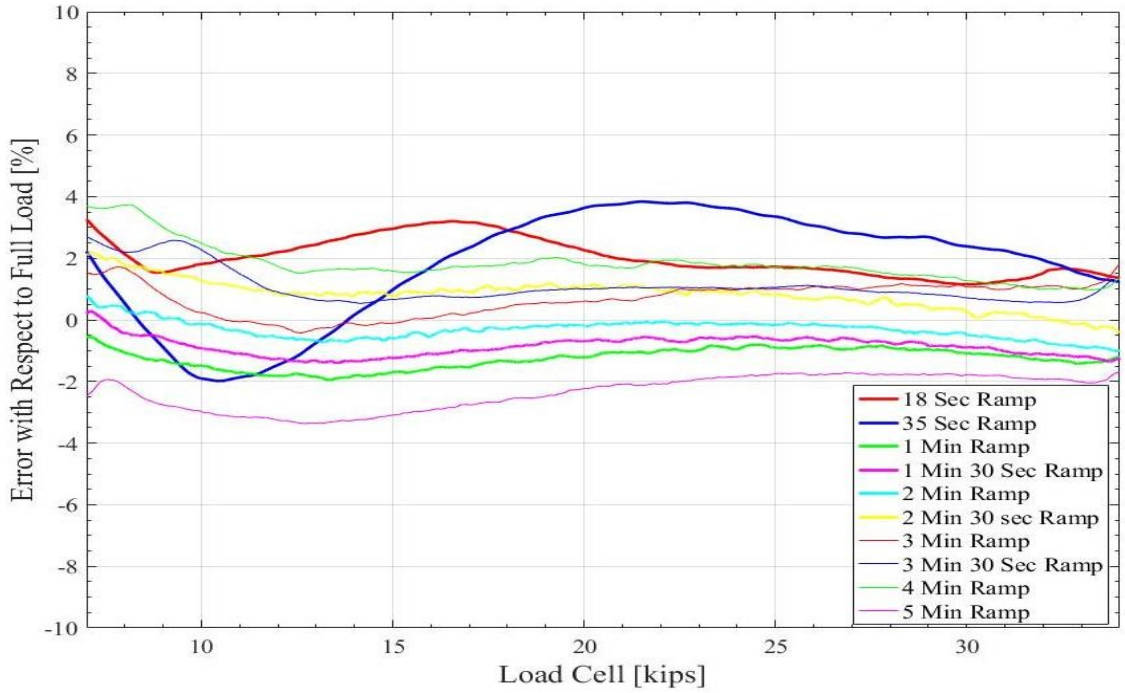

Figure 55. Adapter B Fast Ramping Test Results

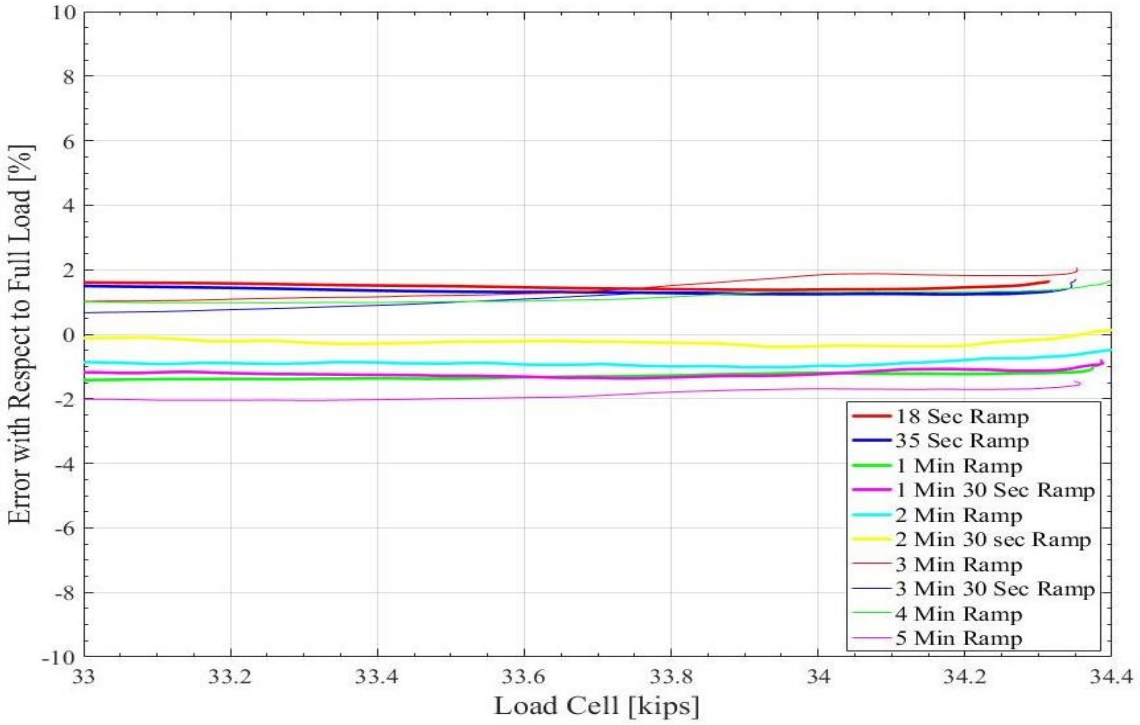

Figure 56. Adapter B Fast Ramping Test Results, End Portion

The zoomed portion of the results of Figure 55 from 33 kips to 34.4 kips (133 kN to 153 kN) can be seen in Figure 56. The maximum cutoff error, that when the train is fully-loaded, is that of the three-minute ramp, which displayed an error of approximately 1.99% and the range of error was -1.54% to 1.99%.

3.3.4 Adapter C

Only the fast ramping test was conducted on Adapters C and D. The results for the full Adapter C ramping test is shown in Figure 57. It can be observed that the effect of the third order correlation is clearly present in the faster loading rates. This figure exemplifies why a second order correlation was not chosen for the primary correlation of the loading tests.

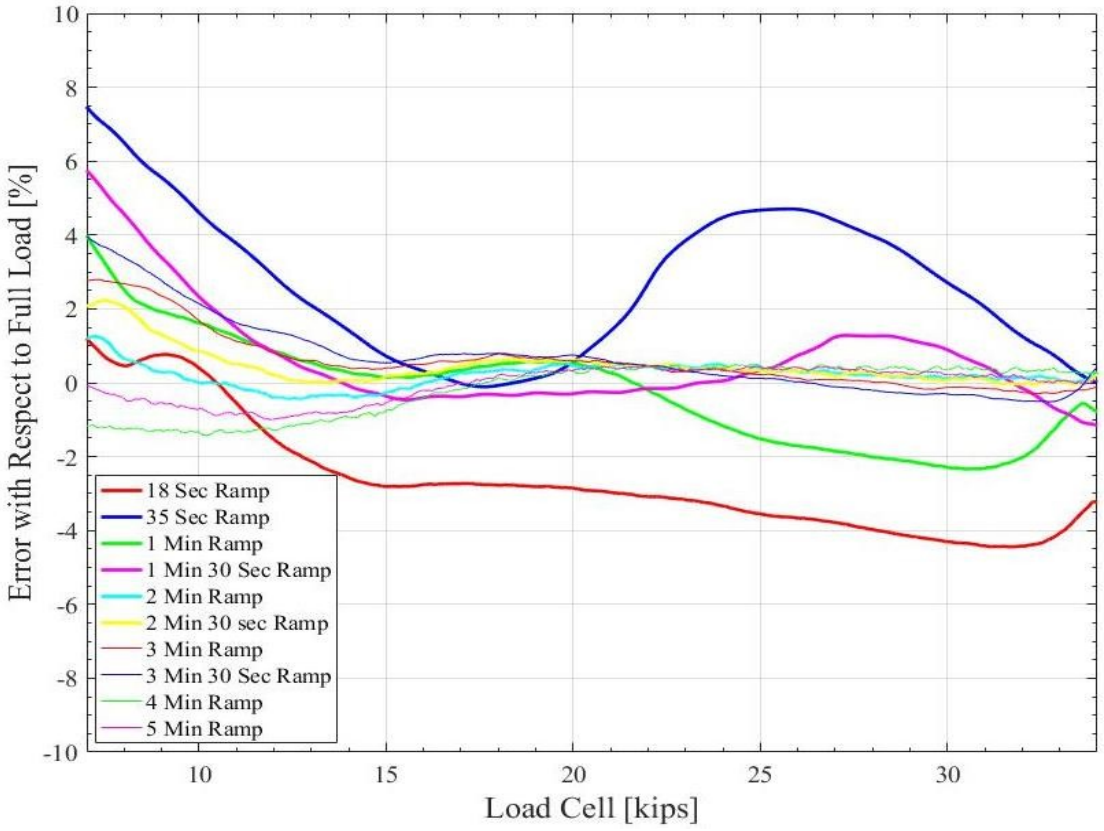

Figure 57. Adapter C Fast Ramping Test Results

The zoomed portion of the results for Adapter C can be seen in Figure 58. The range of error for the fast ramp test of Adapter C was -3.07% to 0.51%. The most interesting observation of this figure lies in the fact that the 18 second ramp predicts the load early for Adapter C and has a large increase in cutoff error (-3.07%) when compared to the results for Adapter B fast ramp testing. This ramp seems to be an outlier as the next highest cutoff error is that for the one-minute ramping rate which has an error of -1.18%.

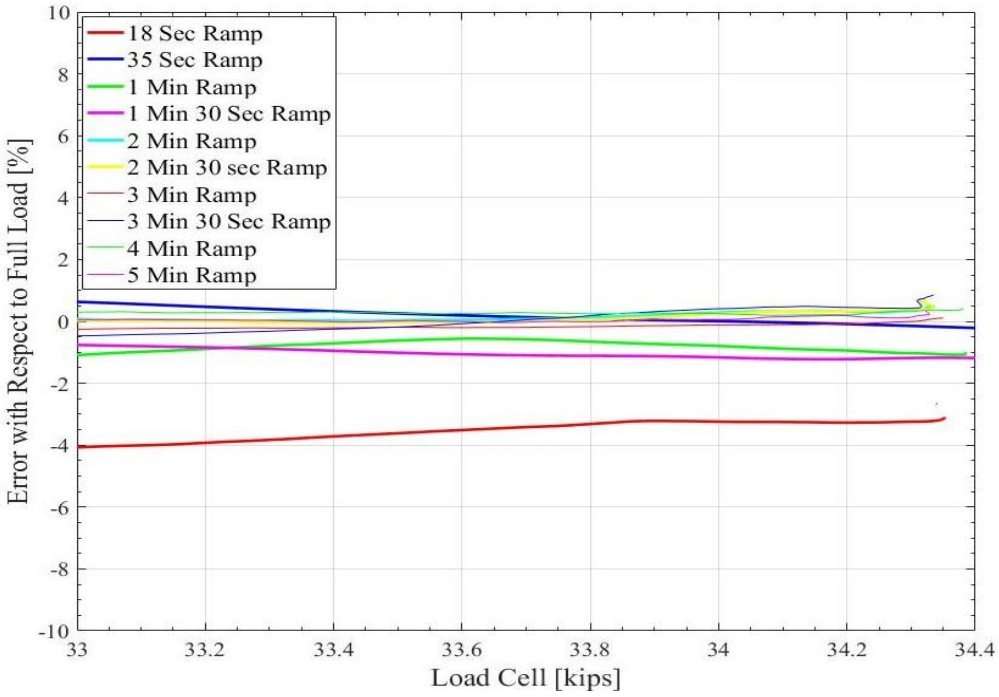

Figure 58. Adapter C Fast Ramping Test Results, End Portion

3.3.5 Adapter D

The results of the ramping test performed on Adapter D can be viewed in Figure 59. It can be observed that the error of the 18 second ramp has a maximum error above 10%, however, it should be noted that the correlation is still able to correct the error at the end of the loading cycle, where the cutoff error of the 18 second loading cycle was below 1% with respect to full load. Figure 60 zooms on the end portion of the results to compare the correlation error with

respect to the full-load with the actual load. The maximum error belonged to the one-minute loading rate, which was -1.69% at the end of the loading period and the range of error for this test is -1.69% to 1.41%.

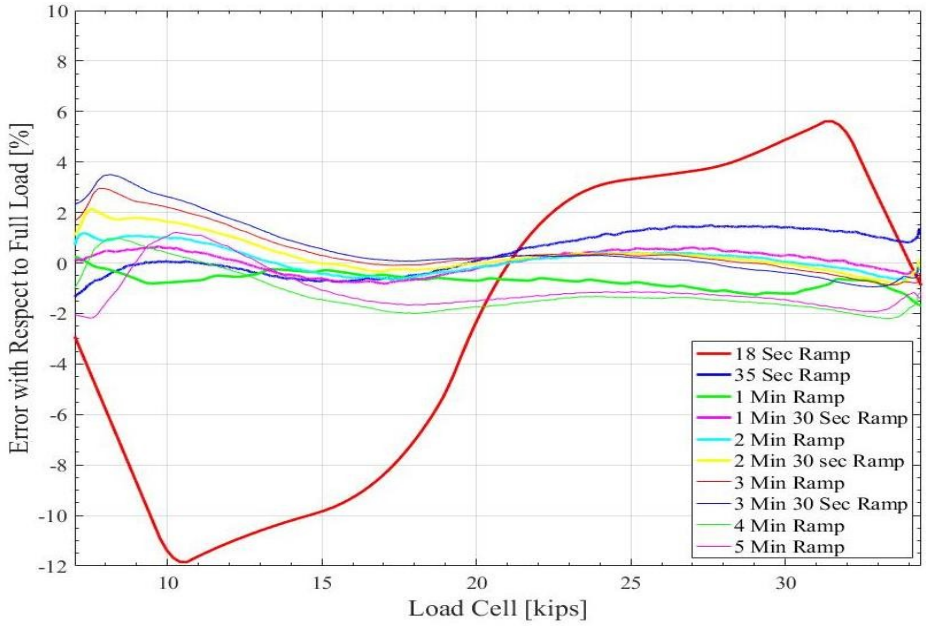

Figure 59. Adapter D Fast Ramping Test Results

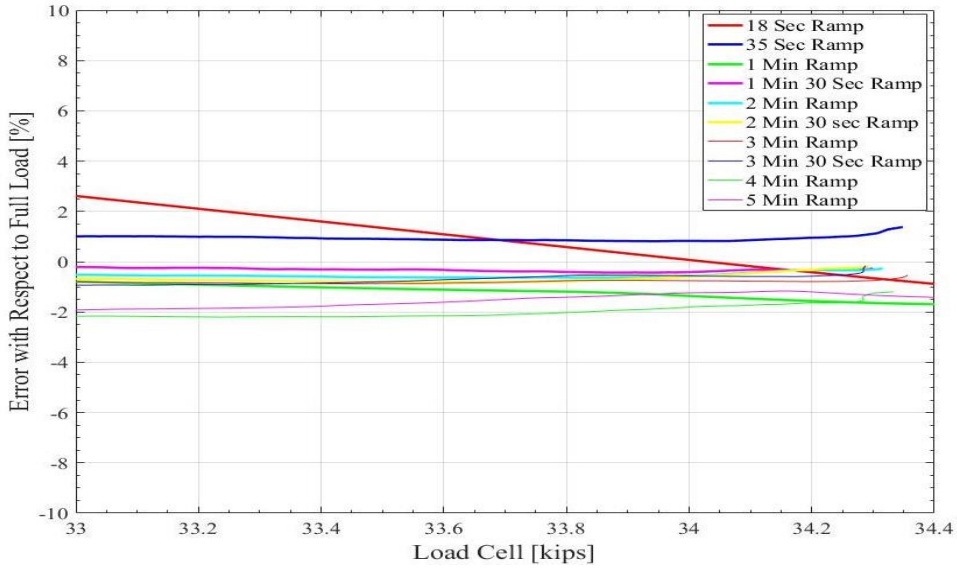

Figure 60. Adapter D Fast Ramping Test Results, End Portion

3.3.6 Sensor Controlled "Ramping" Experiment

Due to the fairly accurate results from the "ramping" tests, further testing was conducted in which the correlation created from the Adapter B fast ramping test was employed in an effort to simulate a railcar loading scenario, whereby the sensor would control when the shutoff of the loading system occurs. A program was created using LabVIEW™ which specified a loading rate and used the output of the load sensor to determine when the simulated loading of the railcar would cease. Using the previously calibrated sensor for Adapter B, the test was situated to run five different ramping rates, from one minute to five minutes. Once the full-load according to the sensor was attained, the system would maintain the load according to the sensor for an approximate 90 seconds. Slight variations will therefore be observed in the short periods after the ramping has ceased. Figure 61 displays the results of the strain-gauge controlled ramping experiment, in which the errors ranged from 3-6%, as demonstrated in Figure 62. Having expected a worst-case error of approximately 2-3%, this outcome prompted further investigation into the reliability, precision, and survivability of the sensor.

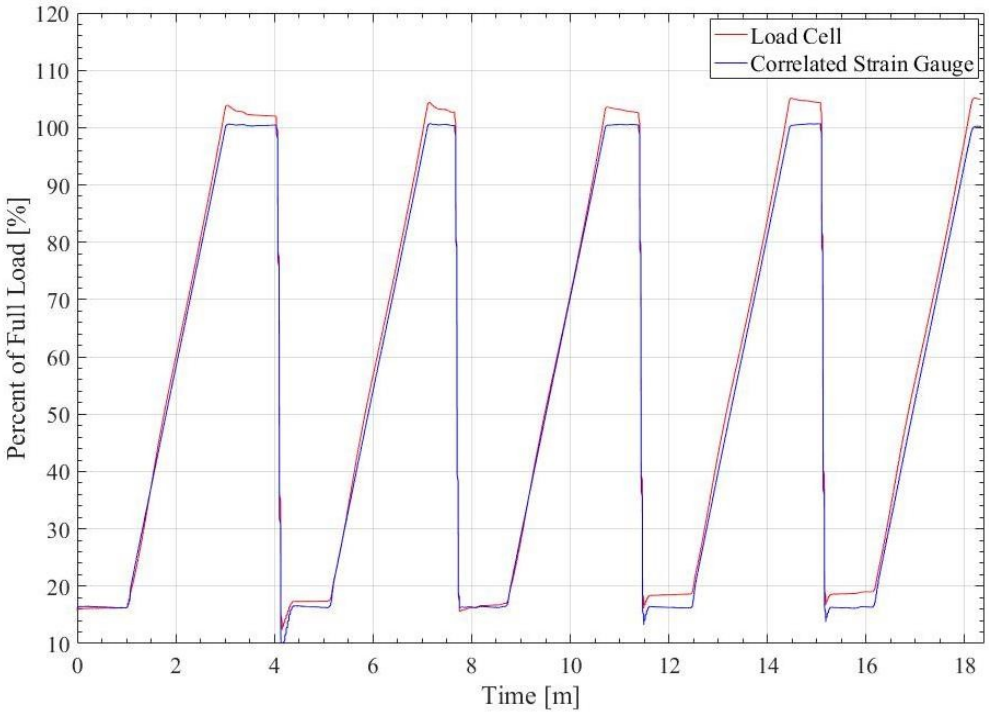

Figure 61. Adapter D Strain Gauge Control Test Results

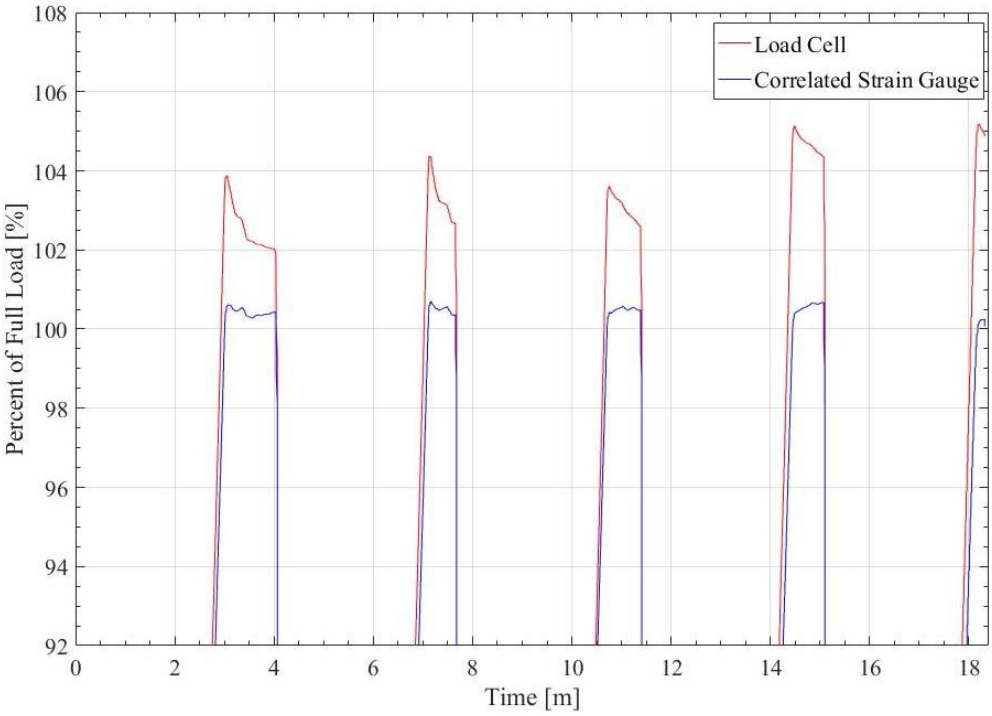

Figure 62. Adapter D Strain Gauge Control Test Results, Upper Portion

CHAPTER IV

ANALYSIS OF RELIABILITY DURING LONG-TERM APPLICATION

4.1 Effect of Impact on Load Signal

After initial testing had been conducted, it was important to ensure that the load insert had the structural capabilities necessary to function in the extreme conditions found in the operation of freight railcars. Some of the most structurally compromising events that occur in rail operations are impacts instigated by wheel flats or rail defects. Wheel flats specifically can develop due to imperfections in the wheel geometry, defects present in the material, or stuck handbrakes.

The rail industry has instituted Wheel Impact Load Detectors (WILDs) to measure the approximate force caused by wheel flats to account for this industry-wide issue. Currently, the Association of American Railroads has noted that wheels that have an impact force above 90 kips (400 kN) are faulty wheels, which was the initial target for testing. However, only a consistent 35 kip (160 kN) impact was achieved. While this system will not be able to fully simulate the severest of wheels that are flagged, it does provide data regarding what would be considered a developing wheel flat [39].

The impact mechanism is depicted in Figure 63, where a rolling rod that operates on a cam is used to compress a spring of a specified constant to release when the cam reaches the end of its stroke. In order to record the necessary data, an accelerometer was employed that utilized

the same data acquisition as that of the load sensor and load cell discussed in Chapter II. The accelerometer, from PCB Piezotronics Inc., was attached to the impact head to measure the acceleration of the mass to derive the impact force imposed by the mechanism. The combined mass of the steel and brass impact head components was 53.37 lb (237 N) and the employed spring had a constant of 200 lb/in (35 kN/m). Data collection for the accelerometer occurred at a sampling rate of 51 kHz to capture the full impact acceleration of the impact head.

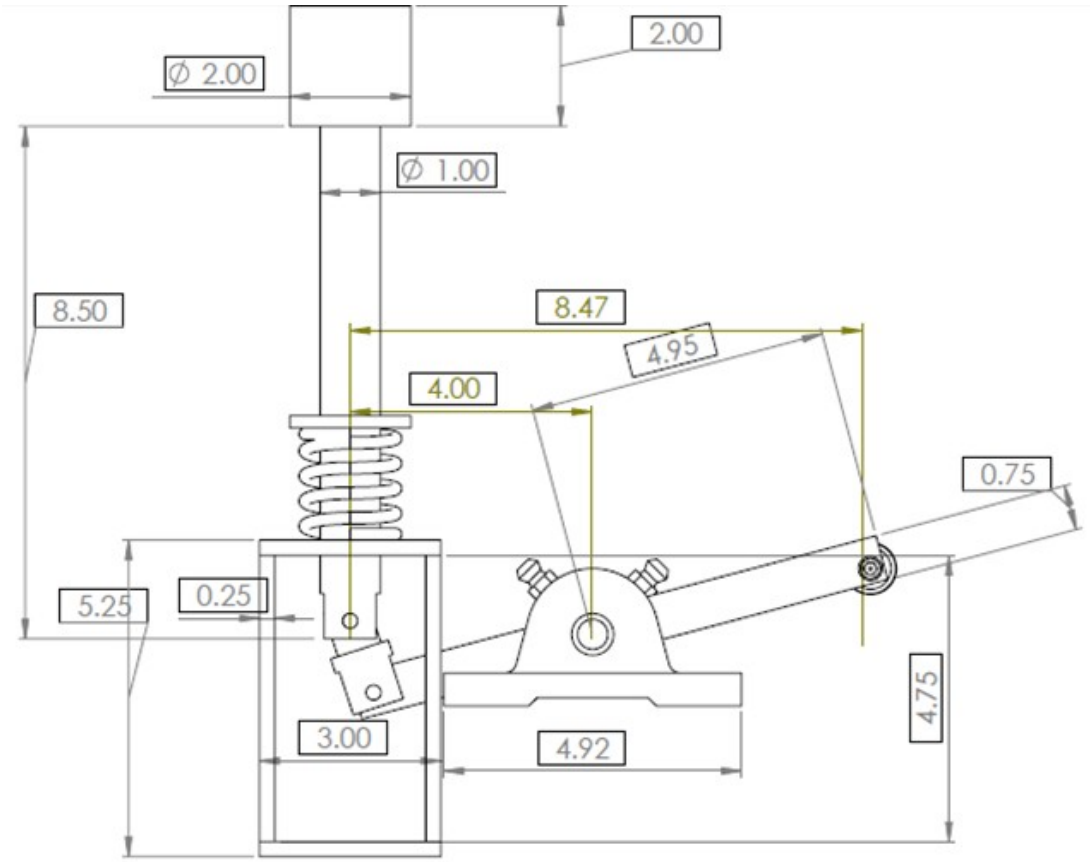

Figure 63. CAD Drawing of Impact Mechanism (dimensions in inches)

4.1.1 Wheel Impact Force Analysis and Load Signal Results

In order to analyze the effect of impacts on the load sensor output, the following experiment was conducted. The adapter was held at full-load and operated at 25 mph (40 km/h)

while impacts occurred at a frequency slightly above 1 Hz. The results of the test can be observed in Figure 64, which exhibits the forces that occur due to the impact mechanism and their effect on the correlated output of the load sensor. A maximum force of 44 kips (196 kN) was attained. The correlated output of the sensor is demonstrated to not be affected by the impact of the mechanism. It can be assumed that due to the data collection frequency (50 Hz), the quick variations in the data that result from the impacts are negated. However, further investigations can be conducted which employ a faster data collection frequency and incorporates a spring with a larger constant to determine at what frequency the impacts will affect the sensor. It should be noted that the sensor was unharmed despite the extreme forces applied to the system.

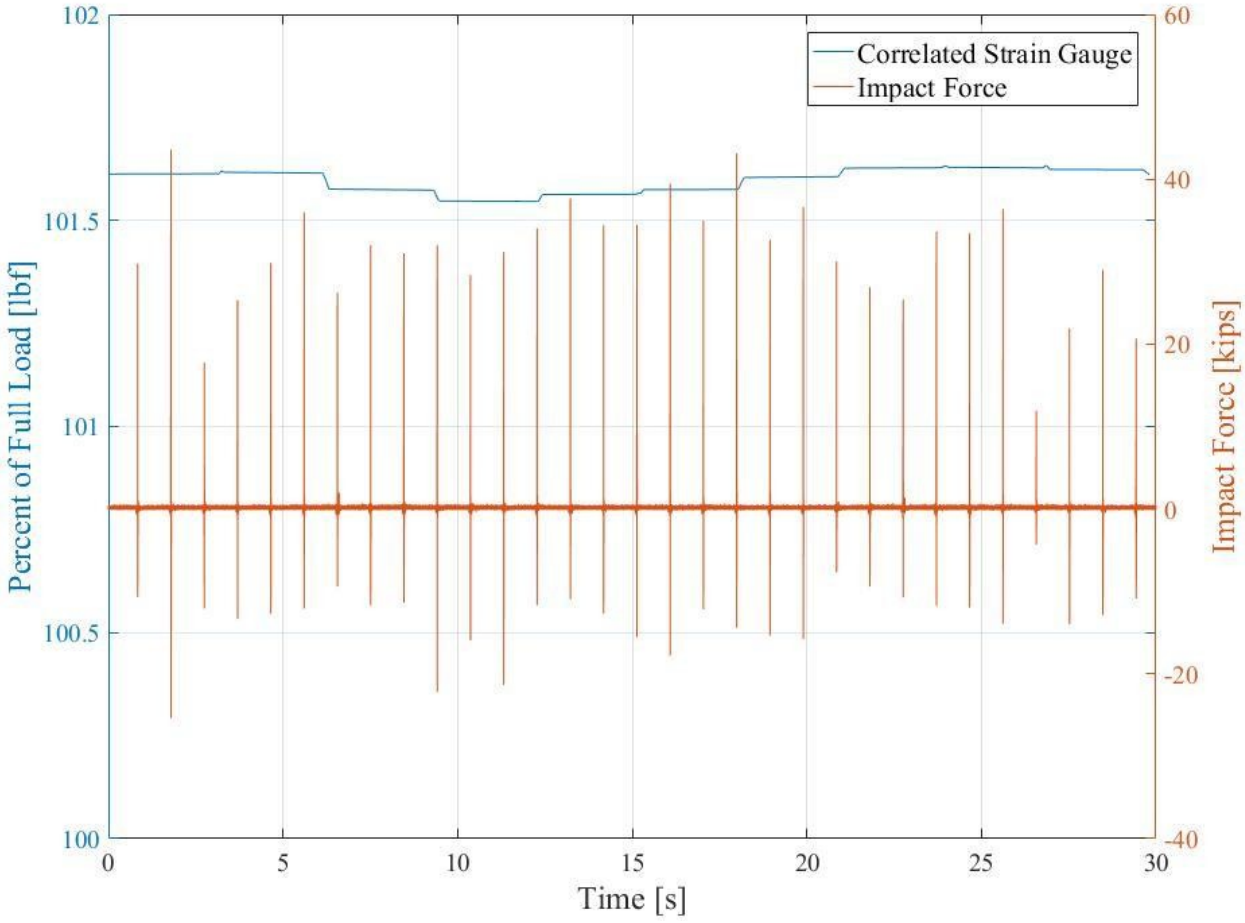

Figure 64. Impact Force of Impact Testing

4.2 Analysis of Mounting Method

The development of the load sensor arrived at a milestone in which the results were consistently accurate. It was discovered, however, that the output received from the data acquisition system after completely unloading the bearing and reloading it to 100% full-load would have a voltage difference present which would result in over 5% error post-calibration. This was theorized to be due to a difference in the loaded pressure distribution in the steering pad, where a slight alteration of the position of the component can result in a shift of the effective distribution of stress in the pad. In an effort to improve the precision of the sensor, two mounting methods were evaluated. Mounting the sensor to the adapter was additionally considered a natural progression as the sensor and adapter would most likely be sold as a pair due to the variables involved in the calibration and implementation.

Post-mounting tests were conducted to evaluate the effect the different mounting methods had on the sensor output. This testing was conducted under static conditions over a two day period. This form of testing was similar to that conducted in Chapter III under the static portion of the load accuracy tests, except that the test was shortened to approximately 7.5 hours. After the first day of testing, the adapter was removed from the assembly and allowed to readjust. The testing conducted on the first day was used as the basis for a second-order calibration which was imposed on the output of the second day of testing. The error of the root mean square of the load difference between the correlated and actual load of the second day of testing is taken with respect to the full-load and displayed in the results for each section. The results for the “free floating” sensor can be observed in Table 5 for comparison.

Table 5. “Free Floating” Analysis

Percent of Full-Load (%)	Error (%)
80	5.34
100	4.36
80	4.81
100	5.02

4.2.1 Bolt-Mounting

The first method considered was mounting the sensor to the Smart Adapter© by threading holes in which mounting bolts could be attached, as shown in Figure 65. Once the machining processes began, however, numerous issues were encountered. The first, but most easily mended, was the sensor housing welds becoming compromised by the reactive forces involved in the milling application, which was due to the inserts being welded previous to the drilling of the mounting positions. This issue resulted in a total reconstruction and positioning of the insert and sensor components. The second and more pressing issue was the effect that using mounting screws had on the data output and its relationship to the load application.

The results of the bolt-mounted insert using four mounting bolts can be observed in

Table *6*, where the results of the testing are shown. The load step errors for the testing are shown in the right column of the table. The high error involved was attributed to the unforeseen bending force applied by the tightening of the mounting bolts on the load sensor, rendering this method of mounting undesirable.

Table 6. Bolt-Mounted Analysis

Percent of Full-Load (%)	Error (%)
80	2.24
100	2.64
80	3.28
100	3.18

Figure 65. Bolt-Mounted Sensor

4.2.2 TIG Weld-Mounting

The next method considered was TIG welding the insert to the adapter using ER70S-6 welding alloy, as shown in Figure 66, which was not the primary method of choice considering the detrimental welding properties of A2 tool steel. When welding tool steel to other materials, the welds will have difficulty creating a joint between the two components. However, all the welds properly formed and besides the presence of surface cracks and the heat involved in the processing, the welding method itself contained no significant drawbacks. An aluminum heat sink was used to resolve the heat of the welding in a process similar to that of the actual construction of the sensor and the surface of the welds were refinished to eliminate any chance of crack propagation.

The results of the testing for a TIG weld-mounted insert with four welds is displayed in Table 7. It can be observed that the error of the implemented calibration is much less than that of the bolt-mounted insert. For the bolt-mounted insert, the most severe error was the second 80% step (3.28%). The weld-mounted inserts experienced a maximum error of 3.07%, which occurred on the first 100% step load. This error is still fairly large and needs to be studied further, however, the weld-mounting proved to be the best method and benefitted the sensor output. Therefore, adapters utilizing both four and eight welds were created.

Because the bolt-mounted inserts were deemed insufficient due to the unfavorable bending stresses imposed by the tightening of the mounting bolts, each adapter that had been purposed for bolting was repurposed with welds as shown in Figure 67. Shims were additionally implemented in an effort to ensure all the sensors were twelve one-thousandths of an inch (0.305 mm) above the adapter surface.

Figure 66. Weld Mounted Sensor

Table 7. Weld-Mounting Analysis

Percent of Full-Load (%)	Weld Error (%)
80	1.45
100	3.07
80	1.19
100	1.33

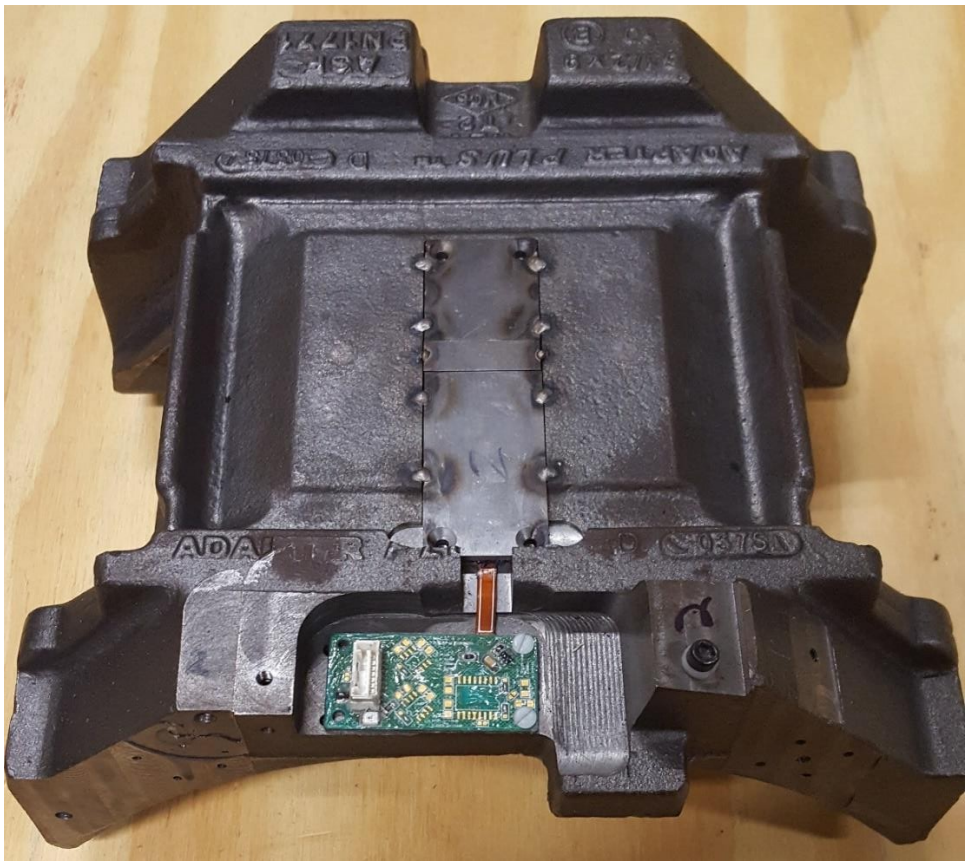

Figure 67. Repurposed Bolt-Mounted Sensor with Eight Mounting Welds

4.3 Weld Fatigue Analysis

4.3.1 Theoretical Fatigue Analysis

To further investigate the effect of the extreme forces found in railroad bearing operation that would be imposed on the chosen mounting method, a theoretical fatigue analysis was conducted. Fatigue fractions begin with a minute crack at a local high stress area and the resulting failure results from repeated plastic deformation and occurs over many cycles of yielding often existing at the microscopic level [41].

The assumptions for the welded material and the loading properties are shown in Table 8. The analysis operated under the assumption that an eighth of the full weight of a railcar utilizing a Class K bearing was distributed evenly across the adapter pad surface, which was assumed to

be 4.4 in x 7.7 in (112 mm x 196 mm). Because we were analyzing the pure shear scenario, which would be the most likely loading scenario to initiate a crack, a friction factor of 0.4 was used, which is an overestimation for most plastic-metal cases. These assumptions equate to a distributed shear stress of 406 psi (2.8 MN/m^2), which is incredibly unlikely as the majority of the pressure is typically distributed across the interlocking ridges as determined by the pressure film analysis conducted by Diedrich [25].

Fatigue analysis additionally makes use of correctional coefficients for characteristic properties. The welding material has a yield strength of 65.5 ksi (452 MPa). Each of the welded areas were assumed to be in torsional load cycles and have a "hot rolled" surface. The torsional loading condition was chosen because of the pure shear assumption mentioned previously. According to empirical data [41], hot rolled surfaces with an ultimate tensile strength of 78 ksi (537 MPa) have a surface factor of approximately 0.65. The load factor for torsion is 0.58 and the gradient factor was assumed to be 0.9.

Table 8. Properties and Assumptions for Fatigue Analysis

Material and Loading Properties	
Ultimate Tensile Strength	78 ksi
Yield Strength	65.5 ksi
Surface	Hot-Rolled
Loading	Torsion

The results of testing are displayed in Figure 68. The infinite life threshold stress at the designated pressure distribution is 13.2 ksi (91 MPa), which indicates that there is a factor of

safety of over 25 for the welded area. According to this model, the welds, if attached properly with no cracks, should never break.

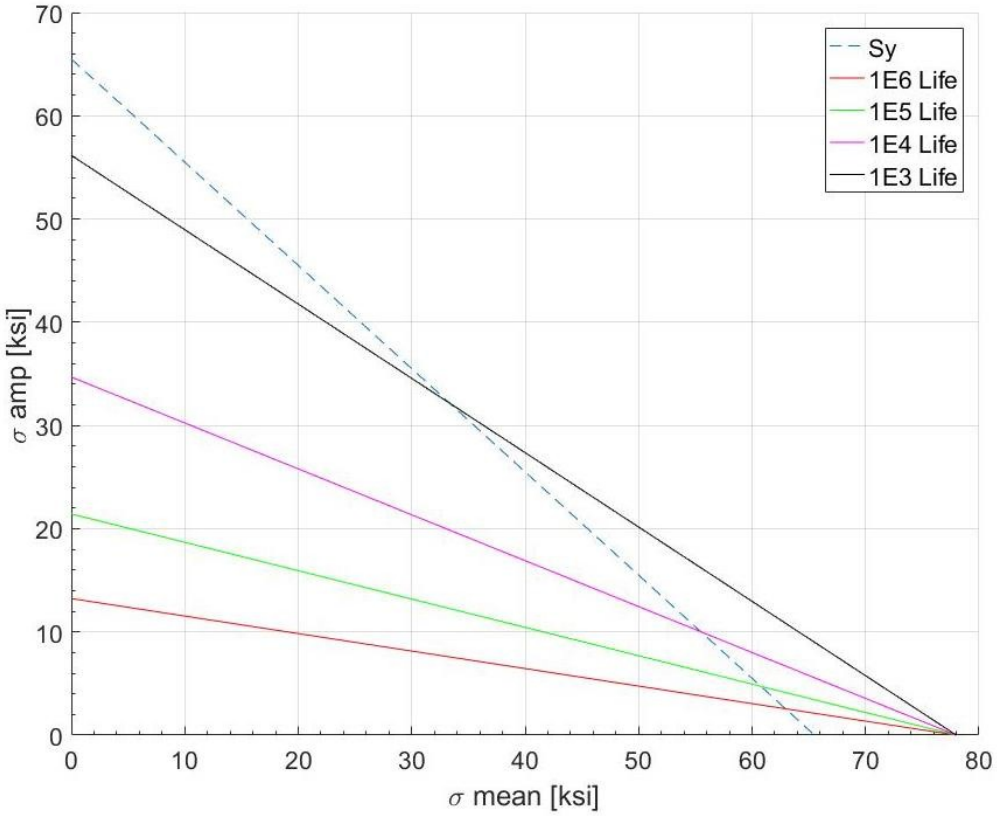

Figure 68. Results of Theoretical Fatigue Analysis

4.3.2 Finite Element Analysis

Finite Element Analysis (FEA) has been an essential tool for many engineering disciplines since its inception in the 1940s when Hrennikoff and McHenry utilized a series of elements to obtain solutions for the behavior of various solids. In its infancy, it was used primarily as a structural analysis tool, but over time it has been improved and applied to more engineering disciplines. FEA takes complex problems and separates them into smaller, more manageable subsets. These subsets are analyzed and the collection of results provide a realistic approximation of how the structure would behave under the presence of specified forces,

pressures, and boundary conditions. It can be used to provide insight into the expected mechanical performance of different assemblies and its impact on functional safety [42].

In Algor FEMPRO™, a variety of tests including: linear stress analysis, nonlinear stress analysis, and steady-state heat transfer can be used to evaluate different assemblies or components. The FEA approach for the purposes of this thesis utilized a linear stress analysis for the models regarding the weld-mounting of the sensor.

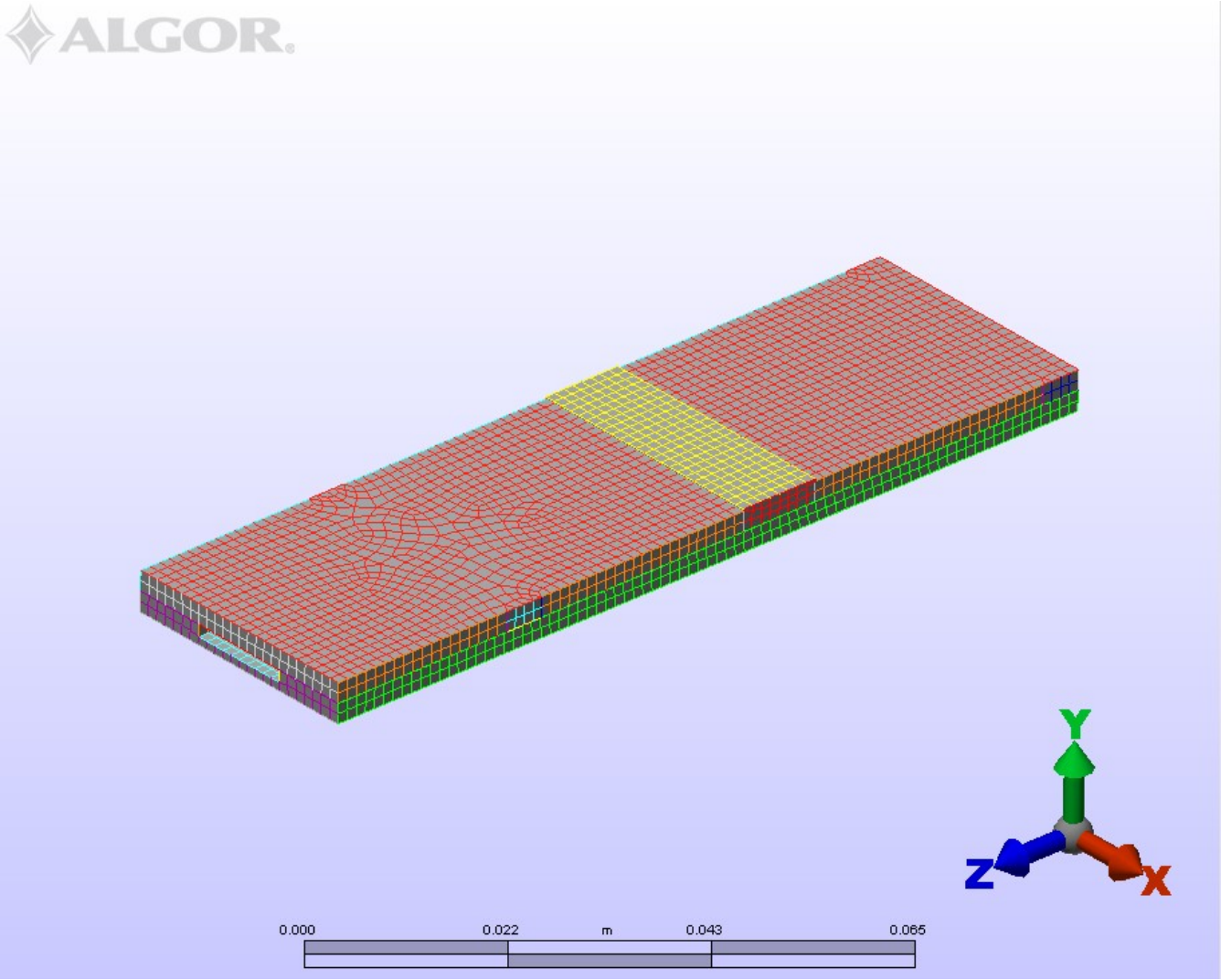

Figure 69. FEA Mesh Analysis

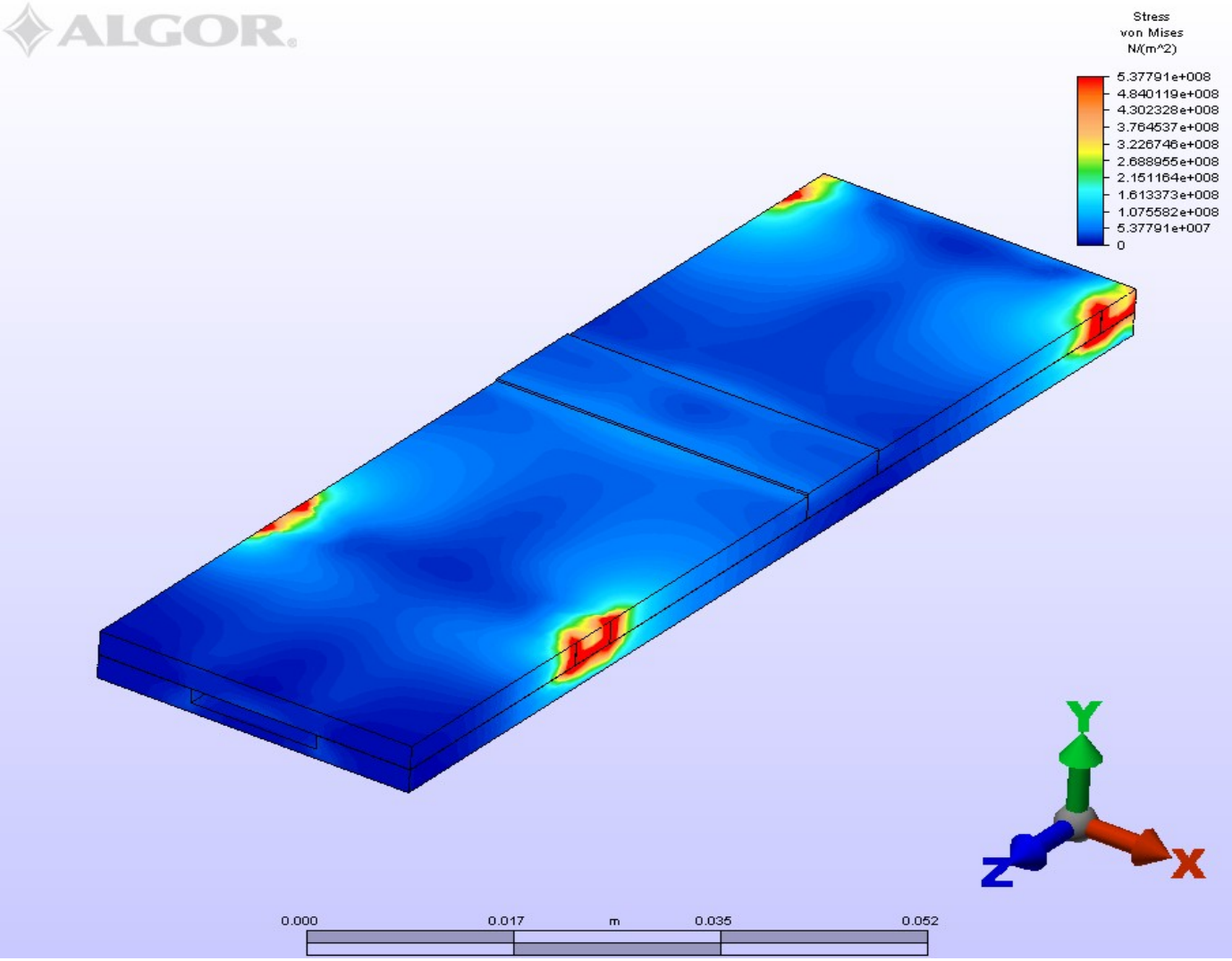

Figure 70. FEA Results

To verify the survival of the mounting procedure, a study of the structural integrity was necessary. Finite Element Analysis (FEA) was chosen as the secondary means of verification. A four-weld mounted sensor model was created and evaluated. The material parameters are input into the model and certain boundary conditions are imposed. When employed in the field, the welds would most likely fail due to the shear stresses imposed by the steering pad when the railcar enters a curved section of track. Therefore, the model was assumed to be in complete shear having the full load distributed across the surface of the sensor with no loss due to friction,

the most extreme and a non-plausible scenario for the sensor if employed in the field. The welds were assumed to fill 0.2” of the side of the sensor.

The preliminary studies required appropriate boundary conditions to obtain realistic results for the proposed model. The welds were each assumed fixed, with no rotation or translation. Additionally, the sensor was fixed in the X and Z directions to simulate walls of the adapter canal, as well as the negative Y direction to simulate the bottom of the adapter canal. The mesh used to conduct the FEA can be observed in Figure 69. The results of the analysis can be seen in Figure 70. A slight alteration of the mesh can be observed in the area of the welds, which is largely due to the amount of elements used in the analysis. In the worst case scenario, the maximum stress would be equivalent to the ultimate tensile strength of the weld material (78 ksi or 538 MPa). However, if eight welds were implemented, the welds would not fail under the most hyperbolized circumstances.

4.4 Reliability Analysis of Load Insert

As discussed in Chapter III, the precision of the sensor was questionable as left in its “free floating” assembly. To evaluate the precision of the weld-mounted sensors, tests were designed to demonstrate hypothetical “field employment” scenarios and exhibit the performance of a pre-test calibrated sensor under numerous loading cycles. In the case that a leak or shifting in freight occurs during transportation, small variations in the load would occur. To account for these scenarios, this portion of testing was conducted without the use of the load controller to let the thermal expansion of the hydraulic fluid account for the minimal alterations in load. A load accuracy test was used as the basis of calibration for the tests that follow. The tests performed utilize a control bearing with no noticeable imperfections and a spalled bearing which is used to demonstrate the integrity of the sensor and its signal under the spall-induced vibration. The

testing will be displayed in weeklong increments to have the resolution necessary to observe the demonstrated trends. All testing employs Adapter B which was fabricated with eight mounting welds. In the following sections, the "loaded" error refers to the "average error" at loads above 90% of full-load.

4.4.1 Control Bearing

The first set of testing was performed on the test rig using signal conditioning box B-2 and the rod-end load cell. This test utilized a control bearing, focusing solely upon the precision of the welded sensor of Adapter B. The three-week test concentrated on loads above 90% of full-load with the axle rotating at a speed equivalent to 25 mph (40 km/h). Figure 71 gives the overview of the three-week test as observed by the load cell.

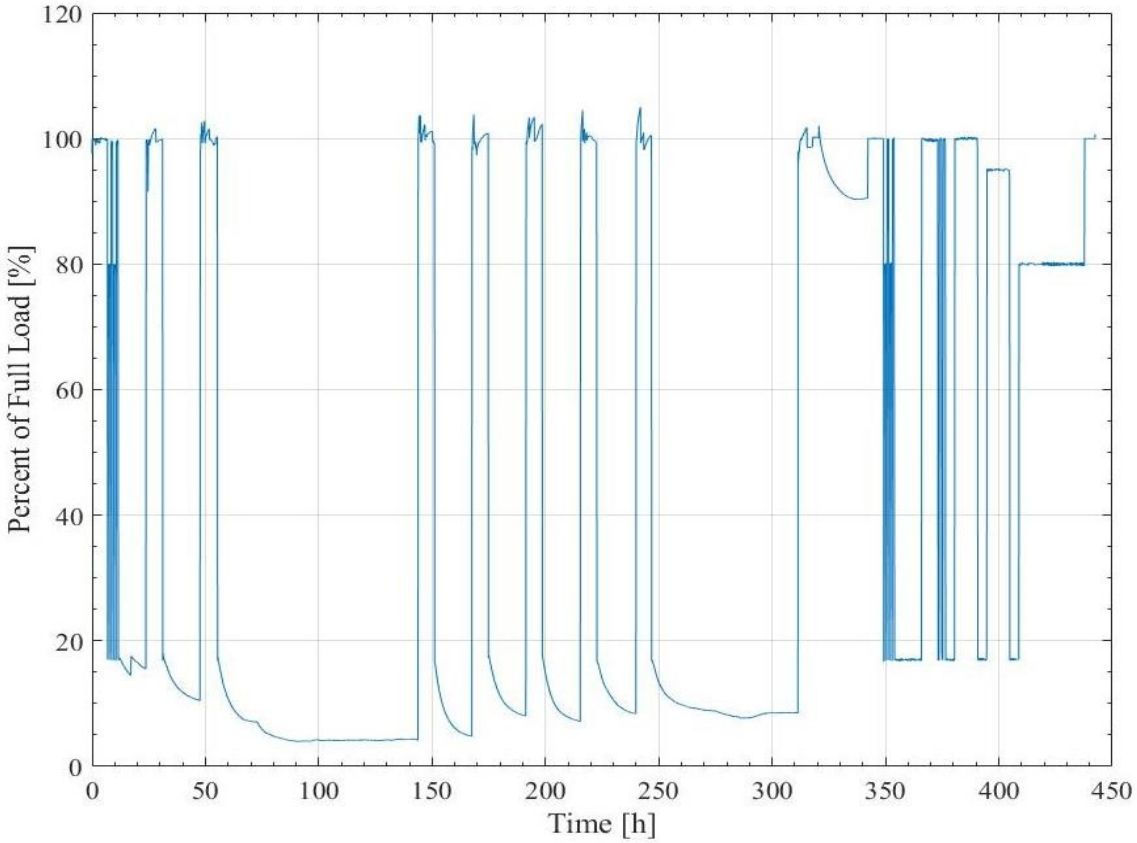

Figure 71. Reliability Testing on Control Bearing

Figure 72 displays the first week of testing using the second-order correlation. It can be observed at the beginning of testing that the short duration of 80% and 100% alternating static steps displayed a large amount of inaccuracy. The average error for the full week utilizing the second-order correlation, however, was within the desired tolerance at 0.96%. Figure 73 displays the multivariate counterpart of the test. The average error throughout the first week of testing displayed by the multivariate correlation is 0.98%, however, when evaluating only situations in which the load is above 90% of full-load, the error of the second-order correlation for the first week of testing increases to 2.79% and the multivariate increases to 2.33%. Surprisingly, both sensors were able to accurately reflect the lower loads to a high degree of accuracy.

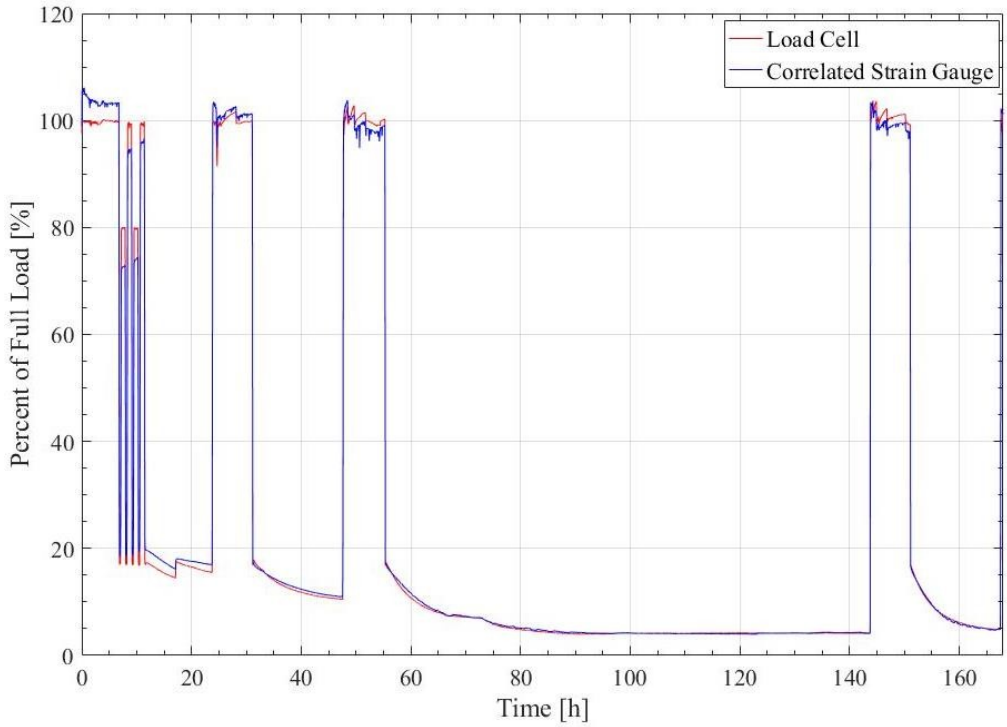

Figure 72. Control Bearing, Week 1, 2nd Order Correlation

Figure 74 displays the results of the second week of testing utilizing the second-order correlation method. It can be observed that towards the end of the testing period shown, a

significant amount of variation is detected which is additionally found in the multivariate correlation, displayed in Figure 75, and indicates that the voltage output is the primary cause for the variation. The amount of variation remains approximately the same for both, in which the average error throughout the week testing period is 0.91% for the second-order correlation and 0.87% for the multivariate correlation.

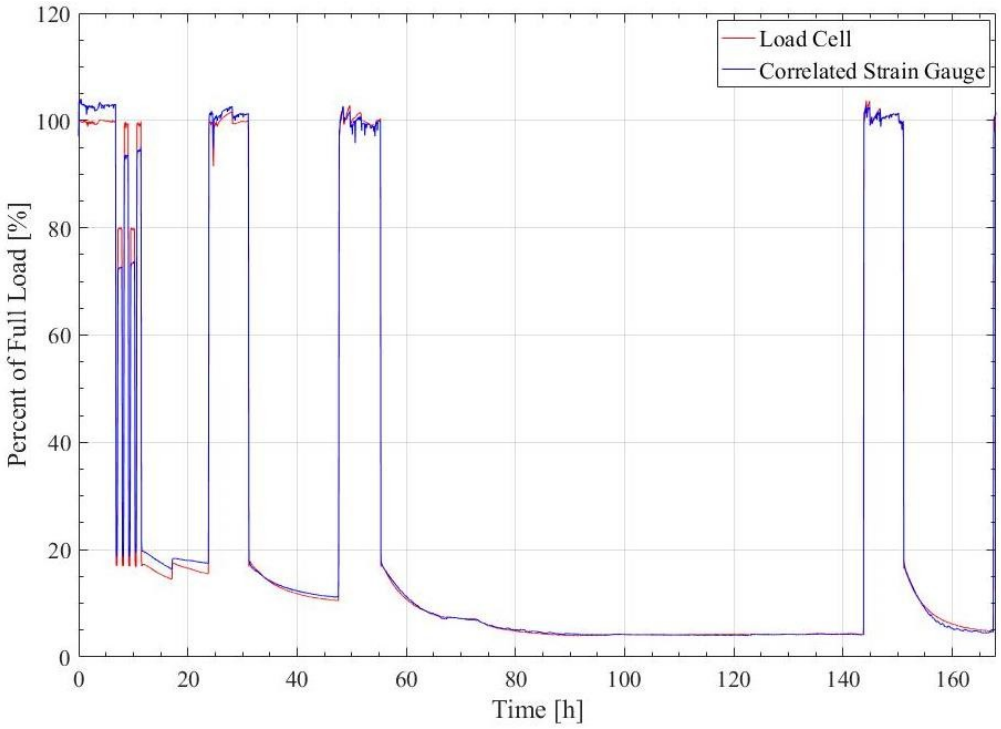

Figure 73. Control Bearing, Week 1, Multivariate Correlation

Figure 76 shows the third week of testing utilizing the second-order correlation, which displayed an average error of 2.94%, which increases to 5.55% when only accounting for test portions exceeding 90% of full-load. Contrastingly, Figure 76 displays the advantage of the multivariate regression, where the temperature accounted for a large amount of error, decreasing the test period average error to 1.22%.

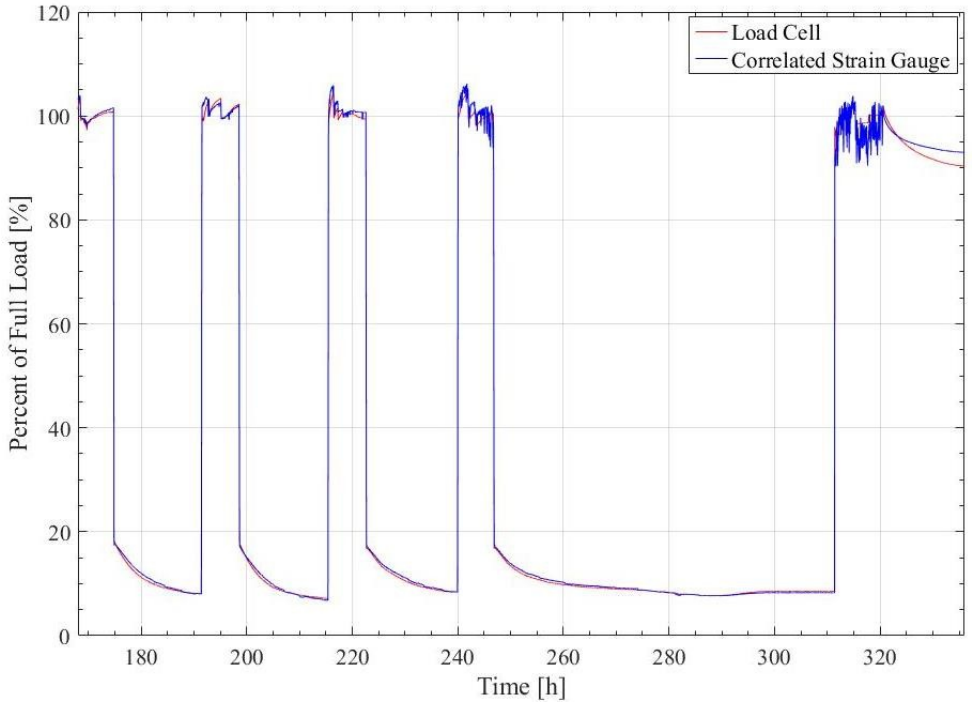

Figure 74. Control Bearing, Week 2, 2nd Order Correlation

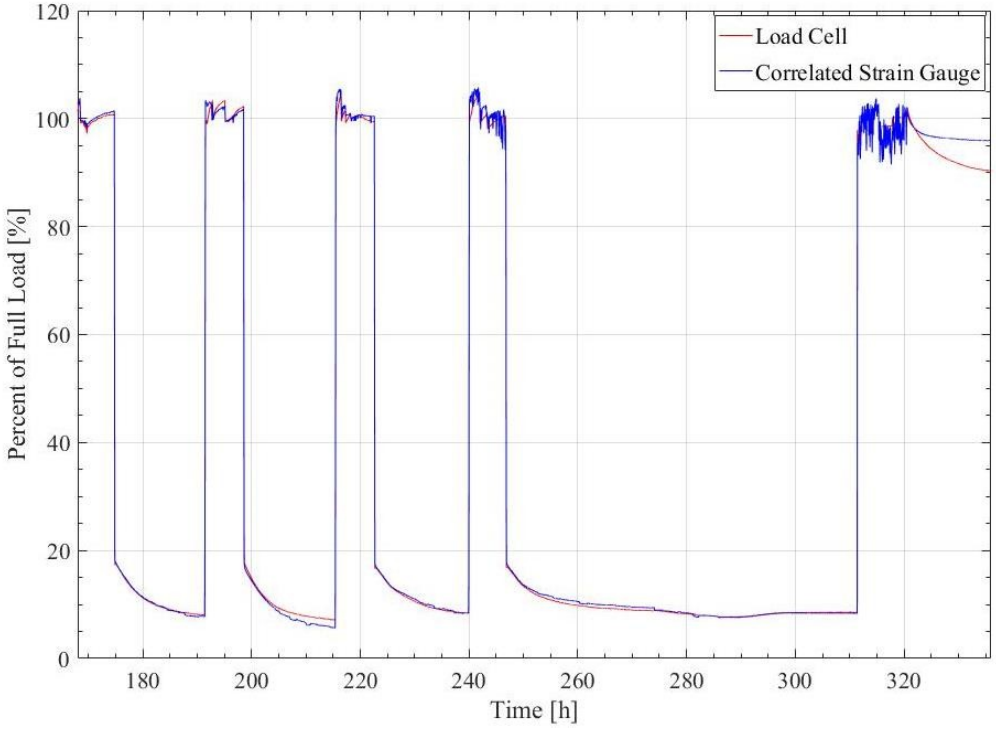

Figure 75. Control Bearing, Week 2, Multivariate Correlation

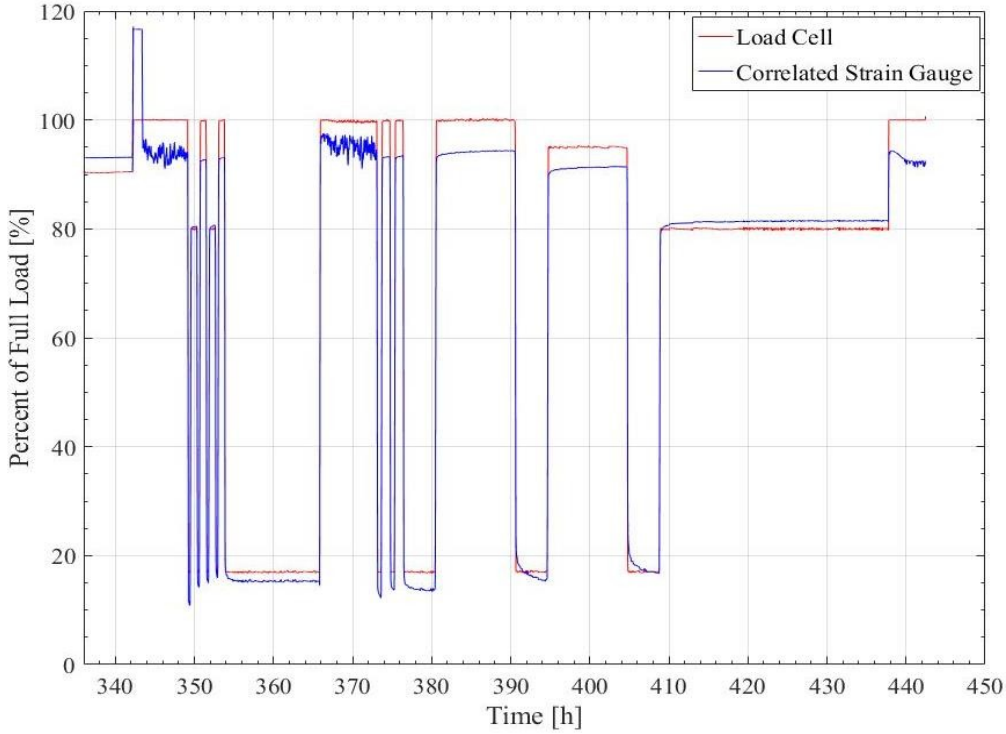

Figure 76. Control Bearing, Week 3, 2nd Order Correlation

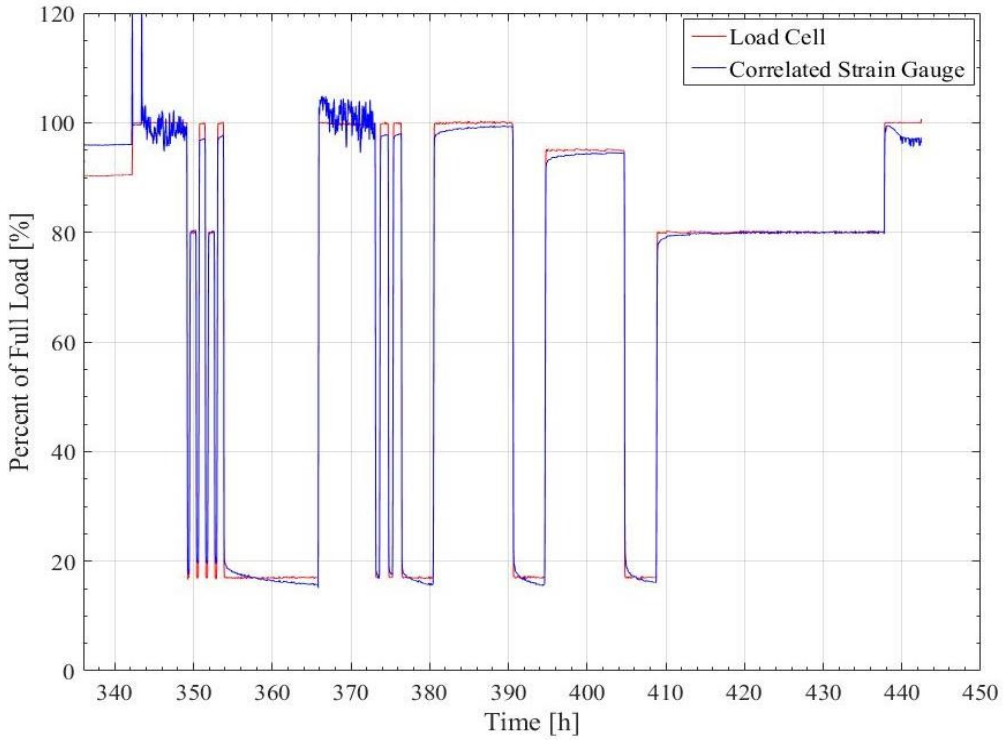

Figure 77. Control Bearing, Week 2, Multivariate Correlation

4.4.2 Spalled Bearing Test 1

The set of testing utilizing a spalled bearing was conducted for over a one month period. The overview of the first set of testing using the spalled bearing can be observed in Figure 78. As can be seen, this test concentrated on the effect the vibration induced by the spall in an unloaded environment would have on the data output and signal processing. While the inaccuracies are discussed, this was considered to be, primarily, a structural test.

Figure 79 shows the first week of testing using the second-order correlation, which had an average error of 1.74%. Figure 80 shows the first week of testing using the multivariate correlation, which had an average of error of 1.65%.

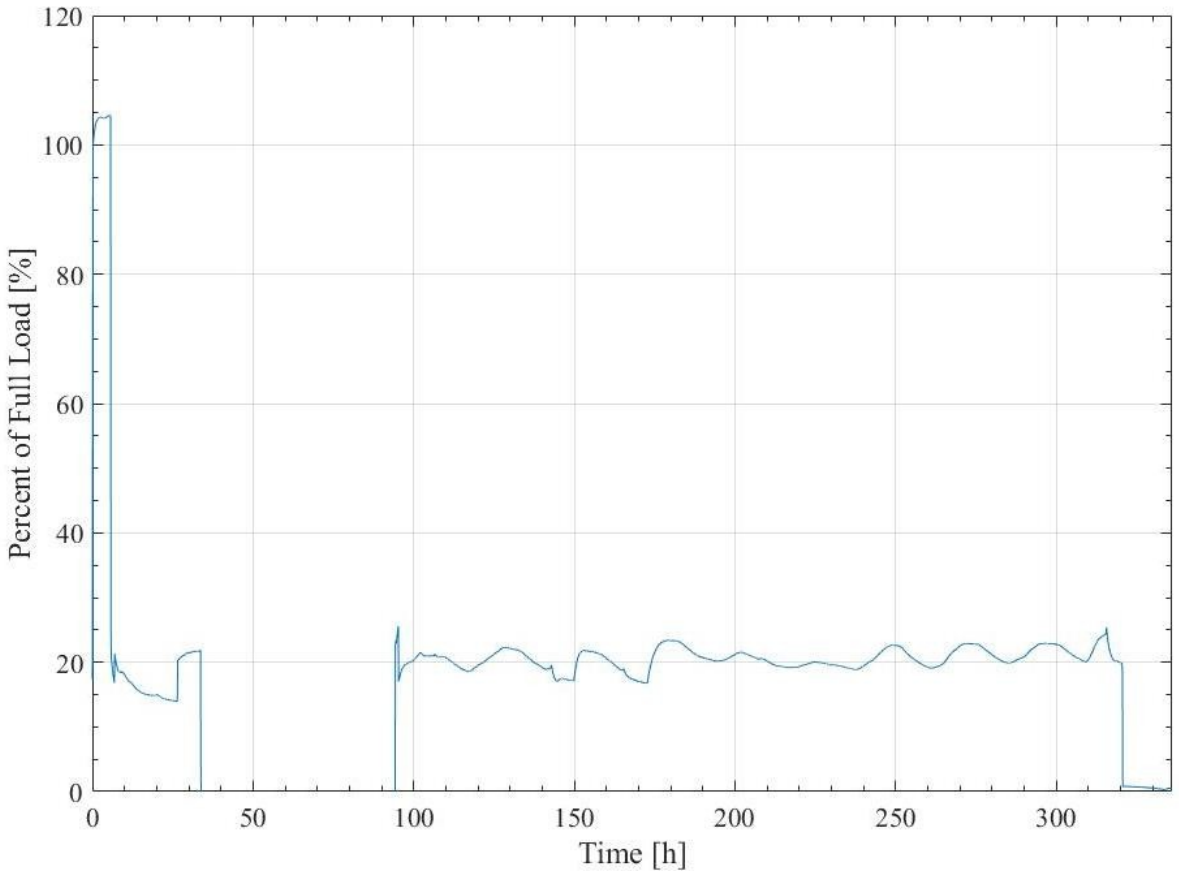

Figure 78. Reliability Test on Spalled Bearing, Test 1

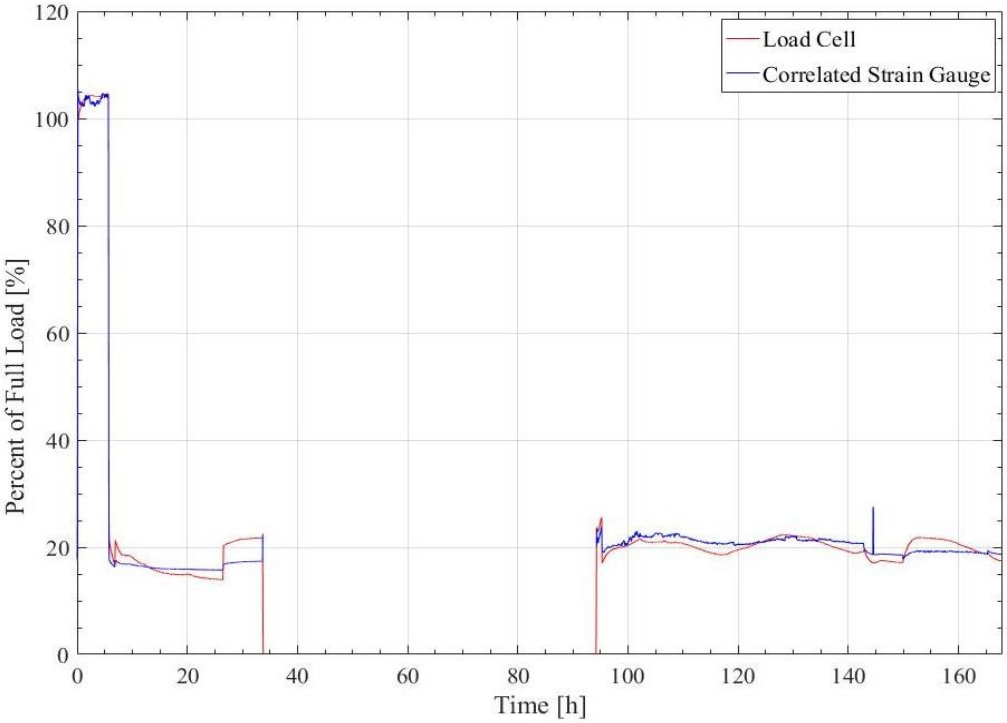

Figure 79. Spalled Bearing, Test 1, Week 1, Second-Order Correlation

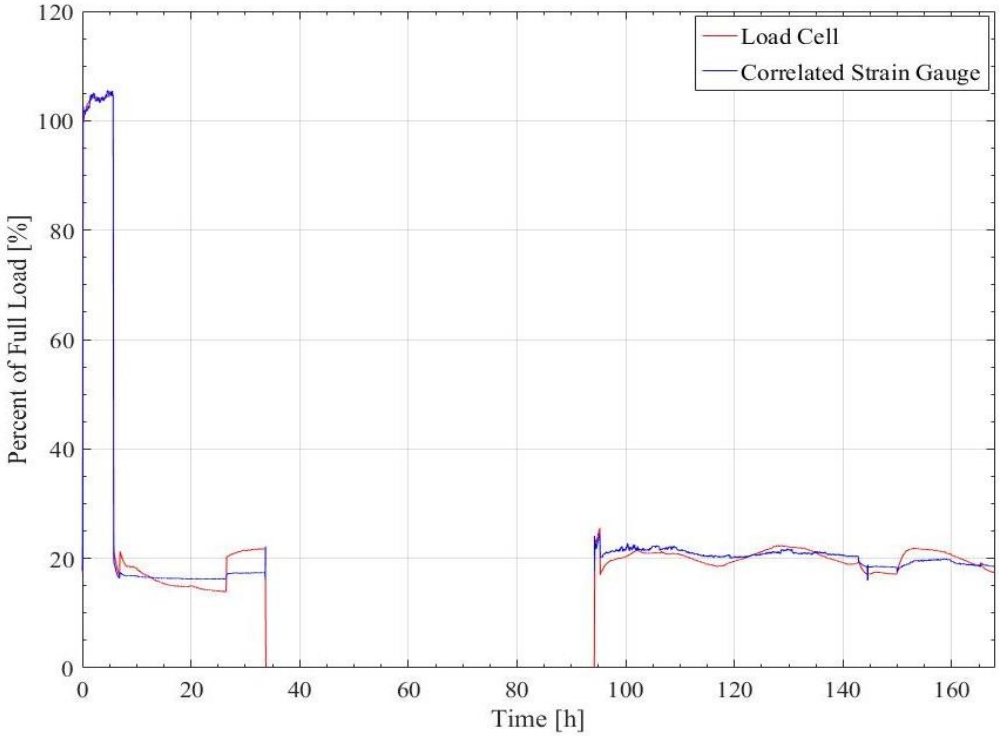

Figure 80. Spalled Bearing, Test 1, Week 1, Multivariate Correlation,

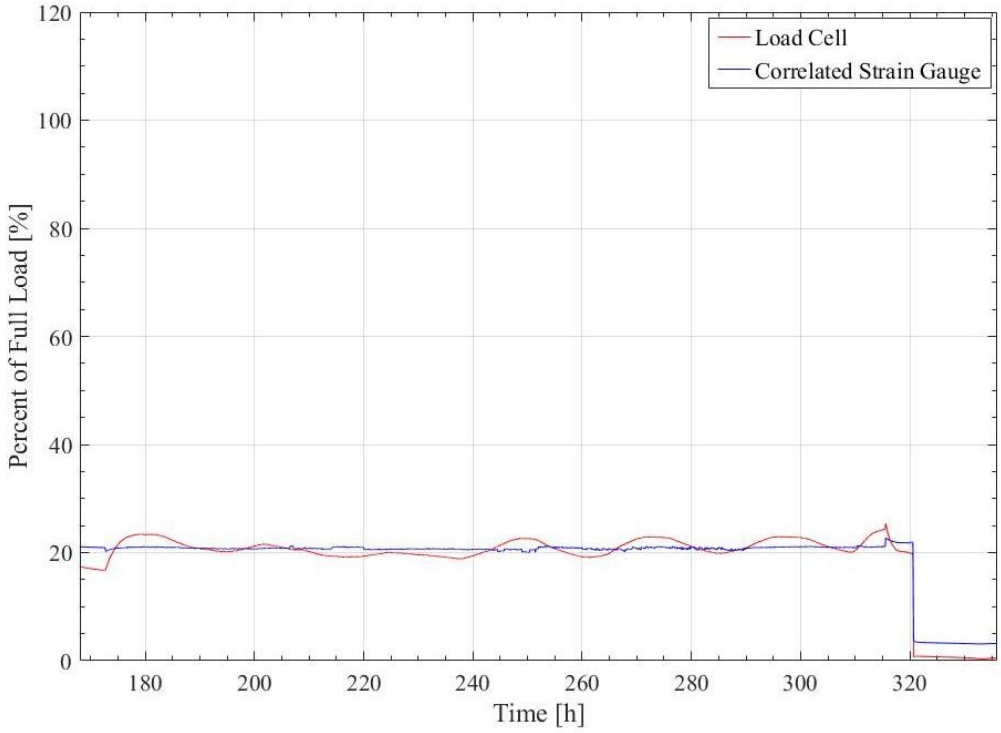

Figure 81. Spalled Bearing, Test 1, Week 2, 2nd Order Correlation

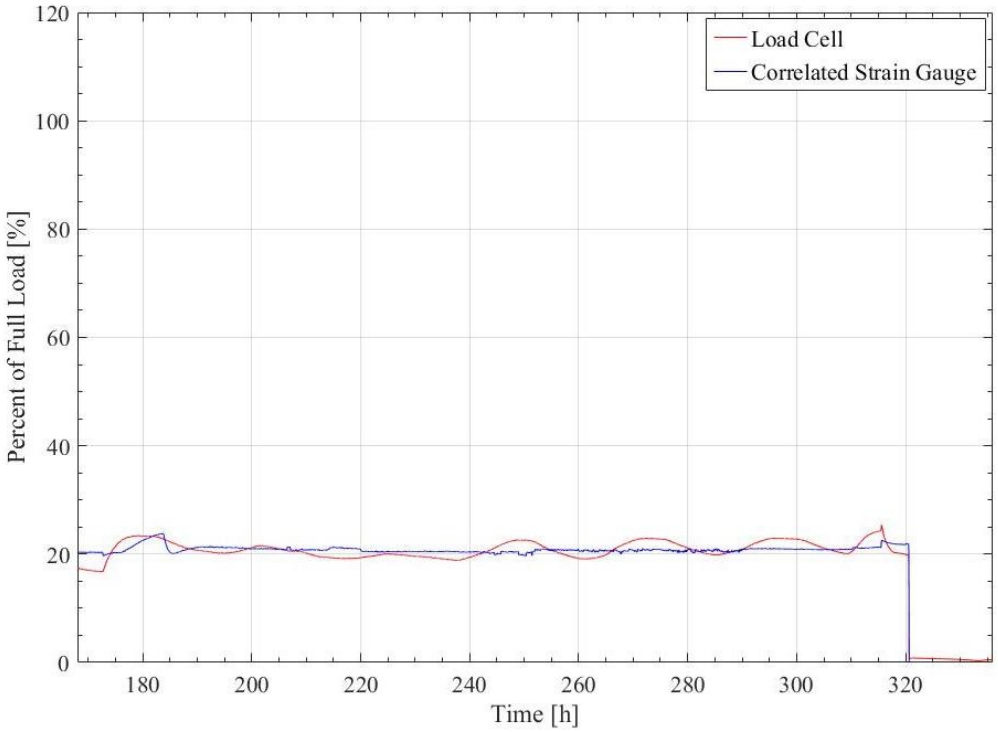

Figure 82. Spalled Bearing, Test 1, Week 2, Multivariate Correlation

Figure 81 shows the results of the second week of testing using the second-order correlation, which displayed an average error of 1.35%. Figure 82 shows the results of the second week of testing utilizing the multivariate correlation, which displayed an average error of 1.31%. It can be observed that both correlations display difficulty in accurately detecting the variations in load, which is primarily attributable to the vibration of the spall and the resulting effect on sensor output. Despite the testing conditions, temperature was able to contribute in some cases which the second-order correlation could not detect, such as the peak that occurs approximately at 180 hours into testing.

4.4.3 Spalled Bearing Test 2

The overview of the second test conducted utilizing a spalled bearing can be seen in Figure 83. This test focuses on loads above 90% of full-load. The first week of testing, utilizing a second-order correlation, can be observed in Figure 84. It can be seen that half of the first week was attributed to the continuation of the unloaded vibration testing seen previously, however, the second half concentrates on loaded situations. The second order correlation displayed an average error of 2.70% for the first week of testing, while the multivariate regression method, seen in Figure 85, displayed an average error of 5.49% which was due to the inability of the correlation to account for the unloaded portion at the beginning of testing. The error of the multivariate correlation decreases slightly when evaluating only loaded situations, where the loaded error of the second-order correlation decreases to 3.36%. Contrastingly, the loaded error of the second-order correlation increases to 3.67%. These averages, however, incorporate an outlier, as it seems that a fast reloading of the system at approximately 155 hours into testing affected the pressure distribution of the steering pad. In application, railcars are typically not loaded in under 20

seconds, therefore, the actual average errors for the testing period would decrease to 1.68% for the second-order method and 1.23% for the multivariate method.

Figure 86 shows the second week of testing utilizing the second-order correlation which displayed an average error of 3.27%. Figure 87 shows the second week of testing utilizing the multivariate correlation, which displayed an average error of 4.27%. However, when analyzing only the loaded portions of testing, the error of the second-order correlation increased to 3.55% and the error of the multivariate correlation increased to 4.63%.

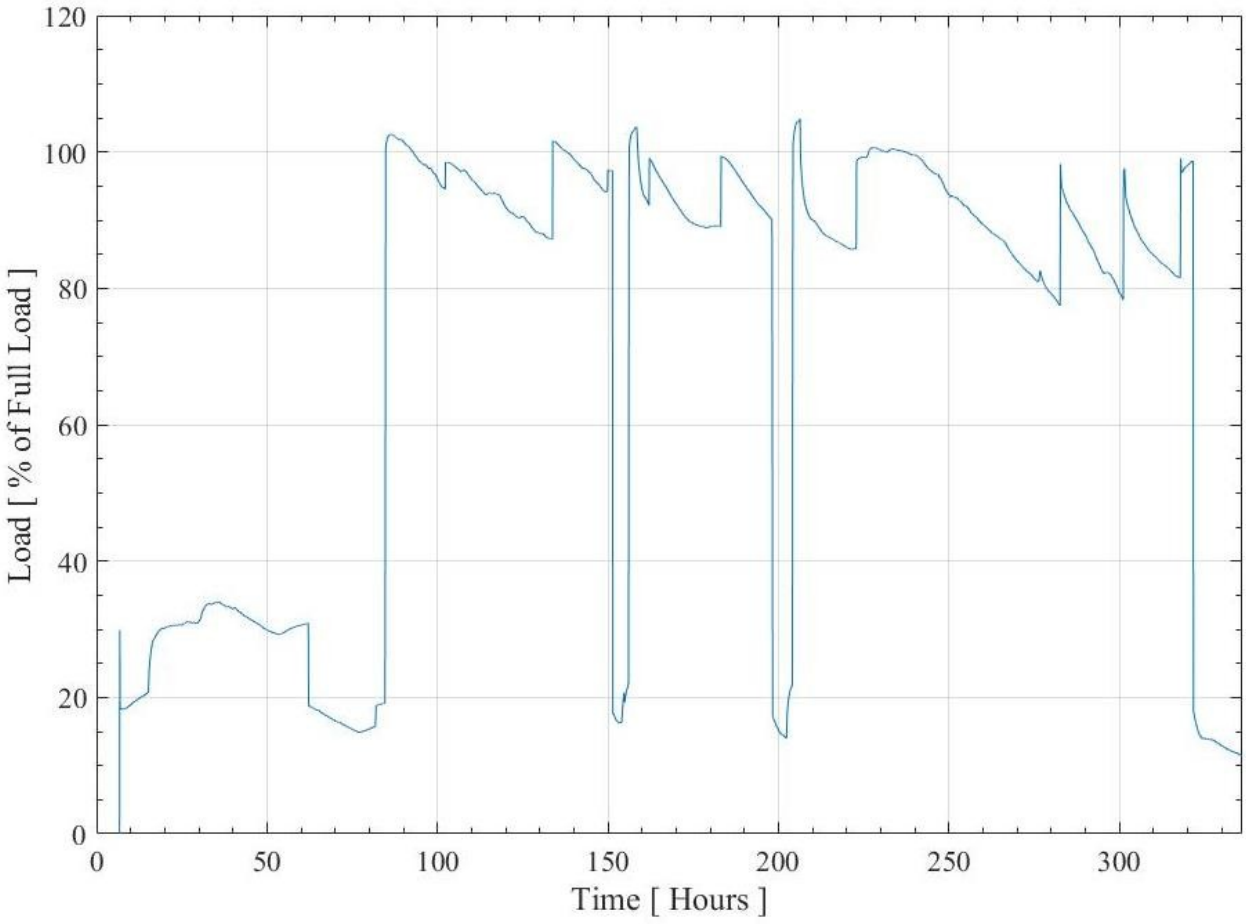

Figure 83. Reliability Testing on Spalled Bearing, Test 2

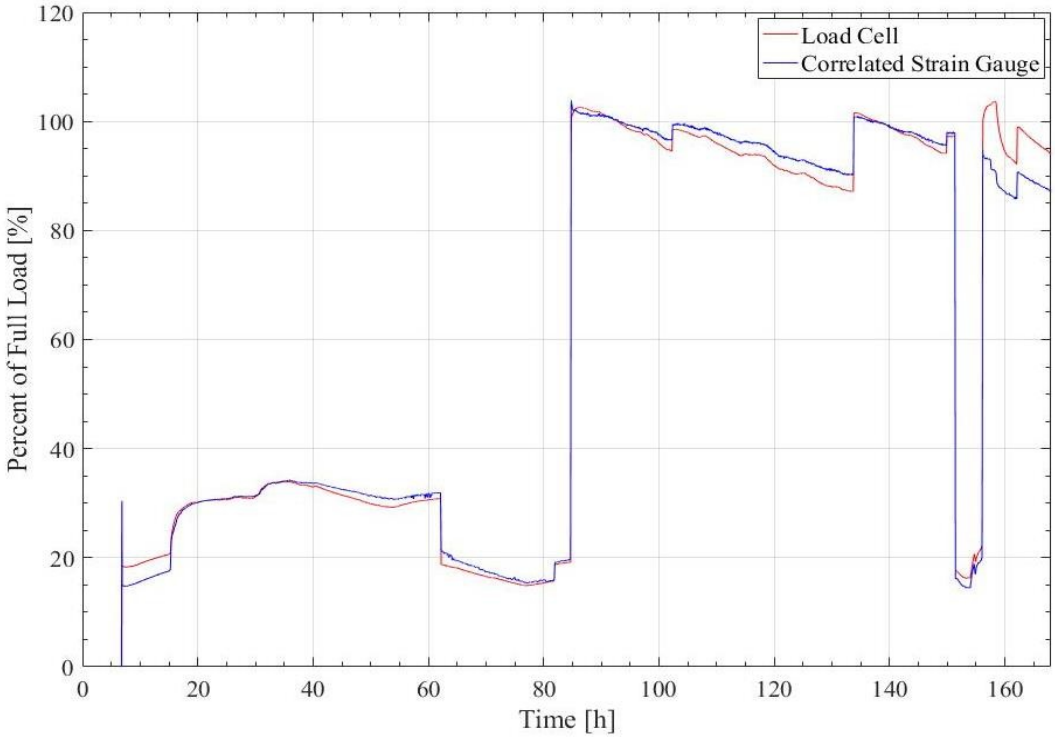

Figure 84. Spalled Bearing, Test 2, Week 1, 2nd Order Correlation

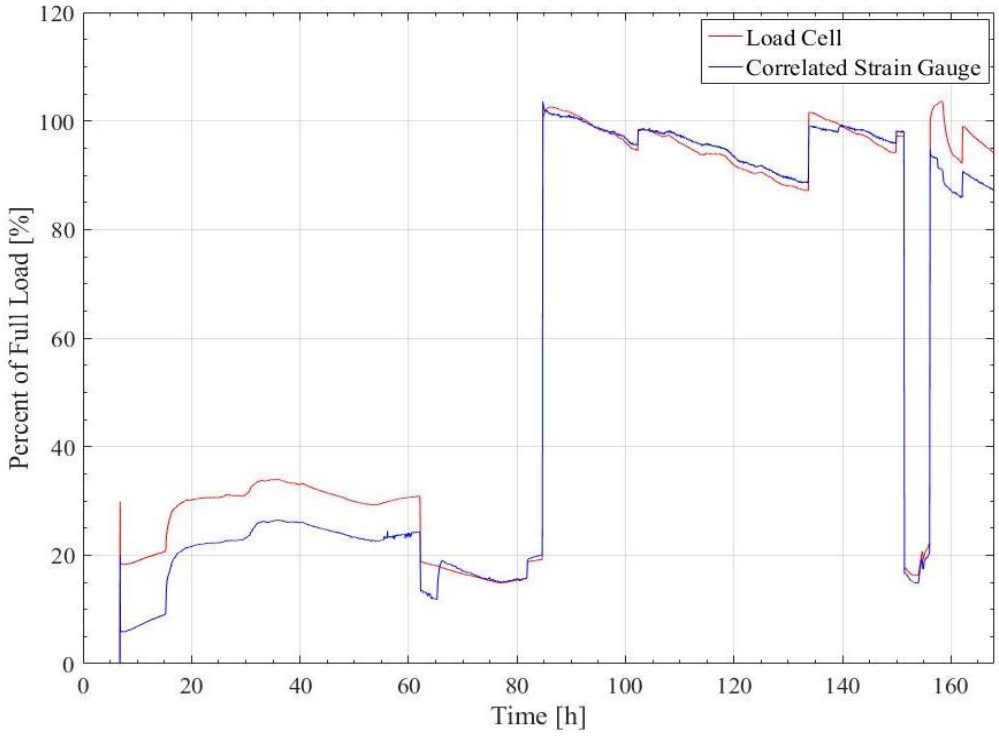

Figure 85. Spalled Bearing, Test 2, Week 1, Multivariate Correlation

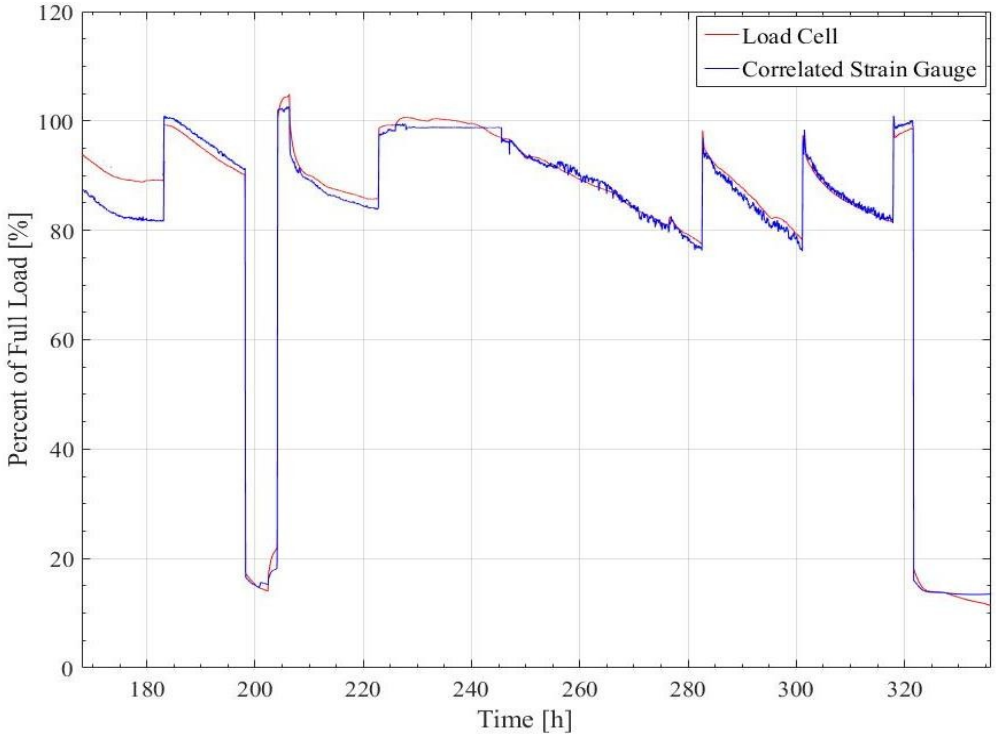

Figure 86. Spalled Bearing, Test 2, Week 2, 2nd Order Correlation

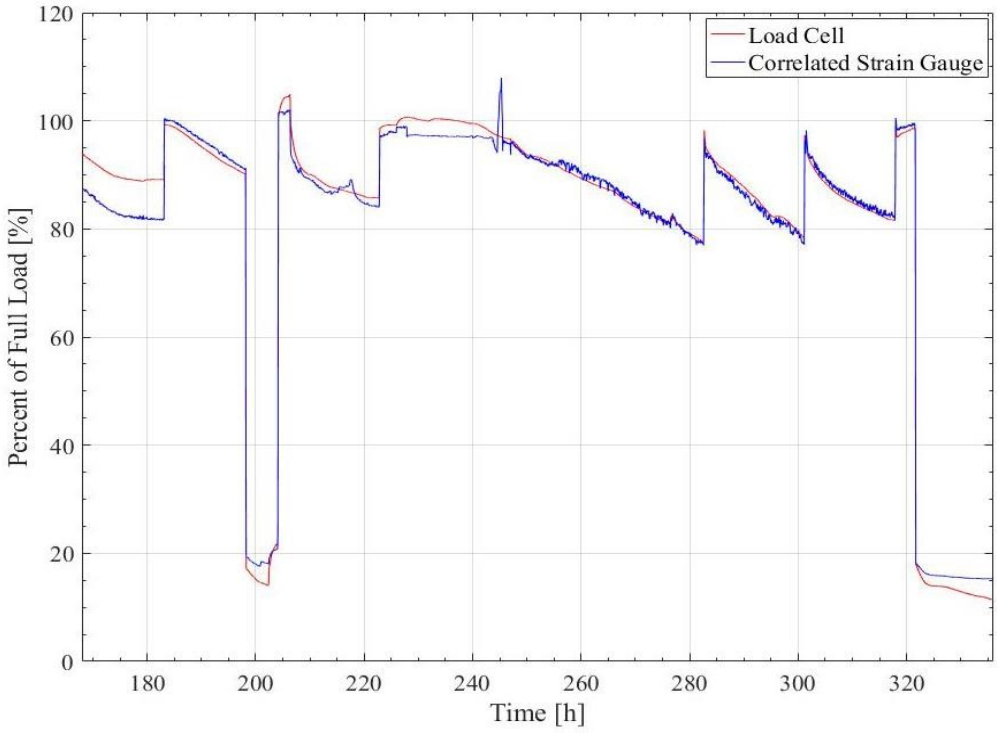

Figure 87. Spalled Bearing, Test 2, Week 2, Multivariate Correlation

4.4.4 Summary of Reliability Analysis Error

The summary of errors present in the reliability testing performed on Adapter B can be observed in Table 9. It can be seen that for the first test utilizing the spalled bearing, there are no loaded errors given which is due to the limited amount of data within the testing period above 90% of full-load. In two of the week testing periods, the second-order correlation outperforms the multivariate in the loaded case. This could be attributable to the amount of data points used to average the data and the instabilities that could arise from the multiple parameters involved in the post-processing of the multivariate correlation. It should also be noted that the welds and sensor went undamaged throughout this long and arduous testing period.

Table 9. Reliability Test Error Summary

Control Bearing			
	Week 1	Week2	Week 3
2nd Order (%)	0.96	0.91	2.94
Multivariate (%)	0.98	0.87	1.22
2nd Order Loaded (%)	2.79	2.34	5.55
Multivariate Loaded (%)	2.33	2.11	2.41
Spalled Bearing Test 1			
	Week 1	Week 2	
2nd Order (%)	1.74	1.35	
Multivariate (%)	1.65	1.31	
Spalled Bearing Test 2			
	Week 1	Week 2	
2nd Order (%)	2.70	3.27	
Multivariate (%)	5.49	4.27	
2nd Order Loaded (%)	3.67	3.55	
Multivariate Loaded (%)	3.36	4.63	

CHAPTER V

CONCLUSION AND FUTURE WORK

5.1 Conclusions

The results of the experimentation performed throughout this thesis demonstrate that the incorporation of raceway temperatures into the correlation of the load sensor can have an immensely positive influence over the accuracy of the sensor output. From the data presented in Chapter III, the load accuracy testing proved that the incorporation of raceway temperatures improved the sensor accuracy. The evaluation of the ability of the sensor to detect different loading scenarios progressed the development of the sensor to concentrate on the reliability and precision over long testing periods. Furthermore, an additional correlation will need to be implemented during the loading cycle. From the testing presented in Chapter IV, the Smart Adapter© load insert is able to produce a steady signal under numerous conditions including wheel impacts and spalled bearing vibration. The reliability analysis of the sensor demonstrated that mounting the sensor to the adapter by TIG welding improved the precision of the sensor and furthermore the welds were able to survive the severe loads and vibration inherent in spalled bearing operation

5.2 Future Work

The sensors need to undergo field testing to evaluate their accuracy and precision when employed in an actual railcar assembly. The sensor-adapter welded assemblies would be

mounted on a railcar to test the accuracy of the derived laboratory correlations. The field testing would optimally focus on the 100% loaded and 17% unloaded scenarios. This form of testing would provide data that is comparable to the laboratory and help demonstrate to the railroad industry that this is a viable product.

To increase the accuracy of the load sensor, it is recommended that five load and temperature scenarios be included in the calibration of each sensor. To achieve this, a rig would be designed which would contain the capability to simulate temperature and loading scenarios involved in operational bearing assemblies. While preliminary testing proved that the creation of a ramping correlation for the employed load sensors is possible, additional work and testing must be conducted to bring this aspect of the sensor to its fruition. Research should additionally be conducted which analyzes the adapter pad to evaluate the application and effect of reinforcing geometry or structures on the pressure distribution observed by the steering pad.

REFERENCES

[1] "Freight Rail Today," Federal Railroad Administration. [Online]. Available: www.fra.dot.gov/Page/P0362. [Accessed 6 June 2016].

[2] D. Heyman & R. Perez-Pena, "Spilled Oil Keeps Flames Burning After a Train Derailment in West Virginia," New York Times, 17 Feb. 2015. [Online]. Available: www.nytimes.com/2015/02/18/us/west-virginia-train-derailment-dumps-oil-into-river.html?_r=0. [Accessed 17 Nov. 2016].

[3] J. Ley, "Load Sensor in an Elastomer Suspension Element," Master's Thesis, University of Texas-Pan American, Edinburg, TX, United States, 2012.

[4] "Double Row Tapered Roller Bearings," SKF Bearings. [Online]. Available: www.skf.com/us/products/bearings-units-housings/roller-bearings/tapered-roller-bearings/double-row-tapered-roller-_bearings/index.html. [Accessed 26 July 2016].

[5] C. M. Tarawneh, "Experiments and Models for the Thermal Response of Railroad Tapered-Roller Bearings," *International Journal of Heat and Mass Transfer*, 51(25-26), p. 5794–5803, Dec. 2008.

[6] "Railway Investigation Report R11T0016," Transportation Safety Board of Canada, 2011. [Online]. Available: www.tsb.gc.ca/eng/rapportsreports/rail/2011/r11t0016/r11t0016.pdf. [Accessed 22 Aug. 2016].

[7] "A Short History of U.S. Freight Railroads," Association of American Railroads, May 2016. [Online]. Available: www.aar.org/BackgroundPapers/Railroad%20History%20May%202016.pdf. [Accessed 21 June 2016].

[8] "Overview of America's Freight Railroads," Association of American Railroads, June 2016. [Online]. Available: www.aar.org/BackgroundPapers/Overview%20of%20America's%20Freight%20RRs.pdf. [Accessed 5 July 2016].

[9] "The Need for Balanced Railroad Regulation," Association of American Railroads, May 2016. [Online]. Available: www.aar.org/BackgroundPapers/Need%20for%20Reasonable%20Railroad%20Regulation.pdf. [Accessed 2 Aug. 2016].

[10] "Map USA Railroad Routes," Ginu Blog. [Online]. Available: ginu.tk/2016/12/02/map-us-railroad-routes/. [Accessed 12 Sept. 2016].

[11] "America's Freight Railroads Under Balanced Regulation," Association of American Railroads. April 2016. [Online]. Available: www.aar.org/BackgroundPapers/Impact%20of%20the%20Staggers%20Act.pdf. [Accessed 3 July 2016].

[12] J. Z. Hecker, "Freight Railroads: Updated Information on Rates and Competition Issues." *U.S. Government Accountability Office,* Washington D.C., p. 6, 27 Sept. 2007.

[13] "Positive Train Control" Association of American Railroads. [Online]. Available: https://www.aar.org/policy/positive-train-control. [Accessed 15 July 2016].

[14] "Wayside Advanced Technology Systems (WATS)," Federal Railroad Administration. [Online]. Available: www.fra.dot.gov/Page/P0806. [Accessed: 12 Aug. 2016].

[15] S. Karunakaran, "Bearing Temperature Performance in Freight," *ASME RTD Fall Technical Conference*, Chicago, 2007.

[16] J. A. Kypuros, C. M. Tarawneh, A. Zagouris, S. Woods, B. M. Wilson & A. Martin, "Implementation of Wireless Temperature Sensors for Continuous Condition Monitoring of Railroad Bearings," *ASME RTD Fall Technical Conference*, Minneapolis, Minnesota, USA, 2011.

[17] N. G. Nenov, E. M. Dimitrov & G. S. Mihov, "Sensor for Measuring Load on Wheels of Running Railway Vehicle," *28th International Spring Seminar on Electronics Technology: Meeting the Challenges of Electronics Technology Progress*, 2005.

[18] "NEM Solutions - Hot Axle and Box Detection -HABD: System for Measuring the Temperature of Rolling Stock Gearboxes, Disc Brakes and Wheels," NEM Solutions. [Online]. Available: www.nemsolutions.com/rail/hot-axle-and-box-detection/. [Accessed 12 Aug. 2016].

[19] J. G. Tabbachi, R. R. Newman, R. C. Leedham, D. A. Purta, G. G. Madered, R. Galli, "Hot Bearing Detection with the SMART-BOLT," *Proceedings of the 1990 ASME/IEEE Joint Railroad Conference*, p. 105-10, 1990.

[20] "IONX Asset Monitoring," Amsted Rail. [Online]. Available: www.amstedrail.com/products-services/ionx-asset-monitoring. [Accessed 6 June 2016].

[21] V. J. Hodge, S. O'Keefe, S. Weeks, & A. Moulds, "Wireless Sensor Networks for Condition Monitoring in the Railway Industry: A Survey," *IEEE Transactions on Intelligent Transportation Systems,* 3(16), p. 1088-1106, June 2015.

[22] "Guardian Bearing (Sensor)," Timken. [Online]. Available: www.timkenbearings.com/pt-br/solutions/rail/products/Pages/GuardianBearing.aspx. [Accessed 14 June 2016].

[23] M. L. French, K. M. Iftekharrudin, D. R. Leeper, R. P. Samy, W. Hwang, "Bearing with Wireless Self-powered Sensor Unit." *The Timken Company*, assignee, Patent US 6535135 B1, 18 March, 2003.

[24] R. S. Toms, "Electronic Weighing System and Method for Railcars," *Union Tank Car Company*, assignee, Patent WO 2010093895 A1, 19 Aug. 2010.

[25] T. Diedrich, "Onboard Load Sensor Prototype for Use in Freight Railcar Service," Master's Thesis, University of Texas-Pan American, Edinburg, TX, United States, 2015.

[26] K. Malakhov, "Certain Problems of Weighing Technique in Railroad Transport – Documents," Documentslide.com, 17 Aug. 2016. [Online]. Available: docslide.us/documents/certain-problems-of-weighing-technique-in-railroad-transport.html. [Accessed 21 Aug. 2016].

[27] "Railcar Weighing Systems," Advanced Weigh Technologies, 2002. [Online]. Available: awtscale.com/attachments/22-SAI%20Railscale%20-%20General%20Brochure.pdf. [Accessed 5 June 2016].

[28] "Rail Scales," Kemeke. [Online]. Available: www.kemeke.com/en/top-menu/rail-scales/platform-railweighbridgeswhichismountedinthefoundationpit. [Accessed 12 Sept. 2016].

[29] "Truck Assemblies," *Amsted Rail*. [Online]. Available: www.amstedrail.com/products-services/truck-assemblies. [Accessed 12 Dec. 2016].

[30] "Brake Systems," Amsted Rail. [Online]. Available: www.amstedrail.com/brake-systems. [Accessed 31 Oct. 2016].

[31] C. Cruceanu, "Train Braking, Reliability and Safety in Railway," University Politehnica of Bucharest, Romania, 2012.

[32] "Adapter Plus Steering Pad System," Amsted Rail. [Online]. Available: www.amstedrail.com/products-services/adapter-plus-steering-pad-system. [Accessed 21 July 2016].

[33] L. Saenz IV, "Calibration and Optimization of a Load Sensor Embedded in a Railroad Bearing Adapter," Master's Thesis, University of Texas-Pan American, Edinburg, TX, United States, 2013.

[34] "Bearings," Amsted Rail. [Online]. Available: www.amstedrail.com/products-services/bearings. [Accessed 1 Nov. 2016].

[35] "Tapered Roller Bearing Units TAROL Products and Services," Schaeffler. [Online]. Available: www.schaeffler.com/remotemedien/media/_shared...2/.../tpi_158_de_en.pdf, [Accessed 12 Dec. 2016].

[36] "REC Rod End Load Cell," Interface Advanced Force Measurement. [Online]. Available: http://www.interfaceforce.com/index.php?REC-Rod-End-Load-Cell&mod=product&show=38. [Accessed 27 Oct. 2016].

[37] "Measuring Strain with a Strain Gauge," National Instruments. [Online]. Available: http://www.ni.com/white-paper/3642/en/. [Accessed 1 Dec. 2016].

[38] A. Gonzalez, "Development, Optimization, and Implementation of a Vibration Based Defect Detection Algorithm for Railroad Bearings," Master's Thesis, University of Texas-Pan American, Edinburg, TX, United States, 2015.

[39] W. N. Findley, J. S. Lai, & K. Onaran, "Creep and Relaxation of Nonlinear Viscoelastic Materials," *New York Dover Publications*, 1976.

[40] B. Tuzik, "Taking the Long View: 20 Years of Wheel/Rail Interaction (Part 2 of 2)," Interface: the Journal of Wheel/Rail Interaction, 22 April 2014. [Online]. Available: http://interfacejournal.com/archives/1008. [Accessed: 20 Nov. 2016].

[41] R. C. Juvinall & K. M. Marshek, "Fundamentals of Machine Component Design," *J. Wiley*, New York, 1991.

[42] D. L. Logan, "A First Course in the Finite Element Method," *CL Engineering*, 2007.

APPENDIX A

APPENDIX A
LOAD SENSOR SUMMARY

Load Accuracy Test Correlations

Adapter A					
2nd Order					
V0	V	V^2			
-23489	7157	344			
Multivariate					
V0	V	V^2	T	T^2	V*T
-54198	15229	-201	869	-6	-126

Adapter B					
2nd Order					
V0	V	V^2			
-11181	612	744			
Multivariate					
V0	V	V^2	T	T^2	V*T
-45871	7900	368	1103	-8	-144

Adapter C					
2nd Order					
V0	V	V0			
-23490	7157	344			
Multivariate					
V0	V	V^2	T	T^2	V*T
-53972	15165	-197	856	-6	-123

Load Accuracy Error Summary

Adapter A			
	2nd Order (%)	Multivariate (%)	Estimated Difference (lbs)
Total	1.62	0.61	-347
Total Loaded Dynamic	1.4	0.38	-351
Total Loaded Static	0.87	0.4307	-151
Dynamic	1.73	0.53	-413
Static	1.53	0.65	-303
Adapter B			
	2nd Order (%)	Multivariate (%)	Estimated Difference (lbs)
Total	1.63	0.46	-402
Total Loaded Dynamic	1.64	0.41	-423
Total Loaded Static	1.09	0.19	-310
Dynamic	1.86	0.54	-454
Static	1.46	0.37	-375
Adapter C			
	2nd Order (%)	Multivariate (%)	Estimated Difference (lbs)
Total	1.87	0.92	-327
Total Loaded Dynamic	1.38	0.82	-193
Total Loaded Static	1.52	0.39	-389
Dynamic	1.56	1.06	-172
Static	2.11	0.58	-526

Ramping Test Correlations

Adapter B (slow rates)			
3rd Order			
V^3	V^2	V	V0
290	-5009	38519	-91518

Adapter B			
3rd Order			
V^3	V^2	V	V0
100	-1971	23244	-71674

Adapter C			
3rd Order			
V^3	V^2	V	V0
474	-6285	38169	-60249

Adapter D			
3rd Order			
V^3	V^2	V	V0
-121	2455	-6447	-13772

Ramping Test Error Summary

Adapter B (slow rates)	
Rate	Error [%]
3 min	1.15
5 min	1.57
7 min	0.31
10 min	0.13
12 min	0.40
15 min	-0.06

Adapter B	
Rate	Error [%]
18 s	1.66
35 s	1.37
1 min	-0.97
1 min 30 s	-0.89
2 min	-0.48
2 min 30 s	0.13
3 min	1.99
3 min 30 s	1.59
4 min	1.63
5min	-1.54

Adapter C	
Rate	Error [%]
18 s	-3.07
35 s	-1.05
1 min	-1.18
1 min 30 s	0.49
2 min	0.47
2 min 30 s	0.11
3 min	0.50
3 min 30 s	0.41
4 min	-0.20
5min	0.51

Adapter D	
Rate	Error [%]
18 s	-0.96
35 s	1.37
1 min	-1.69
1 min 30 s	-0.24
2 min	-0.25
2 min 30 s	-0.18
3 min	-0.56
3 min 30 s	-0.37
4 min	-1.20
5min	1.41

Adapter B Reliability Control Testing Correlation

2nd Order

V0	V	V^2
-16154	1172	581

Multivariate

V0	V	V^2	T	T^2	V*T
-48725	7580	400	980	-4	153

Adapter B Reliability Spalled Testing Correlation

2nd Order

V0	V	V^2
-15180	1014	698

Multivariate

V0	V	V^2	T	T^2	V*T
-46512	6430	395	1145	-7	147

Reliability Test Error Summary

Control Bearing			
	Week 1	Week2	Week 3
2nd Order (%)	0.96	0.91	2.94
Multivariate (%)	0.98	0.87	1.22
2nd Order Loaded (%)	2.79	2.34	5.55
Multivariate Loaded (%)	2.33	2.11	2.41
Spalled Bearing Test 1			
	Week 1	Week 2	
2nd Order (%)	1.74	1.35	
Multivariate (%)	1.65	1.31	
Spalled Bearing Test 2			
	Week 1	Week 2	
2nd Order (%)	2.70	3.27	
Multivariate (%)	5.49	4.27	
2nd Order Loaded (%)	3.67	3.55	
Multivariate Loaded (%)	3.36	4.63	

APPENDIX B

APPENDIX B

THERMOPLASTIC POLYURETHANE STEERING PAD PROPERTIES

Elastollan® TPU Technical Data Sheet

BASF
The Chemical Company

Elastollan® 1154D

Polyether-based Grade

Elastollan® 1154D exhibits excellent abrasion resistance, toughness, transparency, very good low temperature flexibility, hydrolytic stability and fungus resistance. It has excellent damping characteristics and outstanding resistance to tear propagation. Elastollan® 1154D conforms to the FDA food contact regulations as described in book 21, section 177.2600 for wet food contact applications. Elastollan® 1154D also has NSF Standard 61 "Water Contact Material" certification. Elastollan® 1154D is supplied uncolored in diced form.

Typical Properties of Elastollan®	ASTM Test Method	Units	Typical Values
All the physical properties reported here are measured on injection molded samples (about 2.2 mm thickness). Properties of sheet or film samples of this product are also available upon request.			
Specific Gravity	ASTM D 792	g/cm^3	1.16
Shore Hardness	ASTM D 2240	Shore A or D	54D
Taber Abrasion	ASTM D 1044	mg loss	60
DIN Abrasion	DIN 53516	mm^3 loss	30
E-Modulus	ASTM D 412	psi	22000
Flexural Modulus	ASTM D 790	psi	24000
Tensile Strength	ASTM D 412	psi	7000
Tensile Stress at 100% Elongation	ASTM D 412	psi	3800
Tensile Stress at 300% Elongation	ASTM D 412	psi	6600
Ultimate Elongation	ASTM D 412	%	410
Tear Strength	ASTM D 624, Die C	lb/in	1200
Compression Set **22h at 70°C** **22h at 23 °C**	ASTM D 395 "B"	% of original deflection	 50 40
Glass Transition temperature*	BASF Analytical Method	°C	-16
Vicat Softening Temperature	ASTM D 1525	°C	138
DMA Softening Temperature	BASF Analytical Method	°C	127

*Measured with Dynamic Mechanical Analysis (DMA). DMA profile is available upon request.
Above values are shown as typical values and should not be used as specifications.

Elastollan® TPU
Technical Data Sheet

BASF
The Chemical Company

Elastollan® 1154D
Polyether-based Grade

DRYING: Elastollan® materials are hydroscopic, i.e. dry Elastollan® will rapidly absorb moisture when exposed to atmosphere. Polyether-based Elastollan® grades absorb moisture more rapidly than polyester-based Elastollan® grades. As with all TPU products, Elastollan® 1154D must be dried before processing. The drying step is required to maintain a low moisture content until the product enters the processing equipment. The water content must be less than 0.03% before and during processing.

Drying diagram for Elastollan

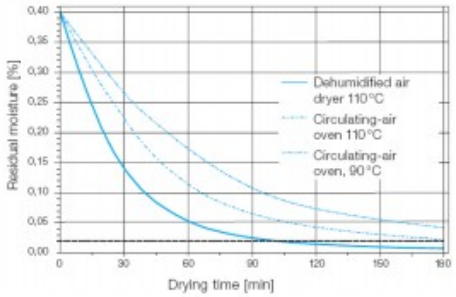

Elastollan® Hardness	Drying Time	Drying Temperature	
		Circulating air	Dehumidified Air
78A to 90A	2 to 3 h	100 to 110 °C	80 to 90 °C
> 90A	2 to 3 h	110 to 120 °C	90 to 120 °C

STORAGE: Elastollan® 1154D can be stored for up to one year in its original container. Containers should be stored in a cool and dry area. Containers should be tightly closed after use. Granulates should be exposed to the surrounding air only for as long as absolutely essential; it is therefore important to cover the feed hopper of the processing machine. Drying is recommended if the container has been opened several times. In order to prevent condensation, materials stored in cool conditions should be brought to room temperature before opening the container.

Moisture absorption
Polyether-TPU
Hardness 80 Shore A – 64 Shore D

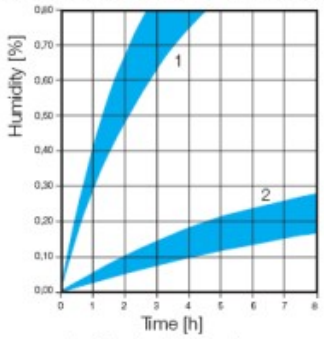

1 – Standard atmosphere 40 °C/92% rel. hum.
2 – Standard atmosphere 23 °C/50% rel. hum.

PROCESSING RECOMENDATIONS: Single screw extruder with a compression ratio of 1:2 to 1:3, preferably 1: 2.5, are recommended for processing Elastollan®. BASF experience shows that three section screws with an L/D ratio of 25 to 30 are most suitable. Three section screws should have continued constant pitch of 1D. The radial clearance between screw and barrel should be 0.1 to 0.2 mm. For processing Elastollan®, multizone screws, e.g. barrier screws, have also proven suitable. Short screws with high compression ratio are unsuitable for Elastollan®. Use of breaker plates and screen packs is recommended. Depending on the screw diameter and type of die, breaker plates should have holes of 1.5 to 5 mm in diameter. Since thermoplastic polyurethanes are shear sensitive, excessively high screw speeds may lead to reduction in product properties.

Screw configuration (diagrammatic view)

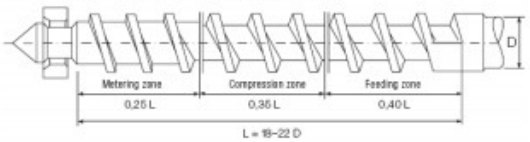

Elastollan® TPU Technical Data Sheet

BASF
The Chemical Company

TYPICAL PROCESSING CONDITIONS: Elastollan® 1154D is preferably used for injection molding applications and can be used for extrusion conditions. Typical processing conditions are listed in the table below. We recommend you to call our technical service helpdesk for more information or troubleshooting.

INJECTION MOLDING		
Recommended barrel temperatures in °C		
Elastollan® Hardness	Barrel Temperature	Nozzle
60A- 80A	170-210	200-210
85A- 95A	190-220	210-225
98A-74D	210-230	220-240

VISCOSITY CURVE:

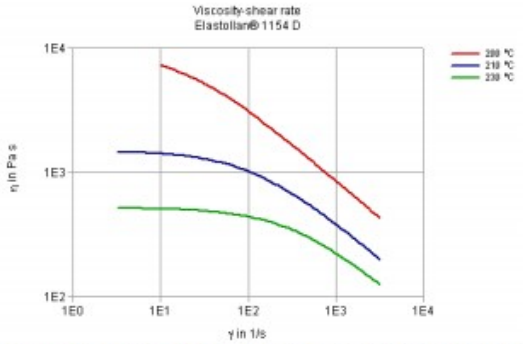

SHRINKAGE: This graph can be used for estimated shrinkage values of Elastollan® products in relation to the wall thickness. Please remember that depending on the molding conditions and part design these values can change. We recommend you to call technical service group for further information.

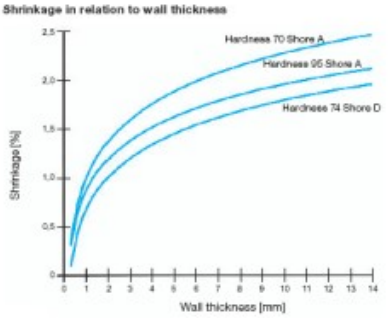

CHALLENGE US: Please contact us for more information on Elastollan® products.

You can reach our technical team at 1-800-892-3111 or tpu_helpdesk@basf.com. You can find more information at www.basf.com/elastollan. Our mailing address is BASF Corporation, 1609 Biddle Avenue, Wyandotte, Michigan 48192

For Further information, the following detailed brochures are available upon request:

- Elastollan® Material Properties
- Elastollan® Product Range
- Elastollan® Processing Recommendations
- Elastollan® Electrical Properties
- Elastollan® Chemical Resistance

DISPOSAL: Elastollan® materials are fully reacted and present no hazard to the environment. Waste can therefore be disposed at public waste disposal sites. The official regulations on waste disposal should be observed. For further information, please see BASF material safety data sheets.

CAUTION: Contact with product dusts from regrinding operations may cause temporary irritation of the eyes and the respiratory tract. Use with local exhaust. Under hot melt processing conditions (170-230°C), wear personal protective equipment to prevent thermal burns.

FIRST AID: Eyes-Flush eyes with flowing water at least 15 minutes. If irritation develops, consult a physician. *Skin*-Skin contact with hot melt may cause thermal burns. Call a physician immediately. *Inhalation*-If vapors generated from the hot melt process are inhaled, move to fresh air. Aid in breathing. If breathing difficulties develop, see a physician immediately.
In case of fire: Use water fog, foam, CO_2, or dry chemical extinguishing media. Firefighters should be equipped with self-contained breathing apparatus and turnout gear.

APPENDIX C

APPENDIX C

PROPERTIES OF A2 TOOL STEEL

Technical Datasheet

CARPENTER

A2 Tool Steel

Identification

UNS Number

- T30102

AISI Number

- Type A2

Type Analysis

Carbon	1.00 %	**Manganese**	0.80 %
Silicon	0.30 %	**Chromium**	5.25 %
Molybdenum	1.10 %	**Vanadium**	0.21 %
Iron	91.35 %		

General Information

Description

A2 tool steel is an air hardening tool steel capable of being hardened throughout, even in heavy sections. This tool steel has been used for applications in which the sections are very large or involve extreme accuracy of size and extreme hazards in hardening. A2 tool steel displays good balance between hardness and toughness. It is available as a DeCarb-Free product. DCF bars have been cold finished in the mill, thereby eliminating the need for bar bark removal.

Applications

A2 tool steel has been used in applications which require extreme accuracy and safety in hardening and when the sections are heavy. Typical applications have included:

Large blanking dies
Thread roller dies
Long punches
Rolls
Master hubs
Trimming dies
Forming dies
Precision tools
Gauges
Coining dies

Properties

Physical Properties

Specific Gravity	7.87	
Density	0.2840	lb/in³

Mean CTE

68 to 212°F	5.94	x 10⁻⁶ in/in/°F
68 to 392°F	6.67	x 10⁻⁶ in/in/°F
68 to 572°F	7.06	x 10⁻⁶ in/in/°F
68 to 752°F	7.33	x 10⁻⁶ in/in/°F
68 to 932°F	7.61	x 10⁻⁶ in/in/°F
68 to 1112°F	7.78	x 10⁻⁶ in/in/°F
68 to 1292°F	7.94	x 10⁻⁶ in/in/°F
68 to 1382°F	8.00	x 10⁻⁶ in/in/°F

A2 Tool Steel

Mean Coefficient of Thermal Expansion—A2 Tool Steel
The following figures are the average coefficients between room temperature and the specified elevated temperature. They represent material in the annealed condition and the dimensions are in in/in/° temperature.

Room Temperature		Average Coefficient	
68°F to	20°C to	10^{-6}/°F	10^{-6}/°C
212	100	5.96	10.7
392	200	6.64	12.0
572	300	7.05	12.7
752	400	7.36	13.2
932	500	7.60	13.7
1112	600	7.75	14.0
1292	700	7.92	14.3
1382	750	7.98	14.4

Modulus of Elasticity (E) 29.5 x 10^3 ksi

Isothermal Transformation Diagram—A2 Tool Steel
Austenitizing Temperature - 1750° F (954° C)

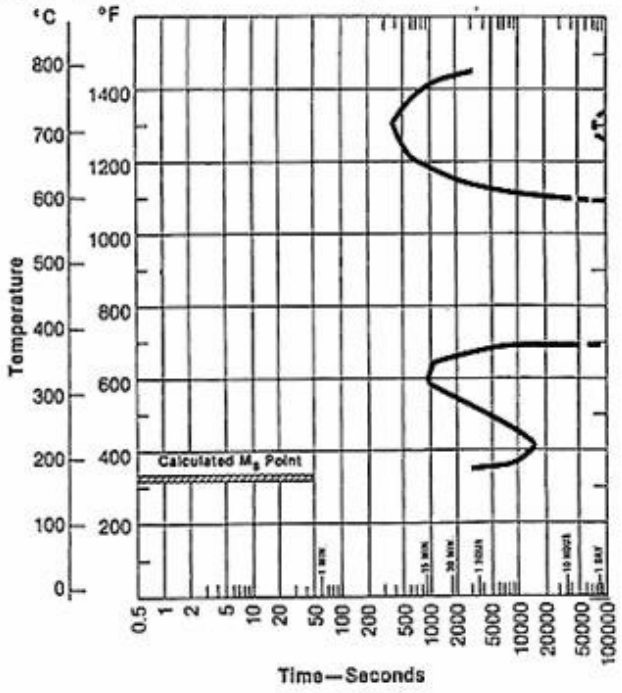

A2 Tool Steel

Typical Mechanical Properties

Reduction in Area and Elongation–A2 Tool Steel

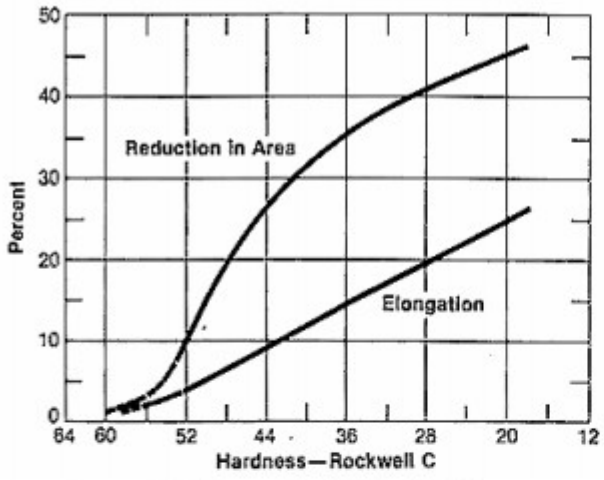

Tensile and Yield Strengths–A2 Tool Steel

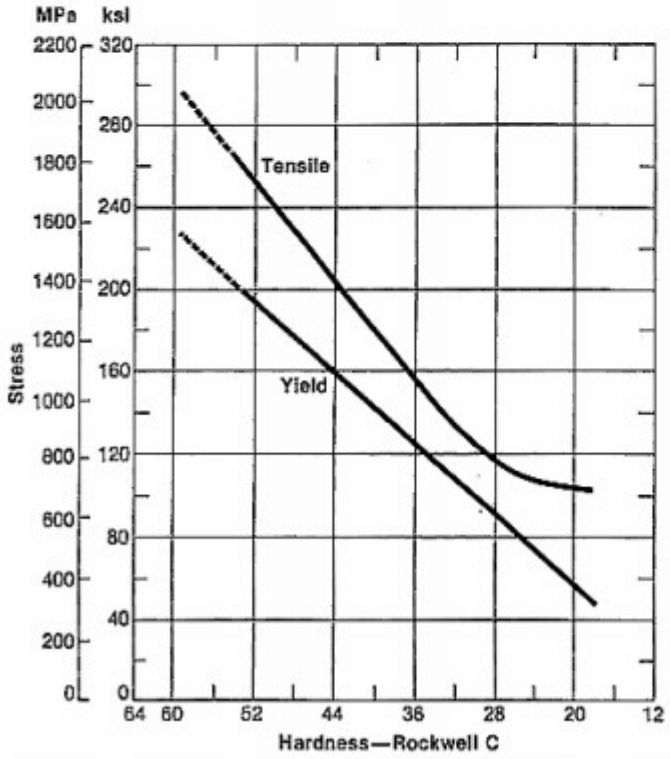

Typical Unnotched Izod Impact Strength–A2 Tool Steel

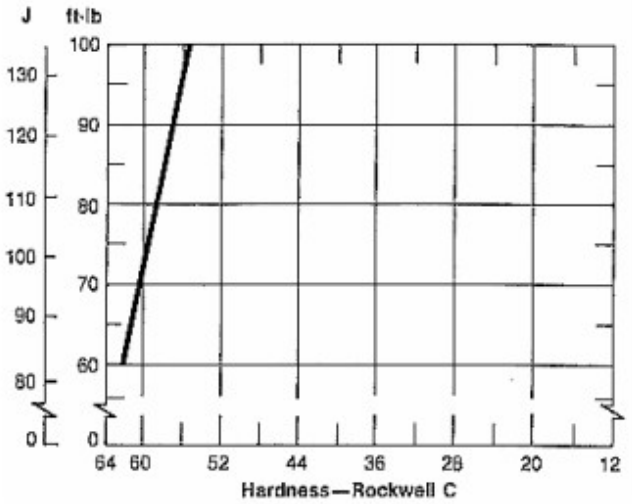

Heat Treatment

Decarburization

Like all high carbon tool steels, A2 tool steel is subject to decarburization during thermal processing and precautions must be taken to control this condition. Modern furnaces are available which provide environments designed to minimize decarburization.

Normalizing

Normalizing A2 tool steel is not recommended and is not necessary after furnace cooling as described above.

Annealing

For annealing, this tool steel should be either packed in a suitable container, using a neutral packing compound, or placed in a controlled atmosphere furnace. Heat uniformly to 1550/1600°F (843/871°C) and cool very slowly in the furnace at a rate of not more than 20°F (11°C) per hour until the furnace is black. The furnace may then be turned off and allowed to cool naturally. This will produce a maximum hardness of Brinell 228.

Hardening

Tools made from A2 tool steel may be hardened by placing them in a furnace maintained at a temperature of 1725/1775°F (940/969°C). Let the tools heat naturally to the furnace temperature, soak for 20 minutes plus 5 minutes per inch of thickness and air quench. Control of decarburization can be accomplished by using any one of the several modern heat-treating furnaces designed for this purpose. If endothermic atmospheres are used, a dew point between +40/50°F (+4/10°C) is suggested. In older type manually operated exothermic atmosphere furnaces, an oxidizing atmosphere is required. Excess oxygen of about 4 to 6% is preferred. If no atmosphere is available, the tool should be pack hardened or wrapped in stainless steel foil to protect its surface.

Deformation (Size Change) in Hardening

Remember that tool steels hold size best when quenched from the proper hardening temperature. If overheated they tend to show shrinkage after tempering. A2 tool steel is particularly sensitive to this problem and therefore should never be hardened from a temperature above 1775°F (968°C). The temperatures used to develop this data are shown within the hyperlink entitled "Size Change." Tool steel can be expected to expand when tempered below 600°F (316°C) but to shrink when tempered between 600 and 975°F (316 and 924°C). The following size change graph within the hyperlink below illustrates typical length changes of A2 tool steel after having been properly hardened and tempered. Note that the length change information is presented in inches per inch of original length.

Size Change in Hardening–A2 Tool Steel

1" (25.4 mm) diameter, air quenched from 1750° F (954° C), tempered 1 hour at temperature.

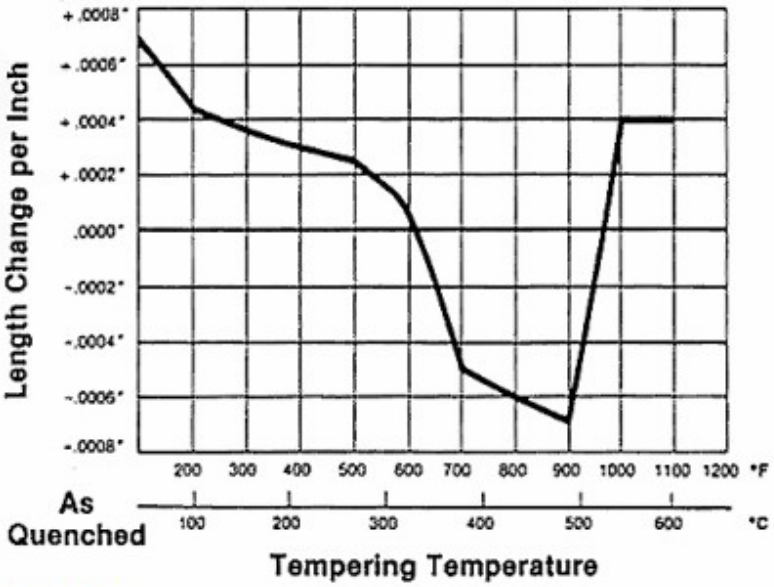

Stress Relieving

To relieve machining stresses for greater accuracy in hardening, first rough machine, then heat to a temperature of 1200/1250°F (649/677°C) for a minimum of one hour at temperature and cool slowly. After cooling, parts may be finish machined.

Tempering

The best combination of hardness and toughness is obtained by tempering A2 tool steel at 400°F (204°C). For greater ductility with some sacrifice in hardness, temper at 700°F (371°C). The following table within the hyperlink entitled "Effect of Tempering Temperature on Hardness" shows the effect of tempering.

Effect of Tempering Temperature–A2 Tool Steel
Air quenched from 1775° F (969° C) and tempered 1 hour at heat.

Tempering Temperature		Rockwell C Hardness
°F	°C	
As Hardened		63/64
300	149	63/64
350	177	61/63
400	204	60/62
450	232	59/61
500	260	58/60
600	316	57/59
700	371	57/59
800	427	57/59
900	482	57/59
1000	538	56/58
1100	593	50/51
1200	649	44/45

A2 Tool Steel

Workability

Forging

A2 tool steel forges very much like a high-speed steel. Heat uniformly and forge from a temperature between 1950 and 2050°F (1066 and 1121°C). Do not continue forging below 1700°F (927°C); reheat as often as necessary. Small, simple forgings can be cooled slowly in lime. The best practice for large forgings is to place them in a furnace heated to about 1550°F (843°C), soak uniformly at this heat, then shut off the heat and cool the job slowly in the furnace. This is not an anneal; after the forging is cold, it must be annealed as described in the "annealing" section that follows.

Machinability

The machinability of A2 tool steel may be rated between 60/65% of Type W-1 tool steel or about 40 to 50 % of B1112.

Following are typical feeds and speeds for A2 tool steel.

Turning—Single-Point and Box Tools

Depth of Cut, In.	High-Speed Tools			Carbide			
	Speed, fpm	Feed, ipr	Tool Material	Speed, fpm		Feed, ipr	Tool Material
				Brazed	Throw Away		
.150	75	.015	M-2	270	315	.015	C-6
.025	85	.007	M-3	315	380	.007	C-7

Turning—Cut-Off and Form Tools

Speed, fpm	Feed, ipr							Tool Material
	Cut-Off Tool Width, Inches			Form Tool Width, Inches				
	1/16	1/8	1/4	1/2	1	1-1/2	2	
60	.001	.0015	.002	.0015	.001	.001	.0007	M-2
205	.003	.0045	.006	.003	.0025	.0025	.0015	C-6

Drilling

Speed, fpm	Feed, ipr								Tool Material
	Nominal Hole Diameter, Inches								
	1/16	1/8	1/4	1/2	3/4	1	1-1/2	2	
45	.001	.001	.003	.005	.007	.008	.010	.012	M-1;M-10

Reaming

Speed, fpm	High-Speed Tool							Carbide Tool	
	Feed, Inches per Rev						Tool Material	Speed, fpm	Tool Material
	Reamer Diameter, Inches								
	1/8	1/4	1/2	1	1-1/2	2			
45	.003	.005	.008	.011	.015	.018	M-7	150	C-2

A2 Tool Steel

Tapping

Speed, fpm	Tool Material
25	M-1; M-7; M-10

Die Threading

Speed, fpm				Tool Material
7 or Less	8 to 15	16 to 24	25 and up, T.P.I.	
8-12	12-18	18-25	20-30	M-1;M-2;M-7;M-10

Milling—End Peripheral

Depth of Cut, In.	High-Speed Tools						Carbide Tools					
	Speed, fpm	Feed—Inches per tooth				Tool Material	Speed, fpm	Feed—Inches per tooth				Tool Material
		Cutter Diameter, Inches						Cutter Diameter, Inches				
		1/4	1/2	3/4	1-2			1/4	1/2	3/4	1-2	
.050	75	.001	.002	.003	.004	M-2;M-7	300	.0015	.0025	.004	.005	C-6

Broaching

Speed, fpm	Chip Load, Inches per tooth	Tool Material
15	.003	M-42

Sawing—Power Hack Saw

Pitch—Teeth per Inch				Speed	Feed
Material Thickness, Inches					
Under 1/4	1/4-3/4	3/4-2	Over 2	Strokes/Minute	Inches/Stroke
10	6	6	4	140	.006
10	6	6	4	70	.003
10	10	6	4	85	.003
10	10	6	4	55	.005
10	8	6	4	75	.003

Figures used for all metal removal operations covered are average. On certain work, the nature of the part may require adjustment of speeds and feeds. Each job has to be developed for best production results with optimum tool life. Speeds or feeds should be increased or decreased in small steps.

Additional Machinability Notes

Figures used for all metal removal operations covered are average. On certain work, the nature of the part may require adjustment of speeds and feeds. Each job has to be developed for best production results with optimum tool life. Speeds or feed should be increased or decreased in small steps.

Other Information

Wear Resistance

The wear characteristics of A2 tool steel shown within the hyperlink entitled "Dry Sand/Rubber Wheel Abrasion Test" were generated using ASTM-G65 Procedure A titled "Standard Practice for Conducting Dry Sand/Rubber Wheel Abrasion Tests". The data are presented as a volume loss as required by the ASTM Standard. Note, therefore, that a lower number indicates better wear resistance.

A2 Tool Steel

DrySand/Rubber Wheel Abrasion Test–A2 Tool Steel
All specimens air hardened from 1777° F (969° C) and tempered for 1 hour.

Tempering Temperature		Rockwell C Hardness	Average Volume Loss ASTM
°F	°C		
As Hardened		64/65	57.7
400	204	60.5	61.2
450	232	60	62.6
1025	552	56.5	75.7
1100	593	51/52	83.4
1200	649	45/46	107.7

Applicable Specifications

- ASTM A681
- QQ-T-570

Forms Manufactured

- Bar-Rounds

Technical Articles

- A Three-Point Program for Improving the Performance of Cold Work Tooling
- New Powder Metal Die Steel for Cold Work Tooling Applications
- The ABC's of Alloy Selection, Heat Treating and Maintaining Cold Work Tooling

Edition Date: 07/01/2000

APPENDIX D

APPENDIX D

CAD SENSOR DRAWINGS

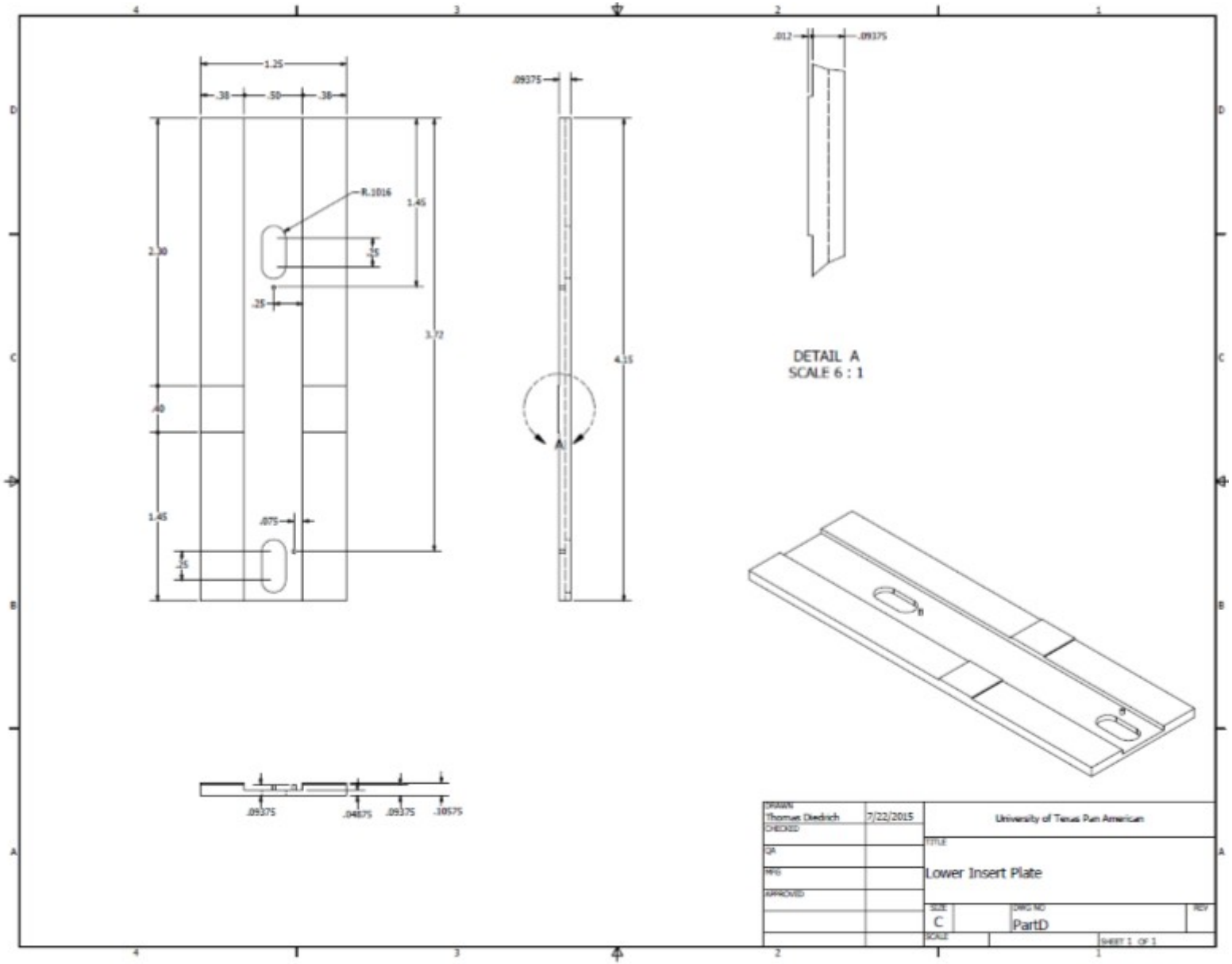
1.25
.38
.50
.38
R.1016
1.45
2.30
.75
.25
3.72
.40
1.45
.075
.25
.09375
4.15
.012
.09375
DETAIL A
SCALE 6 : 1
.09375
.04875
.09375
.10575
Thomas Diedrich
7/22/2015
University of Texas Pan American
Lower Insert Plate
C
PartD
SHEET 1 OF 1

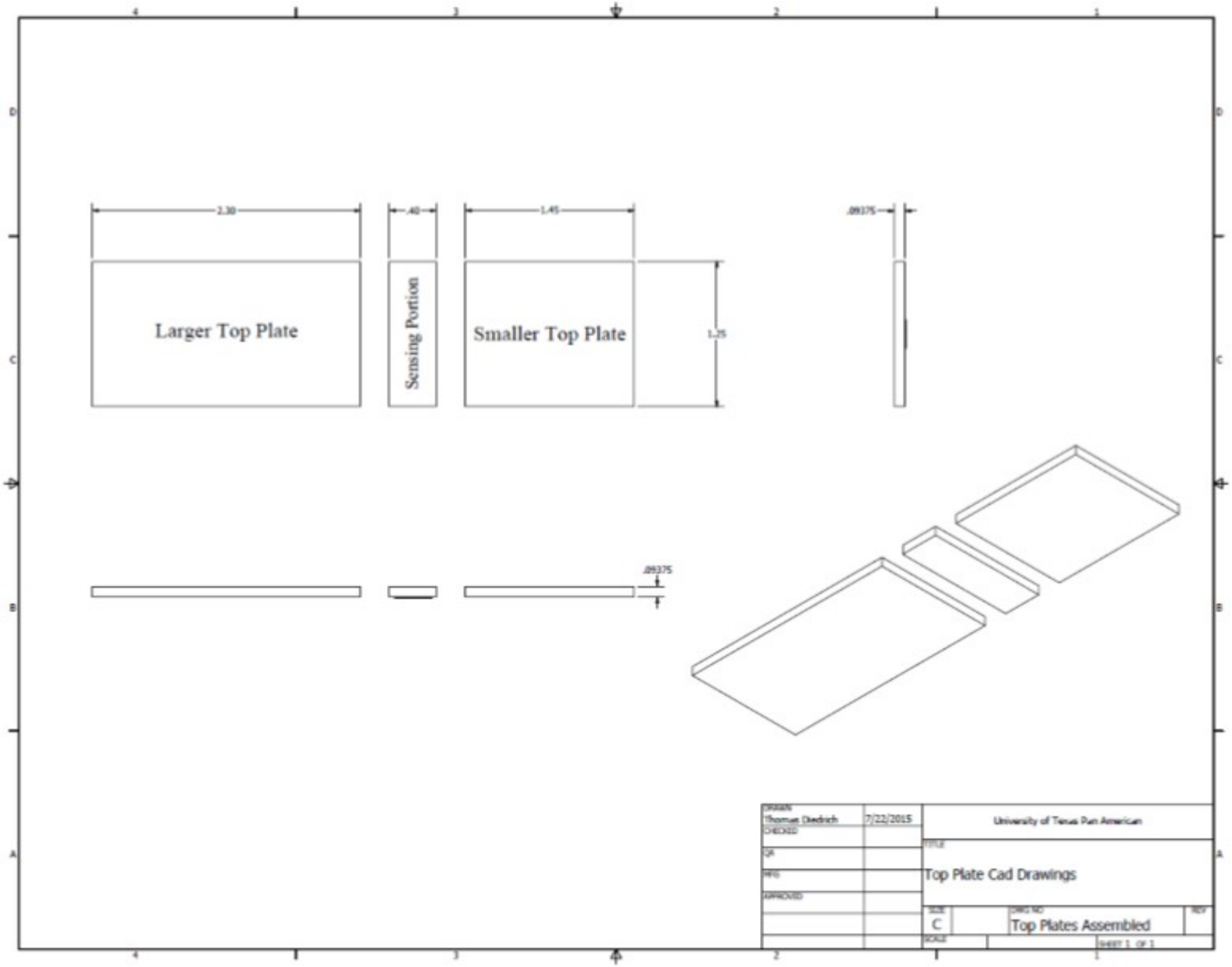
2.30
.40
1.45
.09375
Larger Top Plate
Sensing Portion
Smaller Top Plate
1.75
.09375
Thomas Diedrich
7/22/2015
University of Texas Pan American
Top Plate Cad Drawings
C
Top Plates Assembled

APPENDIX E

APPENDIX E

STRAIN GAUGE DATA SHEET

Full Bridge Patterns

Micro-Measurements

VISHAY PRECISION GROUP

Transducer-Class® Strain Gages

GAGE PATTERN Actual size shown. Enlarged when necessary for definition. DIMENSIONS (inch / millimeter)	GAGE DESIGNATION See Note 1	RES. IN OHMS	STANDARD CREEP CODE	ENCAPSULATION OPTION AVAILABLE
	Low-cost full-bridge gage for bending-beam transducers. †BAL is balanced to ± 0.4mV/V, but RG is 350 ohms ± 15%			
GAGE LENGTH: 0.050 / 1.28 OVERALL LENGTH: 0.260 / 6.66 GRID WIDTH: 0.050 / 1.28 OVERALL WIDTH: 0.220 / 5.64 MATRIX SIZE: 0.32 L x 0.25 W / 8.2 L x 6.4 W	J2A-XX-S1425-35B	BAL ± 0.4†	N/A	
	Compact full-bridge pattern for use on small, double-bending beams. Axial grid centerline spacing 0.250 in (6.35 mm).			
GAGE LENGTH: 0.125 / 3.18 OVERALL LENGTH: 0.465 / 11.81 GRID WIDTH: 0.060 / 1.52 OVERALL WIDTH: 0.189 / 4.80 MATRIX SIZE: 0.54 L x 0.26 W / 13.7 L x 6.6 W	N2A-XX-S055R-350	350 ± 0.2%	R	E2
	Similar to S055R pattern except axial grid centerline spacing 0.330 in (8.38mm).			
GAGE LENGTH: 0.125 / 3.18 OVERALL LENGTH: 0.545 / 13.84 GRID WIDTH: 0.060 / 1.52 OVERALL WIDTH: 0.189 / 4.80 MATRIX SIZE: 0.62 L x 0.26 W / 15.8 L x 6.6 W	N2A-XX-S014N-350	350 ± 0.2%	N	E2

Note 1: All products are RoHS compliant.

VISHAY PRECISION GROUP

Full Bridge Patterns

Micro-Measurements

Transducer-Class® Strain Gages

GAGE PATTERN Actual size shown. Enlarged when necessary for definition. DIMENSIONS (inch / millimeter)	GAGE LENGTH	OVERALL LENGTH	GRID WIDTH	OVERALL WIDTH	GAGE DESIGNATION See Note 1	RES. IN OHMS	STANDARD CREEP CODE	ENCAPSULATION OPTION AVAILABLE
					Full-bridge pattern for single-surface gaging of transducers.			
	0.100	0.345	0.120	0.295				
	2.54	8.76	3.05	7.49	N2A-XX-S056R-350	350 ± 0.2%	R*	E2
	MATRIX SIZE	0.41 L x 0.36 W		10.4 L x 9.1 W	N2A-XX-S120P-10C	1000 ± 0.2%	P*	E2
					Low-cost full-bridge gage for bending-beam transducers. †BAL is balanced to ± 0.4mV/V, but RG is 1200 ohms ± 15%.			
	0.070	0.258	0.070	0.195				
	1.78	6.55	1.78	4.95				
	MATRIX SIZE	0.31 L x 0.25 W		7.9 L x 6.4 W	N2A-XX-S1449-1KB	BAL ± 0.4†	N/A	E2
					Low-cost, full-bridge pattern for bending-beam transducers. †BAL is balanced to ± 0.4mV/V, but RG is 350 ohms ± 15%.			
	0.070	0.238	0.070	0.190				
	1.78	6.04	1.78	4.83				
	MATRIX SIZE	0.27 L x 0.23 W		7.0 L x 5.8 W	N2A-XX-S1612-35B	BAL ± 0.4†	N/A	E2

*Only creep code available for this gage type.

Note 1: All products are RoHS compliant.

Disclaimer

ALL PRODUCTS, PRODUCT SPECIFICATIONS AND DATA ARE SUBJECT TO CHANGE WITHOUT NOTICE.

Vishay Precision Group, Inc., its affiliates, agents, and employees, and all persons acting on its or their behalf (collectively, "Vishay Precision Group"), disclaim any and all liability for any errors, inaccuracies or incompleteness contained herein or in any other disclosure relating to any product.

The product specifications do not expand or otherwise modify Vishay Precision Group's terms and conditions of purchase, including but not limited to, the warranty expressed therein.

Vishay Precision Group makes no warranty, representation or guarantee other than as set forth in the terms and conditions of purchase. **To the maximum extent permitted by applicable law, Vishay Precision Group disclaims (i) any and all liability arising out of the application or use of any product, (ii) any and all liability, including without limitation special, consequential or incidental damages, and (iii) any and all implied warranties, including warranties of fitness for particular purpose, non-infringement and merchantability.**

Information provided in datasheets and/or specifications may vary from actual results in different applications and performance may vary over time. Statements regarding the suitability of products for certain types of applications are based on Vishay Precision Group's knowledge of typical requirements that are often placed on Vishay Precision Group products. It is the customer's responsibility to validate that a particular product with the properties described in the product specification is suitable for use in a particular application.

No license, express, implied, or otherwise, to any intellectual property rights is granted by this document, or by any conduct of Vishay Precision Group.

The products shown herein are not designed for use in life-saving or life-sustaining applications unless otherwise expressly indicated. Customers using or selling Vishay Precision Group products not expressly indicated for use in such applications do so entirely at their own risk and agree to fully indemnify Vishay Precision Group for any damages arising or resulting from such use or sale. Please contact authorized Vishay Precision Group personnel to obtain written terms and conditions regarding products designed for such applications.

Product names and markings noted herein may be trademarks of their respective owners.

APPENDIX F

APPENDIX F

ELECTRICAL COMPONENTS AND SCHEMATICS

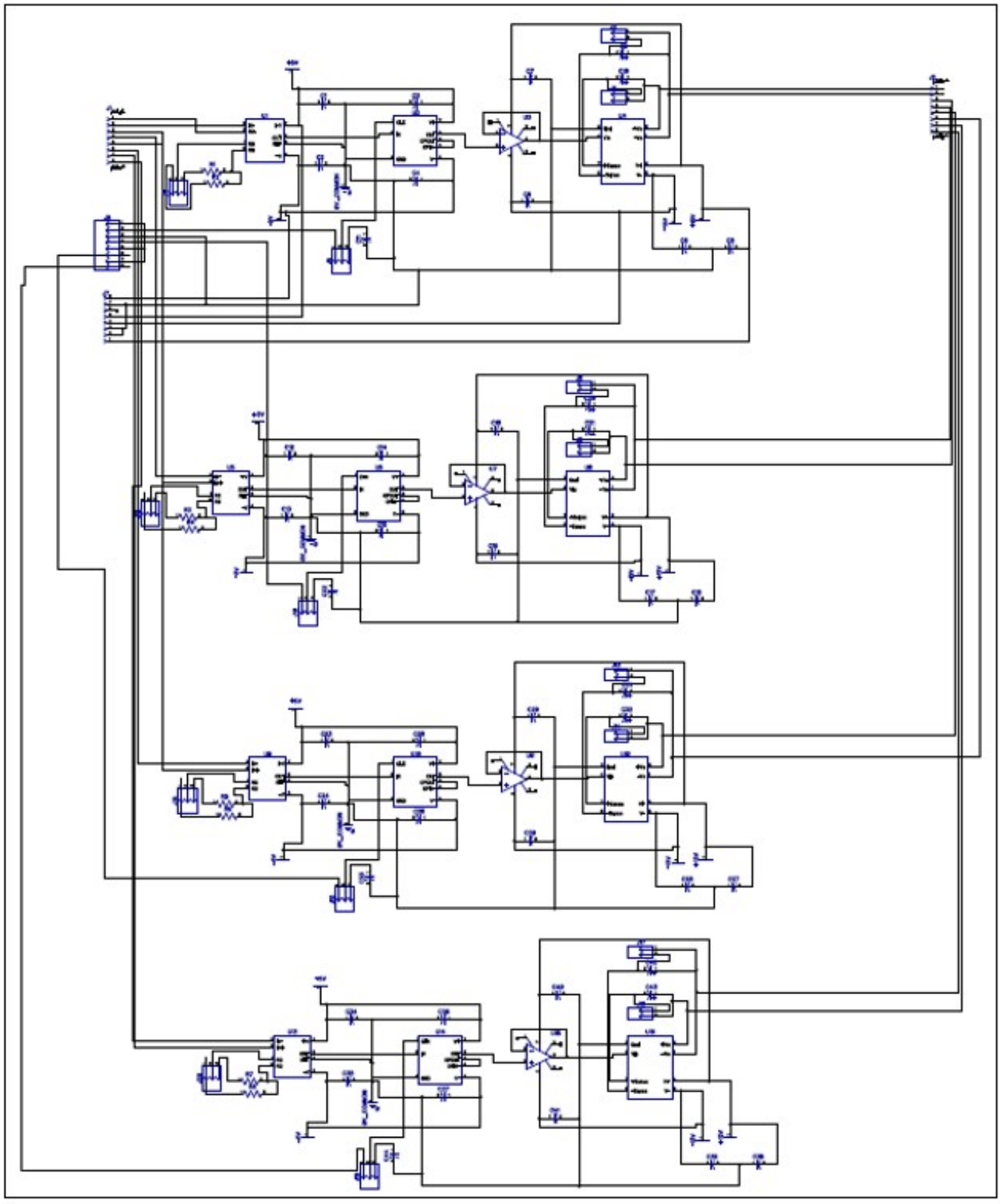

Original Circuitry Box Load Schematic

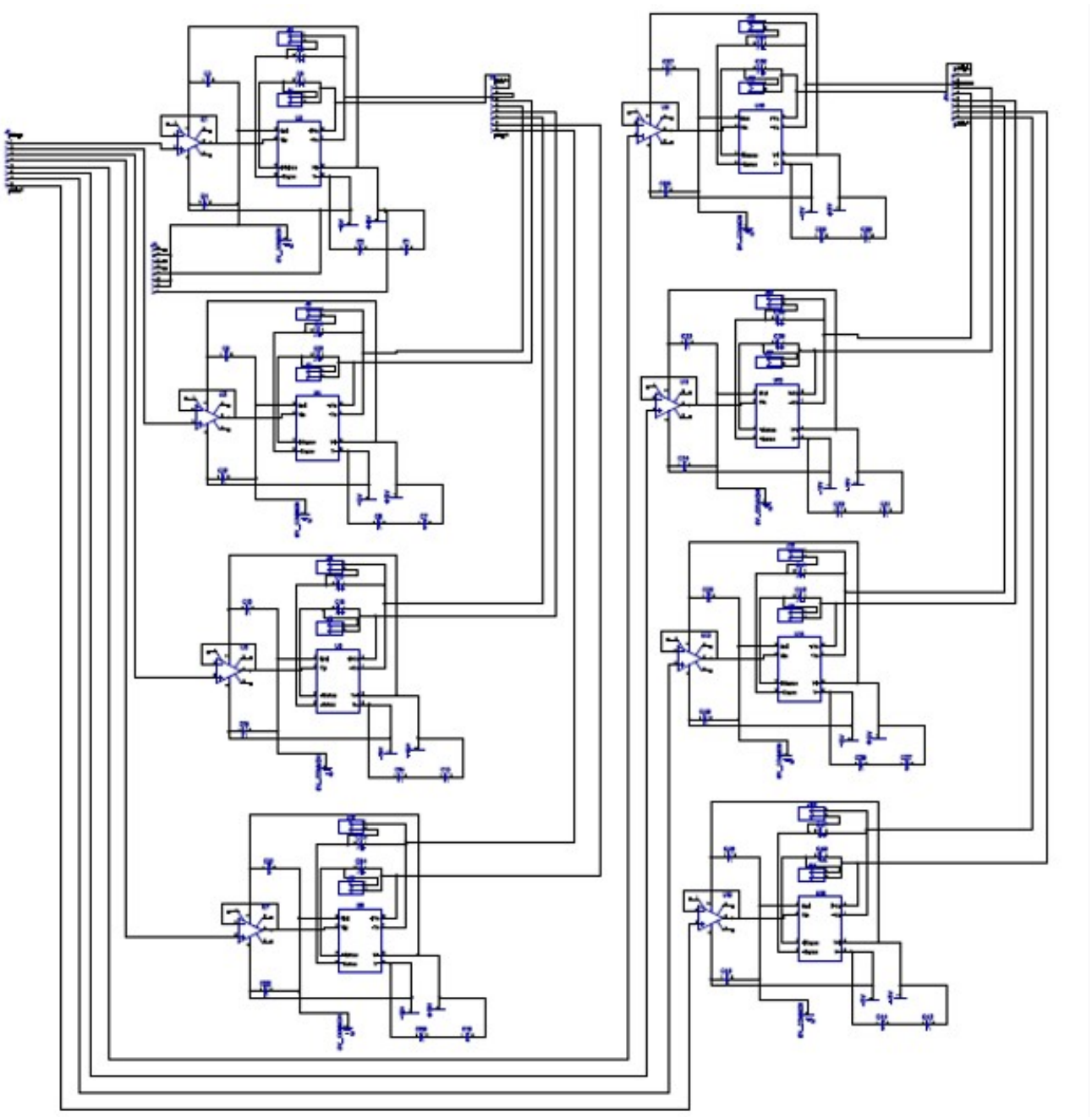

Original Circuitry Box Temperature Schematic

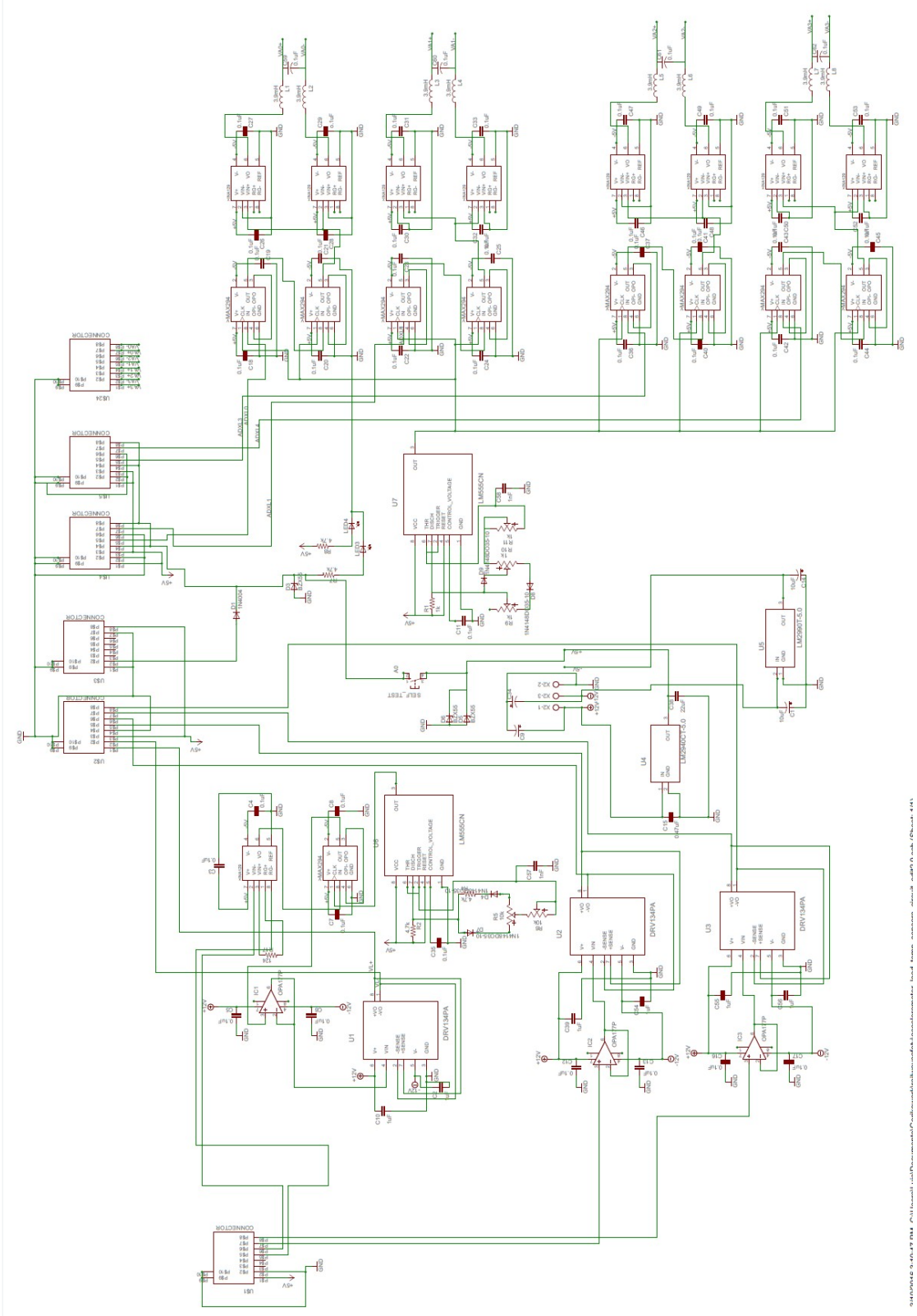

Redesigned Circuitry Box

Burr-Brown Products from Texas Instruments

INA128
INA129

SBOS051B – OCTOBER 1995 – REVISED FEBRUARY 2005

Precision, Low Power INSTRUMENTATION AMPLIFIERS

FEATURES

- LOW OFFSET VOLTAGE: 50µV max
- LOW DRIFT: 0.5µV/°C max
- LOW INPUT BIAS CURRENT: 5nA max
- HIGH CMR: 120dB min
- INPUTS PROTECTED TO ±40V
- WIDE SUPPLY RANGE: ±2.25V to ±18V
- LOW QUIESCENT CURRENT: 700µA
- 8-PIN PLASTIC DIP, SO-8

APPLICATIONS

- BRIDGE AMPLIFIER
- THERMOCOUPLE AMPLIFIER
- RTD SENSOR AMPLIFIER
- MEDICAL INSTRUMENTATION
- DATA ACQUISITION

DESCRIPTION

The INA128 and INA129 are low power, general purpose instrumentation amplifiers offering excellent accuracy. The versatile 3-op amp design and small size make them ideal for a wide range of applications. Current-feedback input circuitry provides wide bandwidth even at high gain (200kHz at G = 100).

A single external resistor sets any gain from 1 to 10,000. The INA128 provides an industry-standard gain equation; the INA129 gain equation is compatible with the AD620.

The INA128/INA129 is laser trimmed for very low offset voltage (50µV), drift (0.5µV/°C) and high common-mode rejection (120dB at G ≥ 100). It operates with power supplies as low as ±2.25V, and quiescent current is only 700µA—ideal for battery-operated systems. Internal input protection can withstand up to ±40V without damage.

The INA128/INA129 is available in 8-pin plastic DIP and SO-8 surface-mount packages, specified for the –40°C to +85°C temperature range. The INA128 is also available in a dual configuration, the INA2128.

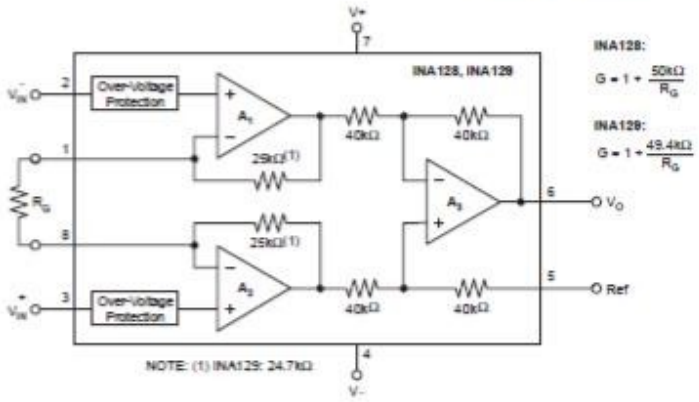

ABSOLUTE MAXIMUM RATINGS(1)

Supply Voltage	±18V
Analog Input Voltage Range	±40V
Output Short-Circuit (to ground)	Continuous
Operating Temperature	–40°C to +125°C
Storage Temperature Range	–55°C to +125°C
Junction Temperature	+150°C
Lead Temperature (soldering, 10s)	+300°C

(1) Stresses above these ratings may cause permanent damage. Exposure to absolute maximum conditions for extended periods may degrade device reliability. These are stress ratings only, and functional operation of the device at these or any other conditions beyond those specified is not implied.

ELECTROSTATIC DISCHARGE SENSITIVITY

This integrated circuit can be damaged by ESD. Texas Instruments recommends that all integrated circuits be handled with appropriate precautions. Failure to observe proper handling and installation procedures can cause damage.

ESD damage can range from subtle performance degradation to complete device failure. Precision integrated circuits may be more susceptible to damage because very small parametric changes could cause the device not to meet its published specifications.

ORDERING INFORMATION

For the most current package and ordering information, see the Package Option Addendum located at the end of this data sheet.

PIN CONFIGURATION

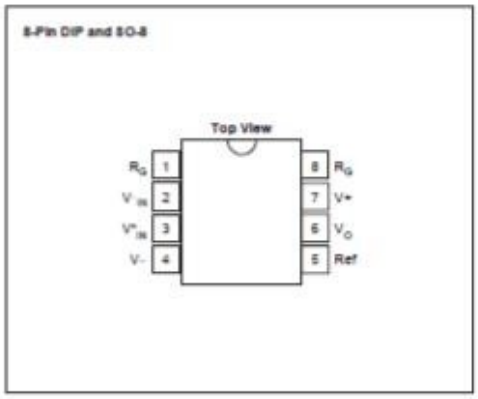

ELECTRICAL CHARACTERISTICS

At T_A = +25°C, V_S = ±15V, R_L = 10kΩ, unless otherwise noted.

PARAMETER	CONDITIONS	INA128P, U INA129P, U			INA128PA, UA INA129PA, UA			UNIT
		MIN	TYP	MAX	MIN	TYP	MAX	
INPUT								
Offset Voltage, RTI								
Initial	T_A = +25°C		±10±100/G	±50±500/G		±25±100/G	±125±1000/G	µV
vs Temperature	T_A = T_{MIN} to T_{MAX}		±0.2±2/G	±0.5±20/G		±0.2±5/G	±1±20/G	µV/°C
vs Power Supply	V_S = ±2.25V to ±18V		±0.2±20/G	±1±100/G		*	±2±200/G	µV/V
Long-Term Stability			±0.1±3/G			*		µV/mo
Impedance, Differential			10^{10} || 2			*		Ω || pF
Common-Mode			10^{11} || 9			*		Ω || pF
Common-Mode Voltage Range[1]	V_O = 0V	(V+) – 2	(V+) – 1.4		*	*		V
		(V–) + 2	(V–) + 1.7		*	*		V
Safe Input Voltage				±40			*	V
Common-Mode Rejection	V_{CM} = ±13V, ΔR_S = 1kΩ							
	G = 1	80	86		73	*		dB
	G = 10	100	106		93	*		dB
	G = 100	120	125		110	*		dB
	G = 1000	120	130		110	*		dB
BIAS CURRENT			±2	±5		*	±10	nA
vs Temperature			±30			*		pA/°C
Offset Current			±1	±5		*	±10	nA
vs Temperature			±30			*		pA/°C
NOISE VOLTAGE, RTI	G = 1000, R_S = 0Ω							
f = 10Hz			10			*		nV/√Hz
f = 100Hz			8			*		nV/√Hz
f = 1kHz			8			*		nV/√Hz
f_B = 0.1Hz to 10Hz			0.2			*		μV_{pp}
Noise Current								
f = 10Hz			0.9			*		pA/√Hz
f = 1kHz			0.3			*		pA/√Hz
f_B = 0.1Hz to 10Hz			30			*		pA_{pp}
GAIN								
Gain Equation, INA128			1 + (50kΩ/R_G)			*		V/V
INA129			1 + (49.4kΩ/R_G)			*		V/V
Range of Gain		1		10000	*		*	V/V
Gain Error	G = 1		±0.01	±0.024		*	±0.1	%
	G = 10		±0.02	±0.4		*	±0.5	%
	G = 100		±0.05	±0.5		*	±0.7	%
	G = 1000		±0.5	±1		*	±2	%
Gain vs Temperature[2]	G = 1		±1	±10		*	*	ppm/°C
50kΩ (or 49.4kΩ) Resistance[2][3]			±25	±100		*	*	ppm/°C
Nonlinearity	V_O = ±13.6V, G = 1		±0.0001	±0.001		*	±0.002	% of FSR
	G = 10		±0.0003	±0.002		*	±0.004	% of FSR
	G = 100		±0.0005	±0.002		*	±0.004	% of FSR
	G = 1000		±0.001	[4]		*	*	% of FSR

NOTE: * Specification is same as INA128P, U or INA129P, U.

(1) Input common-mode range varies with output voltage — see typical curves.

(2) Specified by wafer test.

(3) Temperature coefficient of the 50kΩ (or 49.4kΩ) term in the gain equation.

(4) Nonlinearity measurements in G = 1000 are dominated by noise. Typical nonlinearity is ±0.001%.

ELECTRICAL CHARACTERISTICS (continued)

At T_A = +25°C, V_S = ±15V, R_L = 10kΩ, unless otherwise noted.

PARAMETER	CONDITIONS	INA128P, U INA129P, U			INA128PA, UA INA129PA, UA			UNIT
		MIN	TYP	MAX	MIN	TYP	MAX	
OUTPUT								
Voltage: Positive	R_L = 10kΩ	(V+) + 1.4	(V+) + 0.9		*	*		V
Negative	R_L = 10kΩ	(V−) + 1.4	(V−) + 0.8		*	*		V
Load Capacitance Stability			1000			*		pF
Short-Circuit Current			+6/−15			*		mA
FREQUENCY RESPONSE								
Bandwidth, −3dB	G = 1		1.3			*		MHz
	G = 10		700			*		kHz
	G = 100		200			*		kHz
	G = 1000		20			*		kHz
Slew Rate	V_O = ±10V, G = 10		4			*		V/µs
Settling Time, 0.01%	G = 1		7			*		µs
	G = 10		7			*		µs
	G = 100		9			*		µs
	G = 1000		80			*		µs
Overload Recovery	50% Overdrive		4			*		µs
POWER SUPPLY								
Voltage Range		±2.25	±15	±18	*	*	*	V
Current, Total	V_{IN} = 0V		±700	±750		*	*	µA
TEMPERATURE RANGE								
Specification		−40		+85	*		*	°C
Operating		−40		+125	*		*	°C
θ_{JA} 8-Pin DIP			80			*		°C/W
SO-8 SOIC			150			*		°C/W

NOTE: * Specification is same as INA128P, U or INA129P, U.

(1) Input common-mode range varies with output voltage — see typical curves.

(2) Specified by wafer test.

(3) Temperature coefficient of the 50kΩ (or 49.4kΩ) term in the gain equation.

(4) Nonlinearity measurements in G = 1000 are dominated by noise. Typical nonlinearity is ±0.001%.

APPLICATIONS INFORMATION

Figure 1 shows the basic connections required for operation of the INA128/INA129. Applications with noisy or high impedance power supplies may require decoupling capacitors close to the device pins as shown.

The output is referred to the output reference (Ref) terminal which is normally grounded. This must be a low-impedance connection to assure good common-mode rejection. A resistance of 8Ω in series with the Ref pin will cause a typical device to degrade to approximately 80dB CMR (G = 1).

SETTING THE GAIN

Gain is set by connecting a single external resistor, R_G, connected between pins 1 and 8:

INA128:

$$G = 1 + \frac{50k\Omega}{R_G} \quad (1)$$

INA129:

$$G = 1 + \frac{49.4k\Omega}{R_G} \quad (2)$$

Commonly used gains and resistor values are shown in Figure 1.

The 50kΩ term in Equation 1 (49.4kΩ in Equation 2) comes from the sum of the two internal feedback resistors of A_1 and A_2. These on-chip metal film resistors are laser trimmed to accurate absolute values. The accuracy and temperature coefficient of these internal resistors are included in the gain accuracy and drift specifications of the INA128/INA129.

The stability and temperature drift of the external gain setting resistor, R_G, also affects gain. R_G's contribution to gain accuracy and drift can be directly inferred from the gain equation (1). Low resistor values required for high gain can make wiring resistance important. Sockets add to the wiring resistance which will contribute additional gain error (possibly an unstable gain error) in gains of approximately 100 or greater.

DYNAMIC PERFORMANCE

The typical performance curve *Gain vs Frequency* shows that, despite its low quiescent current, the INA128/INA129 achieves wide bandwidth, even at high gain. This is due to the current-feedback topology of the input stage circuitry. Settling time also remains excellent at high gain.

NOISE PERFORMANCE

The INA128/INA129 provides very low noise in most applications. Low frequency noise is approximately $0.2\mu V_{PP}$ measured from 0.1 to 10Hz (G ≥ 100). This provides dramatically improved noise when compared to state-of-the-art chopper-stabilized amplifiers.

INA128: $G = 1 + \frac{50k\Omega}{R_G}$ INA129: $G = 1 + \frac{49.4k\Omega}{R_G}$

DESIRED GAIN (V/V)	INA128 R_G (Ω)	INA128 NEAREST 1% R_G (Ω)	INA129 R_G (Ω)	INA129 NEAREST 1% R_G (Ω)
1	NC	NC	NC	NC
2	50.00k	49.9k	49.4k	49.9k
5	12.50k	12.4k	12.35k	12.4k
10	5.556k	5.62k	5489	5.49k
20	2.632k	2.61k	2600	2.61k
50	1.02k	1.02k	1008	1k
100	505.1	511	499	499
200	251.3	249	248	249
500	100.2	100	99	100
1000	50.05	49.9	49.5	49.9
2000	25.01	24.9	24.7	24.9
5000	10.00	10	9.88	9.76
10000	5.001	4.99	4.94	4.87

NC: No Connection

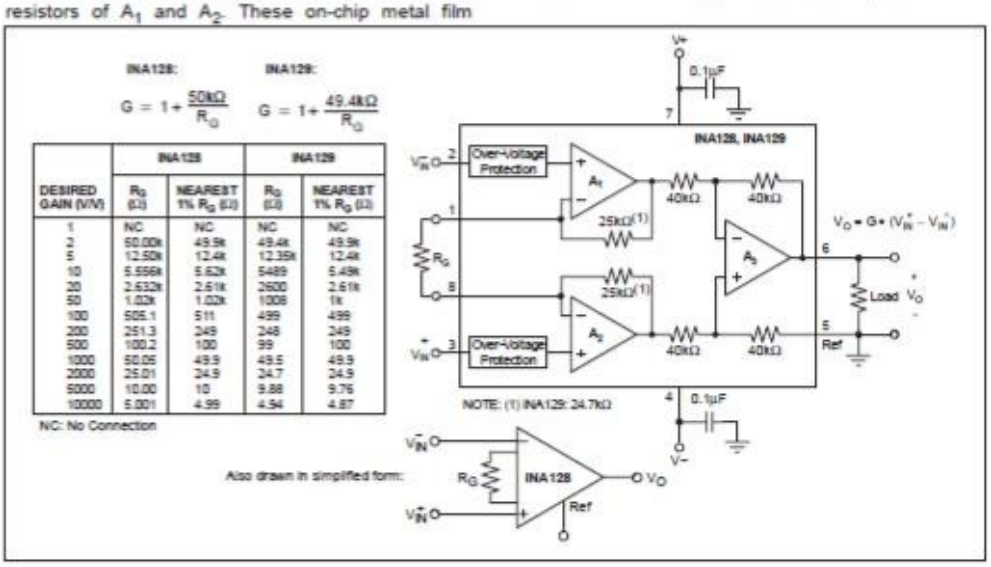

Figure 1. Basic Connections

OFFSET TRIMMING

The INA128/INA129 is laser trimmed for low offset voltage and offset voltage drift. Most applications require no external offset adjustment. Figure 2 shows an optional circuit for trimming the output offset voltage. The voltage applied to Ref terminal is summed with the output. The op amp buffer provides low impedance at the Ref terminal to preserve good common-mode rejection.

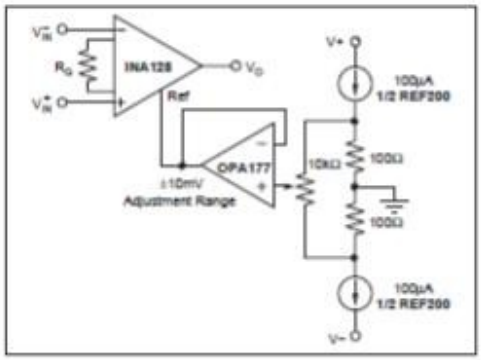

Figure 2. Optional Trimming of Output Offset Voltage

INPUT BIAS CURRENT RETURN PATH

The input impedance of the INA128/INA129 is extremely high—approximately $10^{10}\Omega$. However, a path must be provided for the input bias current of both inputs. This input bias current is approximately ±2nA. High input impedance means that this input bias current changes very little with varying input voltage.

Input circuitry must provide a path for this input bias current for proper operation. Figure 3 shows various provisions for an input bias current path. Without a bias current path, the inputs will float to a potential which exceeds the common-mode range, and the input amplifiers will saturate.

If the differential source resistance is low, the bias current return path can be connected to one input (see the thermocouple example in Figure 3). With higher source impedance, using two equal resistors provides a balanced input with possible advantages of lower input offset voltage due to bias current and better high-frequency common-mode rejection.

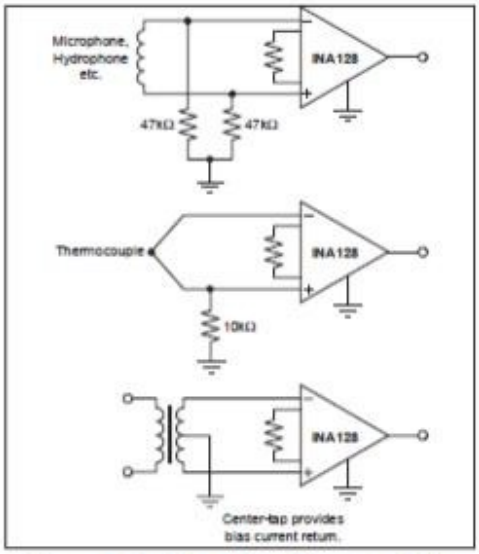

Figure 3. Providing an Input Common-Mode Current Path

INPUT COMMON-MODE RANGE

The linear input voltage range of the input circuitry of the INA128/INA129 is from approximately 1.4V below the positive supply voltage to 1.7V above the negative supply. As a differential input voltage causes the output voltage increase, however, the linear input range will be limited by the output voltage swing of amplifiers A_1 and A_2. So the linear common-mode input range is related to the output voltage of the complete amplifier. This behavior also depends on supply voltage—see performance curves, *Input Common-Mode Range vs Output Voltage*.

Input-overload can produce an output voltage that appears normal. For example, if an input overload condition drives both input amplifiers to their positive output swing limit, the difference voltage measured by the output amplifier will be near zero. The output of A_3 will be near 0V even though both inputs are overloaded.

LOW VOLTAGE OPERATION

The INA128/INA129 can be operated on power supplies as low as ±2.25V. Performance remains excellent with power supplies ranging from ±2.25V to ±18V. Most parameters vary only slightly throughout this supply voltage range—see typical performance curves.

Operation at very low supply voltage requires careful attention to assure that the input voltages remain within their linear range. Voltage swing requirements of internal nodes limit the input common-mode range with low power supply voltage. Typical performance curves, "Input Common-Mode Range vs Output Voltage" show the range of linear operation for ±15V, ±5V, and ±2.5V supplies.

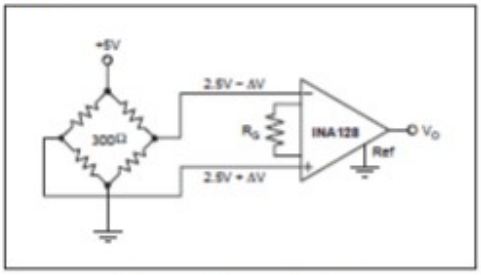

Figure 4. Bridge Amplifier

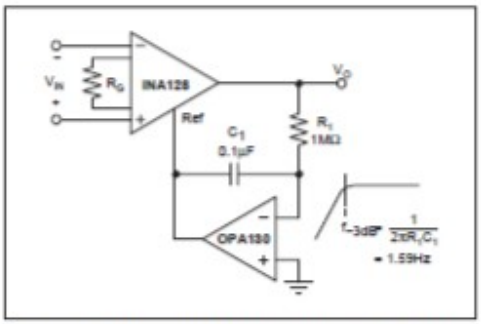

Figure 5. AC-Coupled Instrumentation Amplifier

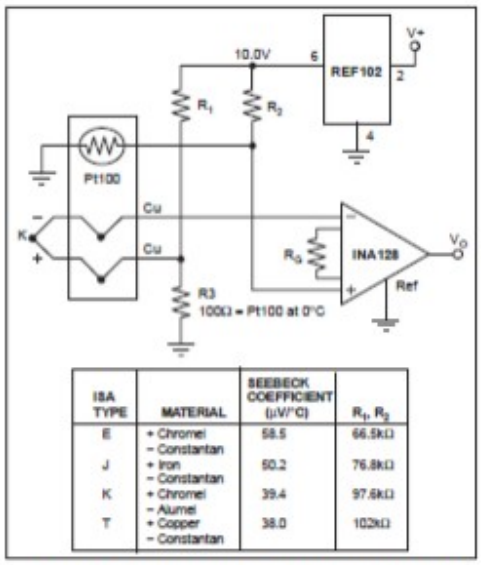

ISA TYPE	MATERIAL	SEEBECK COEFFICIENT (µV/°C)	R_1, R_2
E	+ Chromel – Constantan	58.5	66.5kΩ
J	+ Iron – Constantan	50.2	76.8kΩ
K	+ Chromel – Alumel	39.4	97.6kΩ
T	+ Copper – Constantan	38.0	102kΩ

Figure 6. Thermocouple Amplifier with RTD Cold-Junction Compensation

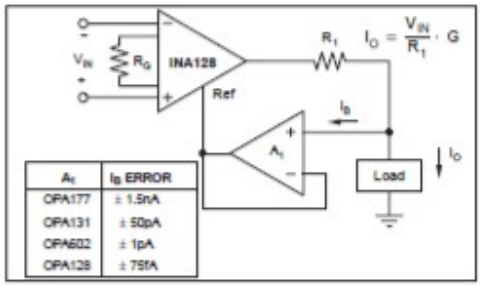

A_1	I_B ERROR
OPA177	± 1.5nA
OPA131	± 50pA
OPA602	± 1pA
OPA128	± 75fA

Figure 7. Differential Voltage to Current Converter

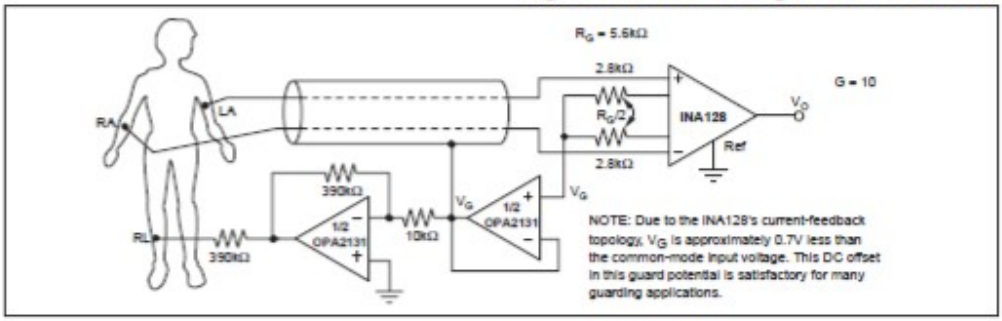

Figure 8. ECG Amplifier with Right-Leg Drive

19-0020; Rev 2; 06/08

MAXIM

8th-Order, Lowpass, Elliptic, Switched-Capacitor Filters

General Description

The MAX293/MAX294/MAX297 are easy-to-use, 8th-order, lowpass, elliptic, switched-capacitor filters that can be set up with corner frequencies from 0.1Hz to 25kHz (MAX293/MAX294) or from 0.1Hz to 50kHz (MAX297).

The MAX293/MAX297's 1.5 transition ratio provides sharp rolloff and -80dB of stopband rejection. The MAX294's 1.2 transition ratio provides the steepest rolloff and -58dB of stopband rejection. All three filters have fixed responses, so the design task is limited to selecting the clock frequency that controls the filter's corner frequency.

An external capacitor is used to generate a clock using the internal oscillator, or an external clock signal can be used. An uncommitted op amp (noninverting input grounded) is provided for building a continuous-time lowpass filter for post-filtering or anti-aliasing. Steep rolloff and high order make these filters ideal for anti-aliasing applications that require maximum bandwidth, and for communication applications that require filtering signals in close proximity within the frequency domain.

The MAX293/MAX294/MAX297 are available in 8-pin DIP and 16-pin wide SO packages, delivering aggressive performance from a tiny area.

Applications

Data-Acquisition Systems

Anti-Aliasing

DAC Post-Filtering

Voice/Data Signal Filtering

Typical Operating Circuit

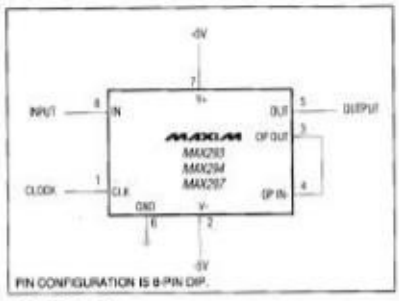

PIN CONFIGURATION IS 8-PIN DIP.

Features

- **8th-Order Lowpass Elliptic Filters**
- **Clock-Tunable Corner-Frequency Range:**
  0.1Hz to 25kHz (MAX293/MAX294)
  0.1Hz to 50kHz (MAX297)
- **No External Resistors or Capacitors Required**
- **Internal or External Clock**
- **Clock to Corner Frequency Ratio:**
  100:1 (MAX293/294)
  50:1 (MAX297)
- **Operate with a Single +5V Supply or Dual ±5V Supplies**
- **Uncommitted Op Amp for Anti-Aliasing or Clock-Noise Filtering**
- **8-Pin DIP and 16-Pin Wide SO Packages**

Ordering Information

PART	TEMP. RANGE	PIN-PACKAGE
MAX293CPA	0°C to +70°C	8 Plastic DIP
MAX293CWE	0°C to +70°C	16 Wide SO
MAX293C/D	0°C to +70°C	Dice*
MAX293EPA	-40°C to +85°C	8 Plastic DIP
MAX293EWE	-40°C to +85°C	16 Wide SO
MAX293MJA	-55°C to +125°C	8 CERDIP**
MAX294CPA	0°C to +70°C	8 Plastic DIP
MAX294CWE	0°C to +70°C	16 Wide SO
MAX294C/D	0°C to +70°C	Dice*

Ordering Information continued on last page.

* *Contact factory for dice specifications.*

** *Contact factory for availability and processing to MIL-STD-883.*

Pin Configurations

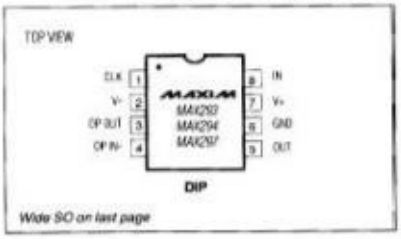

Wide SO on last page

8th-Order, Lowpass, Elliptic, Switched-Capacitor Filters

ABSOLUTE MAXIMUM RATINGS

Supply Voltage (V+ to V-) 12V
Input Voltage at Any Pin ..... (V- - 0.3V) ≤ V_{IN} ≤ (V+ + 0.3V)
Continuous Power Dissipation
8-Pin Plastic DIP (derate 9.09mW/°C above +70°C) 727mW
16-Pin Wide SO (derate 9.52mW/°C above +70°C) 762mW
8-Pin CERDIP (derate 8.00mW/°C above +70°C) 640mW

Operating Temperature Ranges:
MAX29_C_ ..... 0°C to +70°C
MAX29_E_ ..... -40°C to +85°C
MAX29_MJA ..... -55°C to +125°C
Storage Temperature Range ..... -65°C to +160°C
Lead Temperature (soldering, 10 sec) ..... +300°C

Stresses beyond those listed under "Absolute Maximum Ratings" may cause permanent damage to the device. These are stress ratings only, and functional operation of the device at these or any other conditions beyond those indicated in the operational sections of the specifications is not implied. Exposure to absolute maximum rating conditions for extended periods may affect device reliability.

ELECTRICAL CHARACTERISTICS

(V+ = 5V, V- = -5V, filter output measured at OUT pin, 20kΩ load resistor to ground at OUT, f_{CLK} = 100kHz (MAX293/MAX294) or f_{CLK} = 50kHz (MAX297) T_A = T_{MIN} to T_{MAX}, unless otherwise noted.)

PARAMETER	CONDITIONS		MIN	TYP	MAX	UNITS
FILTER CHARACTERISTICS						
Corner Frequency Range	MAX293/MAX294			0.1-25k		Hz
	MAX297			0.1-50k		
Clock to Corner Frequency Ratio	MAX293/MAX294			100:1		
	MAX297			50:1		
Clock to Corner Frequency Tempco	MAX293			9		ppm/°C
	MAX294			7		
	MAX297			4		
Insertion Gain Relative to DC Gain (Note 1)	MAX293	f_{IN} = 0.381F_0	0.12	-0.10	-0.17	dB
		f_{IN} = 0.594F_0	0.12	0.02	-0.17	
		f_{IN} = 0.759F_0	0.12	-0.11	-0.17	
		f_{IN} = 0.866F_0	0.12	-0.03	-0.17	
		f_{IN} = 0.939F_0	0.12	-0.11	-0.17	
		f_{IN} = 0.993F_0	0.22	0.04	-0.17	
		f_{IN} = 1.000F_0	0.22	0.01	-0.17	
		f_{IN} = 1.500F_0	-73	-78		
		f_{IN} = 1.610F_0	-80	-87		
		f_{IN} = 2.020F_0	-80	-84		
		f_{IN} =4.020F_0	-80	-84		
	MAX294	f_{IN} = 0.425F_0	0.10	-0.11	-0.17	
		f_{IN} = 0.644F_0	0.10	0.02	-0.17	
		f_{IN} = 0.802F_0	0.10	-0.10	-0.17	
		f_{IN} = 0.895F_0	0.10	-0.03	-0.17	
		f_{IN} = 0.946F_0	0.10	-0.07	-0.17	
		f_{IN} = 0.994F_0	0.36	0.16	-0.17	
		f_{IN} = 1.000F_0	0.36	0.13	-0.17	
		f_{IN} = 1.200F_0	-49	-54		
		f_{IN} = 1.270F_0	-57	-62		
		f_{IN} = 1.530F_0	-57	-60		
		f_{IN} = 2.040F_0	-57	-60		

ELECTRICAL CHARACTERISTICS (continued)

(V+ = 5V, V- = -5V, filter output measured at OUT pin, 20kΩ load resistor to ground at OUT, f_{CLK} = 100kHz (MAX293/MAX294) or f_{CLK} = 50kHz (MAX297) $T_A = T_{MIN}$ to T_{MAX}, unless otherwise noted.)

PARAMETER	CONDITIONS		MIN	TYP	MAX	UNITS
Insertion Gain Relative to DC Gain (Note 1) (continued)	MAX297	$f_{IN} = 0.377F_0$	0.10	-0.11	-0.17	dB
		$f_{IN} = 0.591F_0$	0.10	0.03	-0.17	
		$f_{IN} = 0.754F_0$	0.10	-0.12	-0.17	
		$f_{IN} = 0.873F_0$	0.10	0.02	-0.17	
		$f_{IN} = 0.944F_0$	0.10	-0.07	-0.17	
		$f_{IN} = 0.996F_0$	0.30	0.11	-0.17	
		$f_{IN} = 1.000F_0$	0.30	0.10	-0.17	
		$f_{IN} = 1.500F_0$	-73	-79		
		$f_{IN} = 1.610F_0$	-80	-87		
		$f_{IN} = 2.020F_0$	-80	-84		
		$f_{IN} = 4.000F_0$	-80	-85		
Passband Ripple	MAX293			0.15		dB
	MAX294			0.27		
	MAX297			0.23		
Output DC Swing			±4			V
Output Offset Voltage	IN = GND			±150	±400	mV
DC Insertion Gain with Output Offset Removed			-0.15	±0.01	0.15	dB
Total Harmonic Distortion plus Noise	T_A = +25°C	MAX293		-71		dB
		MAX294		-69		
		MAX297		-77		
Clock Feedthrough	T_A = +25°C			5.0		mVp-p
Output Drive Capability			20	10		kΩ
CLOCK						
Internal Oscillator Frequency	C_{OSC} = 1000pF		29	35	43	kHz
Internal Oscillator Current Source/Sink	V_{CLK} = 0V or 5V			±70	±120	µA
Clock Input (Note 2) High			4.0			V
Low					1.0	
UNCOMMITTED OP AMP						
Input Offset Voltage				±10	±50	mV
Output Drive Capability			20	10		kΩ
Output DC Swing			±4			V
Gain-Bandwidth Product				4		MHz
POWER REQUIREMENTS						
Supply Voltage Dual Supply			±2.375		±5.5	V
Single Supply	V- = 0V, GND = V+/2		4.75		11.0	
Supply Current	V+ = 5V, V- = -5V, V_{CLK} = 0V to 5V			15.0	22.0	mA
	V+ = 2.375V, V- = -2.375V, V_{CLK} = -2V to 2V			7.0	12.0	

Note 1: Test frequencies selected at ripple peaks and troughs.
Note 2: Guaranteed by design.

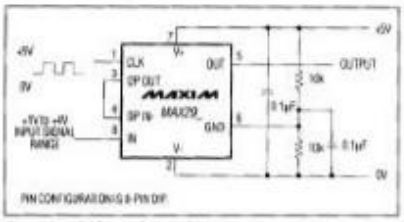

Figure 3. +5V Single-Supply Operation

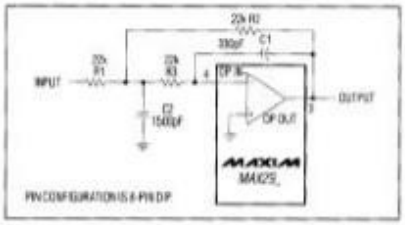

Figure 4. Uncommitted Op Amp Configured as a 2nd-Order Butterworth Lowpass Filter (F_C = 10kHz)

same mismatch in a ladder filter design will spread its error over all poles.

Clock-Signal Requirements

The MAX293/MAX294/MAX297 maximum recommended clock frequency is 2.5MHz, producing a cutoff frequency of 25kHz for the MAX293/MAX294 and 50kHz for the MAX297. The CLK pin can be driven by an external clock or by the internal oscillator with an external capacitor. For external clock applications, the clock circuitry has been designed to interface with +5V CMOS logic. Drive the CLK pin with a CMOS gate powered from 0V and +5V when using either a single supply or dual ±5V supplies. Varying the rate of an external clock will dynamically adjust the filter's corner frequency.

When using the internal oscillator, the capacitance (C_{OSC}) on the CLK pin determines the oscillator frequency:

$$f_{OSC(kHz)} \approx \frac{10^5}{3C_{OSC(pF)}}$$

The stray capacitance at CLK should be minimized, since it will affect the internal oscillator frequency.

Applications Information

Power Supplies

The MAX293/MAX294/MAX297 operate from either dual or single power supplies. The dual-supply voltage range is ±2.375V to ±5.5V (0.1µF bypass capacitors from each supply to GND are recommended). When using a single supply, tie the V- pin to ground and bias the GND pin to the mid-supply point using a resistor-divider network, as shown in Figure 3.

Input-Signal Amplitude Range

The ideal input-signal range is determined by observing at what voltage level the signal-to-noise plus distortion (SINAD) ratio is maximized for a given corner frequency. The *Typical Operating Characteristics* show the MAX293/MAX294/MAX297 THD + Noise response as the input signal's peak-to-peak amplitude is varied.

Uncommitted Op Amp

The uncommitted op amp has its noninverting input connected to the GND pin, and can be used to build a 1st- or 2nd-order continuous-time lowpass filter. This filter is intended for anti-aliasing applications preceding the switched-capacitor filter, but it can be used as a post-filter to reduce clock noise. Figure 4 shows one of many filters that can be built with this op amp: a 2nd-order Butterworth filter with a 10kHz corner frequency and an input impedance greater than 22kΩ. Table 1 gives alternative component values for different corner frequencies of the same Butterworth filter.

Table 1. Component Values for Figure 4's Filter

Corner Freq. (Hz)	R1 (kΩ)	R2 (kΩ)	R3 (kΩ)	C1 (F)	C2 (F)
100k	10	10	10	68p	330p
50k	20	20	20	68p	330p
25k	20	20	20	150p	680p
10k	22	22	22	330p	1.5n
1k	22	22	22	3.3n	15n
100	22	22	22	33n	150n
10	22	22	22	330n	1.5µ

NOTE: Some approximations have been made in selecting preferred component values.

The passband error caused by a 2nd-order Butterworth can be calculated using the formula:

$$\text{Gain error} = -10\log\left[1+\left(\frac{f}{f_C}\right)^4\right] \text{ dB}$$

8th-Order, Lowpass, Elliptic, Switched-Capacitor Filters

As the passband ripple of the MAX293/MAX294/MAX297 elliptic filters is of the order of ±0.1dB, it is normally appropriate to keep the passband errors of any anti-aliasing filter at or below this level. This is achieved by choosing the corner frequency of Figure 4's Butterworth filter (f_{CB}) to be higher than the corner frequency of the elliptic switched-capacitor filter (f_{CE}) by a factor of 2.5 or more. A factor of 5 or more is recommended to avoid problems with component tolerances, i.e. $f_{CB} > (5)(f_{CE})$.

When using the uncommitted op amp as a post-filter to reduce clock noise, keep the filter's input impedance above 20kΩ to avoid excessive loading of the switched-capacitor filter. Note that the op amp experiences some clock feedthrough, so it is generally more useful for anti-aliasing than for clock-noise attenuation.

DAC Post-Filtering

When using the MAX293/MAX294/MAX297 for DAC post-filtering, synchronize the DAC and the filter clocks. If clocks are not synchronized, beat frequencies will alias into the desired passband. The DAC's clock should be generated by dividing down the switched-capacitor filter's clock.

Harmonic Distortion

Harmonic distortion arises from nonlinearities within the filter. These nonlinearities generate harmonics when a pure sine wave is applied to the filter input. Table 2 lists typical harmonic distortion values for the MAX293/MAX294/MAX297 with a 1kHz 5Vp-p sine wave input signal, a 1MHz clock frequency, and a 20kΩ load.

Table 2. Typical Harmonic Distortion (dB)

FILTER	HARMONIC			
	2nd	3rd	4th	5th
MAX293	70	90	88	92
MAX294	67	90	92	94
MAX297	84	89	93	99

Pin Configurations (continued)

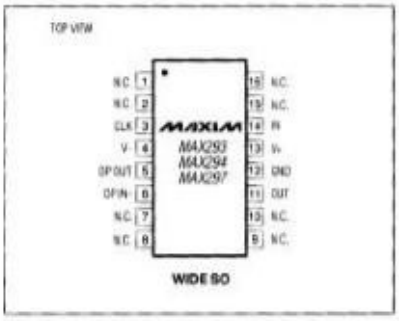

Ordering Information (continued)

PART	TEMP. RANGE	PIN-PACKAGE
MAX294EPA	-40°C to +85°C	8 Plastic DIP
MAX294EWE	-40°C to +85°C	16 Wide SO
MAX294MJA	-55°C to +125°C	8 CERDIP**
MAX297CPA	0°C to +70°C	8 Plastic DIP
MAX297CWE	0°C to +70°C	16 Wide SO
MAX297C/D	0°C to +70°C	Dice*
MAX297EPA	-40°C to +85°C	8 Plastic DIP
MAX297EWE	-40°C to +85°C	16 Wide SO
MAX297MJA	-55°C to +125°C	8 CERDIP**

*Contact factory for dice specifications.
**Contact factory for availability and processing to MIL-STD-883.

BURR-BROWN®

OPA177

Precision OPERATIONAL AMPLIFIER

FEATURES

- LOW OFFSET VOLTAGE: 25μV max
- LOW DRIFT: 0.3μV/°C
- HIGH OPEN-LOOP GAIN: 130dB min
- LOW QUIESCENT CURRENT: 1.5mA typ
- REPLACES INDUSTRY-STANDARD OP AMPS: OP-07, OP-77, OP-177, AD707, ETC.

APPLICATIONS

- PRECISION INSTRUMENTATION
- DATA ACQUISITION
- TEST EQUIPMENT
- BRIDGE AMPLIFIER
- THERMOCOUPLE AMPLIFIER

DESCRIPTION

The OPA177 precision bipolar op amp feature very low offset voltage and drift. Laser-trimmed offset, drift and input bias current virtually eliminate the need for costly external trimming. The high performance and low cost make them ideally suited to a wide range of precision instrumentation.

The low quiescent current of the OPA177 dramatically reduce warm-up drift and errors due to thermoelectric effects in input interconnections. It provides an effective alternative to chopper-stabilized amplifiers. The low noise of the OPA177 maintains accuracy.

OPA177 performance gradeouts are available. Packaging options include 8-pin plastic DIP and SO-8 surface-mount packages.

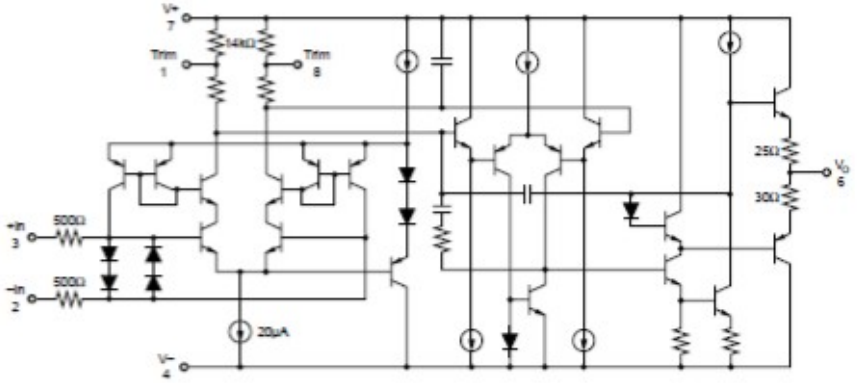

International Airport Industrial Park • Mailing Address: PO Box 11400, Tucson, AZ 85734 • Street Address: 6730 S. Tucson Blvd., Tucson, AZ 85706 • Tel: (520) 746-1111 • Twx: 910-952-1111
Internet: http://www.burr-brown.com/ • FAXLine: (800) 548-6133 (US/Canada Only) • Cable: BBRCORP • Telex: 066-6491 • FAX: (520) 889-1510 • Immediate Product Info: (800) 548-6132

PDS-1081E

Printed in U.S.A. August, 1997

SBOS008

OPA177 SPECIFICATIONS

At V_S = ±15V, T_A = +25°C, unless otherwise noted.

PARAMETER	CONDITION	OPA177F MIN	OPA177F TYP	OPA177F MAX	OPA177G MIN	OPA177G TYP	OPA177G MAX	UNITS
OFFSET VOLTAGE								
Input Offset Voltage			10	25		20	60	µV
Long-Term Input Offset[1] Voltage Stability			0.3			0.4		µV/Mo
Offset Adjustment Range	R_P = 20kΩ		±3			*		mV
Power Supply Rejection Ratio	V_S = ±3V to ±18V	115	125		110	120		dB
INPUT BIAS CURRENT								
Input Offset Current			0.3	1.5		*	2.8	nA
Input Bias Current			0.5	±2		*	±2.8	nA
NOISE								
Input Noise Voltage	1Hz to 100Hz[2]		85	160		*	*	nVrms
Input Noise Current	1Hz to 100Hz		4.5			*		pArms
INPUT IMPEDANCE								
Input Resistance	Differential Mode[3]	26	46		18.5	*		MΩ
	Common-Mode		200			*		GΩ
INPUT VOLTAGE RANGE								
Common-Mode Input Range[4]		±13	±14		*	*		V
Common-Mode Rejection	V_{CM} = ±13V	130	140		115	*		dB
OPEN-LOOP GAIN	R_L ≥ 2kΩ							
Large Signal Voltage Gain	V_O = ±10V[5]	5110	12,000		2000	6000		V/mV
OUTPUT								
Output Voltage Swing	R_L ≥ 10kΩ	±13.5	±14		*	*		V
	R_L ≥ 2kΩ	±12.5	±13		*	*		V
	R_L ≥ 1kΩ	±12	±12.5		*	*		V
Open-Loop Output Resistance			60			*		Ω
FREQUENCY RESPONSE								
Slew Rate	R_L ≥ 2kΩ	0.1	0.3		*	*		V/µs
Closed-Loop Bandwidth	G = +1	0.4	0.6		*	*		MHz
POWER SUPPLY								
Power Consumption	V_S = ±15V, No Load		40	60		*	*	mW
	V_S = ±3V, No Load		3.5	4.5		*	*	mW
Supply Current	V_S = ±15V, No Load		1.3	2		*	*	mA

At V_S = ±15V, −40°C ≤ T_A ≤ +85°C, unless otherwise noted.

OFFSET VOLTAGE								
Input Offset Voltage			15	40		20	100	µV
Average Input Offset Voltage Drift			0.1	0.3		0.7	1.2	µV/°C
Power Supply Rejection Ratio	V_S = ±3V to ±18V	110	120		106	115		dB
INPUT BIAS CURRENT								
Input Offset Current			0.5	2.2		*	4.5	nA
Average Input Offset Current Drift[6]			1.5	40		*	85	pA/°C
Input Bias Current			0.5	±4		*	±6	nA
Average Input Bias Current Drift[6]			8	40		15	60	pA/°C
INPUT VOLTAGE RANGE								
Common-Mode Input Range		±13	±13.5		*	*		V
Common-Mode Rejection	V_{CM} = ±13V	120	140		110	*		dB
OPEN-LOOP GAIN								
Large Signal Voltage Gain	R_L ≥ 2kΩ, V_O = ±10V	2000	6000		1000	4000		V/mV
OUTPUT								
Output Voltage Swing	R_L ≥ 2kΩ	±12	±13		*	*		V
POWER SUPPLY								
Power Consumption	V_S = ±15V, No Load		60	75		*	*	mW
Supply Current	V_S = ±15V, No Load		2	25		*	*	mA

* Same as specification for product to left.

NOTES: (1) Long-Term Input Offset Voltage Stability refers to the averaged trend line of V_{OS} vs time over extended periods after the first 30 days of operation. Excluding the initial hour of operation, changes in V_{OS} during the first 30 operating days are typically less than 2µV. (2) Sample tested. (3) Guaranteed by design. (4) Guaranteed by CMRR test condition. (5) To insure high open-loop gain throughout the ±10V output range, A_{OL} is tested at −10V ≤ V_O ≤ 0V, 0V ≤ V_O ≤ +10V, and −10V ≤ V_O ≤ +10V. (6) Guaranteed by end-point limits.

PIN CONFIGURATION

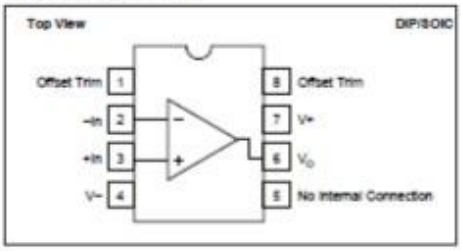

ABSOLUTE MAXIMUM RATINGS

Power Supply Voltage	±22V
Differential Input Voltage	±30V
Input Voltage	$\pm V_S$
Output Short Circuit	Continuous
Operating Temperature:	
Plastic DIP (P), SO-8 (S)	−40°C to +85°C
θ_{JA} (PDIP)	100°C/W
θ_{JA} (SOIC)	160°C/W
Storage Temperature:	
Plastic DIP (P), SO-8 (S)	−65°C to +125°C
Junction Temperature	+150°C
Lead Temperature (soldering, 10s) P packages	+300°C
(soldering, 3s) S package	+260°C

PACKAGE/ORDERING INFORMATION

PRODUCT	PACKAGE	PACKAGE DRAWING NUMBER[1]	TEMPERATURE RANGE
OPA177FP	8-Pin Plastic DIP	006	−40°C to +85°C
OPA177GP	8-Pin Plastic DIP	006	−40°C to +85°C
OPA177GS	SO-8 Surface-Mount	182	−40°C to +85°C

NOTE: (1) For detailed drawing and dimension table, please see end of data sheet, or Appendix C of Burr-Brown IC Data Book.

ELECTROSTATIC DISCHARGE SENSITIVITY

Any integrated circuit can be damaged by ESD. Burr-Brown recommends that all integrated circuits be handled with appropriate precautions. ESD can cause damage ranging from subtle performance degradation to complete device failure. Precision integrated circuits may be more susceptible to damage because very small parametric changes could cause the device not to meet published specifications.

Burr-Brown's standard ESD test method consists of five 1000V positive and negative discharges (100pF in series with 1.5kΩ) applied to each pin.

Failure to observe proper handling procedures could result in small changes to the OPA177's input bias current.

APPLICATIONS INFORMATION

The OPA177 is unity-gain stable, making it easy to use and free from oscillations in the widest range of circuitry. Applications with noisy or high impedance power supply lines may require decoupling capacitors close to the device pins. In most cases 0.1µF ceramic capacitors are adequate.

The OPA177 has very low offset voltage and drift. To achieve highest performance, circuit layout and mechanical conditions must be optimized. Offset voltage and drift can be degraded by small thermoelectric potentials at the op amp inputs. Connections of dissimilar metals will generate thermal potential which can mask the ultimate performance of the OPA177. These thermal potentials can be made to cancel by assuring that they are equal in both input terminals.

1. Keep connections made to the two input terminals close together.
2. Locate heat sources as far as possible from the critical input circuitry.
3. Shield the op amp and input circuitry from air currents such as cooling fans.

OFFSET VOLTAGE ADJUSTMENT

The OPA177 has been laser-trimmed for low offset voltage and drift so most circuits will not require external adjustment. Figure 1 shows the optional connection of an external potentiometer to adjust offset voltage. This adjustment should not be used to compensate for offsets created elsewhere in a system since this can introduce excessive temperature drift.

INPUT PROTECTION

The inputs of the OPA177 are protected with 500Ω series input resistors and diode clamps as shown in the simplified circuit diagram. The inputs can withstand ±30V differential inputs without damage. The protection diodes will, of course, conduct current when the inputs are overdriven. This may disturb the slewing behavior of unity-gain follower applications, but will not damage the op amp.

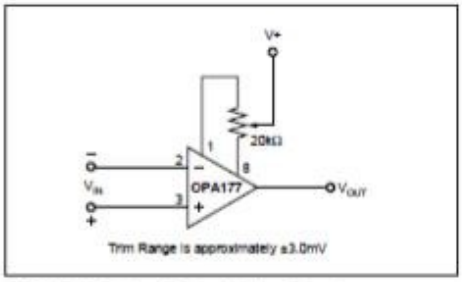

FIGURE 1. Optional Offset Nulling Circuit.

NOISE PERFORMANCE

The noise performance of the OPA177 is optimized for circuit impedances in the range of 2kΩ to 50kΩ. Total noise in an application is a combination of the op amp's input voltage noise and input bias current noise reacting with circuit impedances. For applications with higher source impedance, the OPA627 FET-input op amp will generally provide lower noise. For very low impedance applications, the OPA27 will provide lower noise.

INPUT BIAS CURRENT CANCELLATION

The input stage base current of the OPA177 is internally compensated with an equal and opposite cancellation current. The resulting input bias current is the difference between the input stage base current and the cancellation current. This residual input bias current can be positive or negative.

When the bias current is cancelled in this manner, the input bias current and input offset current are approximately the same magnitude. As a result, it is not necessary to balance the DC resistance seen at the two input terminals (Figure 2). A resistor added to balance the input resistances may actually increase offset and noise.

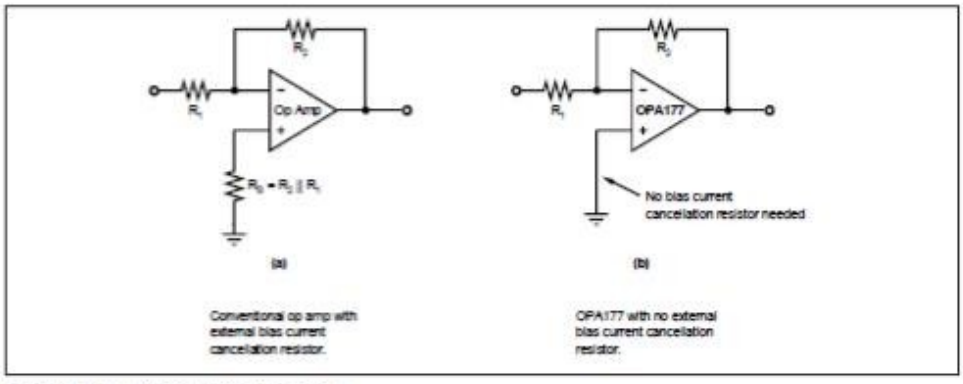

FIGURE 2. Input Bias Current Cancellation.

DRV13x Audio-Balanced Line Drivers

1 Features

- Balanced Output
- Low Distortion: 0.0005% at f = 1 kHz
- Wide Output Swing: 17Vrms into 600 Ω
- High Capacitive Load Drive
- High Slew Rate: 15 V/µs
- Wide Supply Range: ±4.5 V to ±18 V
- Low Quiescent Current: ±5.2 mA
- 8-Pin DIP, SO-8, and SOL-16 Packages
- Companion to Audio Differential Line Receivers: INA134 and INA137
- Improved Replacement for SSM2142

2 Applications

- Audio Differential Line Drivers
- Audio Mix Consoles
- Distribution Amplifiers
- Graphic and Parametric Equalizers
- Dynamic Range Processors
- Digital Effects Processors
- Telecom Systems
- Hi-Fi Equipment
- Industrial Instrumentation

3 Description

The DRV134 and DRV135 are differential output amplifiers that convert a single-ended input to a balanced output pair. These balanced audio drivers consist of high performance op amps with on-chip precision resistors. They are fully specified for high performance audio applications and have excellent ac specifications, including low distortion (0.0005% at 1 kHz) and high slew rate (15 V/µs).

The on-chip resistors are laser-trimmed for accurate gain and optimum output common-mode rejection. Wide output voltage swing and high output drive capability allow use in a wide variety of demanding applications. They easily drive the large capacitive loads associated with long audio cables. Used in combination with the INA134 or INA137 differential receivers, they offer a complete solution for transmitting analog audio signals without degradation.

The DRV134 is available in 8-pin DIP and SOL-16 surface-mount packages. The DRV135 comes in a space-saving SO-8 surface-mount package. Both are specified for operation over the extended industrial temperature range, –40°C to +85°C and operate from –55°C to +125°C.

Device Information[1]

PART NUMBER	PACKAGE	BODY SIZE (NOM)
DRV134	SOIC (16)	10.30 mm × 7.50 mm
DRV135	SOIC (8)	4.90 mm × 3.91 mm

(1) For all available packages, see the orderable addendum at the end of the datasheet.

4 Simplified Schematic

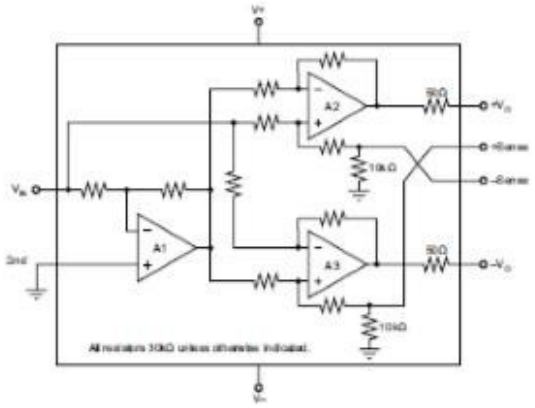

6 Pin Configuration and Functions

Top View — 8-Pin DIP/SO-8

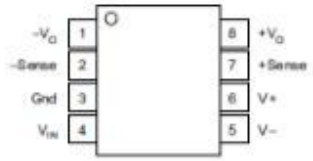

Top View — SOL-16

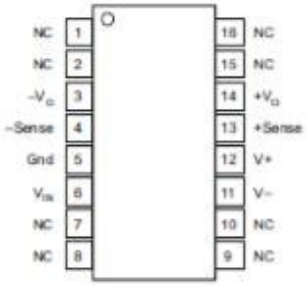

NOTE: NC - No internal connection

Pin Functions

PIN			I/O	DESCRIPTION
NAME	DIP-8 and SO-8	SOL-16		
Gnd	3	5	–	Ground
+Sense	7	13	I	Sensing, non-inverting input
–Sense	2	4	I	Sensing, inverting input
V+	6	12	–	Positive supply
V–	5	11	–	Negative supply
V_{IN}	4	6	I	Input
$-V_O$	1	3	O	Inverted, balanced differential output
$+V_O$	8	14	O	Balanced differential output
NC	–	1,2,7,8,9,10,15,16	–	These pins should be left unconnected

7 Specifications

7.1 Absolute Maximum Ratings

over operating free-air temperature range (unless otherwise noted) (1)

	MIN	MAX	UNIT
Supply voltage, V+ to V–		40	V
Input voltage range	V–	V+	
Output short-circuit (to ground)		Continuous	
Operating temperature	–55	125	°C
Junction temperature		150	°C

(1) Stresses beyond those listed under Absolute Maximum Ratings may cause permanent damage to the device. These are stress ratings only, which do not imply functional operation of the device at these or any other conditions beyond those indicated under *Recommended Operating Conditions*. Exposure to absolute-maximum-rated conditions for extended periods may affect device reliability.

7.2 Handling Ratings

			MIN	MAX	UNIT
T_{stg}	Storage temperature range		–55	125	°C
$V_{(ESD)}$	Electrostatic discharge	Human body model (HBM), per ANSI/ESDA/JEDEC JS-001, all pins(1)	–2000	2000	V
		Charged device model (CDM), per JEDEC specification JESD22-C101, all pins(2)	–500	500	

(1) JEDEC document JEP155 states that 500-V HBM allows safe manufacturing with a standard ESD control process.
(2) JEDEC document JEP157 states that 250-V CDM allows safe manufacturing with a standard ESD control process.

7.3 Recommended Operating Conditions

over operating free-air temperature range (unless otherwise noted)

		MIN	NOM	MAX	UNIT
T_{spe}	Specification temperature range	–40		85	°C
T_A	Operation temperature range	–55		125	°C
V+	Positive supply	4.5	18	18	V
V–	Negative supply	–4.5	–18	–18	V

7.4 Electrical Characteristics

At T_A = +25°C, V_S = ±18 V, R_L = 600 Ω differential connected between $+V_O$ and $-V_O$, unless otherwise noted.

PARAMETER			TEST CONDITIONS	MIN	TYP	MAX	UNIT
AUDIO PERFORMANCE							
THD+N	Total Harmonic Distortion + Noise		f = 20Hz to 20kHz, V_O = 10Vrms		0.001%		
			f = 1kHz, V_O = 10Vrms		0.0005%		
RTO(1)	Noise Floor		20 kHz BW		–98		dBu
RTO(1)	Headroom		THD+N < 1%		27		dBu
INPUT							
Z_{IN}	Input Impedance(2)				10		kΩ
I_{IN}	Input Current		V_{IN} = ±7.07 V	–1000	±700	1000	µA
GAIN							
	Differential						
	Initial		$[(+V_O) – (–V_O)]/V_{IN}$	5.8	6		dB
	Error		V_{IN} = ±10V	–2%	±0.1%	2%	
	Error vs Temperature				±10		ppm/°C
	Single-Ended		V_{IN} = ±5V				
	Initial			5.8	6		dB
	Error			–2%	±0.7%	2%	
	Error vs Temperature				±10		ppm/°C
	Nonlinearity				0.0003		% of FS
OUTPUT							
OCMR	Common-Mode Rejection, f = 1kHz		See Figure 25	46	68		dB
SBR	Signal Balance Ratio, f = 1kHz		See Figure 26	35	54		dB
	Output Offset Voltage						
V_{OCM}(3)	Offset Voltage, Common-Mode		V_{IN} = 0	–250	±50	250	mV
	Offset Voltage, Common-Mode vs Temperature				±150		µV/°C
V_{OD}(4)	Offset Voltage, Differential		V_{IN} = 0	–10	±1	10	mV
	Offset Voltage, Differential vs Temperature				±5		µV/°C
PSRR	Offset Voltage, Differential vs Power Supply		V_S = ±4.5V to ±18V	80	110		dB
	Output Voltage Swing,	Positive	No Load(5)	(V+) – 3	(V+) – 2.5		V
		Negative		(V–) + 2	(V–) + 1.5		
	Impedance				50		Ω
C_L	Load Capacitance, Stable Operation		C_L Tied to Ground (each output)		1		µF
I_{SC}	Short-Circuit Current				±85		mA
FREQUENCY RESPONSE							
	Small-Signal Bandwidth				1.5		MHz
SR	Slew Rate				15		V/µs
	Settling Time: 0.01%		V_{OUT} = 10V Step		2.5		µs
	Overload Recovery		Output Overdriven 10%		3		µs
POWER SUPPLY							
V_S	Rated Voltage				±18		V
	Voltage Range			±4.5		±18	V
I_Q	Quiescent Current		I_O = 0	–5.5	±5.2	5.5	mA

(1) dBu = 20log (Vrms /0.7746); RTO = Referred-to-Output.
(2) Resistors are ratio matched but have ±20% absolute value.
(3) $V_{OCM} = [(+V_O) + (–V_O)] / 2$.
(4) $V_{OD} = (+V_O) – (–V_O)$.
(5) Ensures linear operation. Includes common-mode offset.

Electrical Characteristics (continued)

At T_A = +25°C, V_S = ±18 V, R_L = 600 Ω differential connected between $+V_O$ and $-V_O$, unless otherwise noted.

PARAMETER			TEST CONDITIONS	MIN	TYP	MAX	UNIT
TEMPERATURE RANGE							
	Specification Range			–40		85	°C
	Operation Range			–55		125	°C
	Storage Range			–55		125	°C
θ_{JA}	Thermal Resistance	8-Pin DIP			100		°C/W
		SO-8 Surface mount			150		°C/W
		SOL-16 Surface mount			80		°C/W

7.5 Typical Characteristics

At T_A = 25°C, V_S = ±18 V, R_L = 600 Ω differential connected between $+V_O$ and $-V_O$, unless otherwise noted.

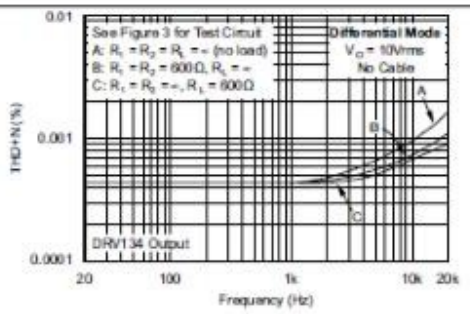

Figure 1. Total Harmonic Distortion + Noise vs Frequency

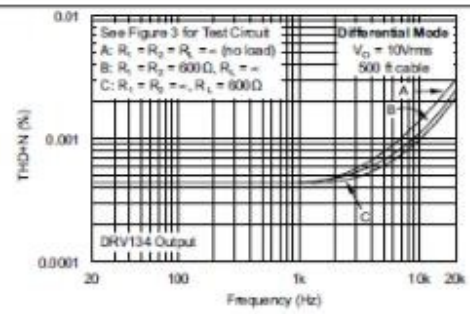

Figure 2. Total Harmonic Distortion + Noise vs Frequency

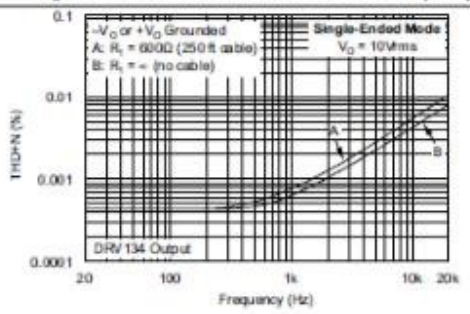

Figure 3. Total Harmonic Distortion + Noise vs Frequency

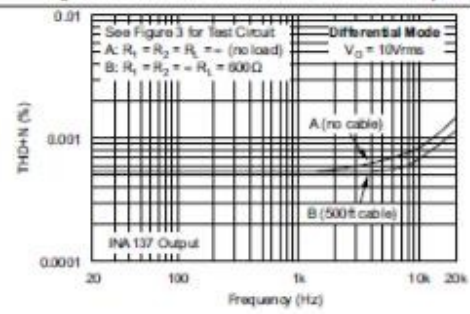

Figure 4. System Total Harmonic Distortion + Noise vs Frequency

8 Detailed Description

8.1 Overview

The DRV134 and DRV135 consist of an input inverter driving a cross- coupled differential output stage with 50 Ω series output resistors. Characterized by low differential-mode output impedance (50 Ω) and high common-mode output impedance (1.6 kΩ), the DRV134 and DRV135 are ideal for audio applications.

Excellent internal design and layout techniques provide low signal distortion, high output level (27 dBu), and a low noise floor (–98 dBu). Laser trimming of thin film resistors assures excellent output common-mode rejection (OCMR) and signal balance ratio (SBR). In addition, low dc voltage offset reduces errors and minimizes load currents.

The *Functional Block Diagram* section shows a detailed block diagram of the DRV134 and DRV135.

8.2 Functional Block Diagram

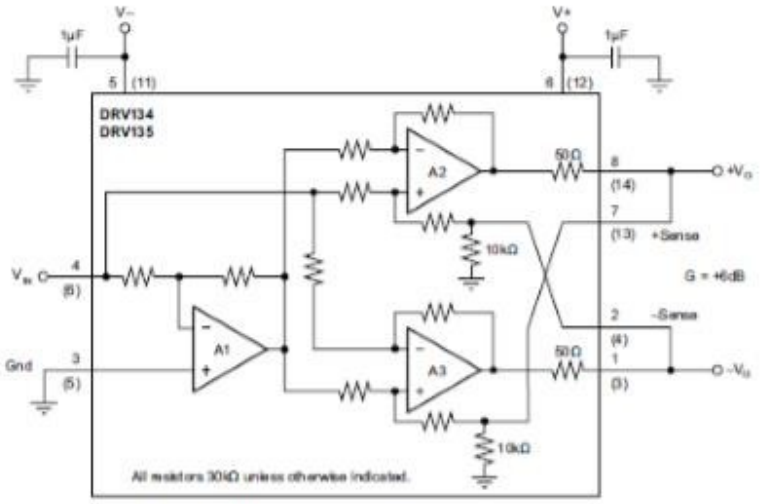

8.3 Feature Description

8.3.1 Audio Performance

The DRV134 and DRV135 were designed for enhanced ac performance. Very low distortion, low noise, and wide bandwidth provide superior performance in high quality audio applications. Laser-trimmed matched resistors provide optimum output common-mode rejection (typically 68dB), especially when compared to circuits implemented with op amps and discrete precision resistors. In addition, high slew rate (15 V/µs) and fast settling time (2.5 µs to 0.01%) ensure excellent dynamic response.

The DRV134 and DRV135 have excellent distortion characteristics. As shown in the distortion data provided in the *Typical Characteristics* section, THD+Noise is below 0.003% throughout the audio frequency range under various output conditions. Both differential and single-ended modes of operation are shown. In addition, the optional 10µF blocking capacitors used to minimize V_{OCM} errors have virtually no effect on performance. Measurements were taken with an Audio Precision System One (with the internal 80 kHz noise filter) using the THD test circuit shown in Figure 24.

Feature Description (continued)

Up to approximately 10 kHz, distortion is below the measurement limit of commonly used test equipment. Furthermore, distortion remains relatively constant over the wide output voltage swing range (approximately 2.5 V from the positive supply and 1.5 V from the negative supply). A special output stage topology yields a design with minimum distortion variation from lot-to-lot and unit-to-unit. Furthermore, the small and large signal transient response curves demonstrate the stability under load of the DRV134 and DRV135.

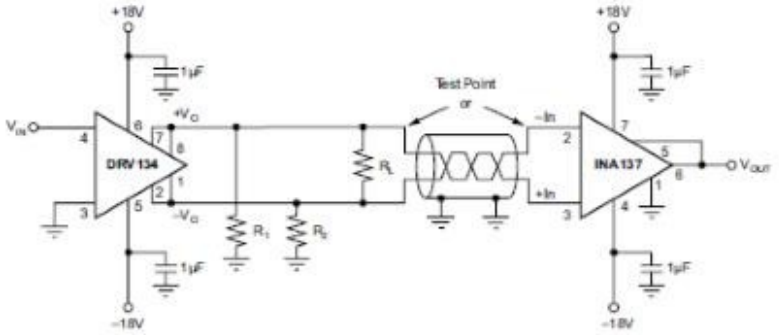

Figure 24. Distortion Test Circuit

8.3.2 Output Common-Mode Rejection

Output common-mode rejection (OCMR) is defined as the change in differential output voltage due to a change in output common-mode voltage. When measuring OCMR, V_{IN} is grounded and a common-mode voltage, VCM, is applied to the output as shown in Figure 25. Ideally no differential mode signal (VOD) should appear. However, a small mode-conversion effect causes an error signal whose magnitude is quantified by OCMR.

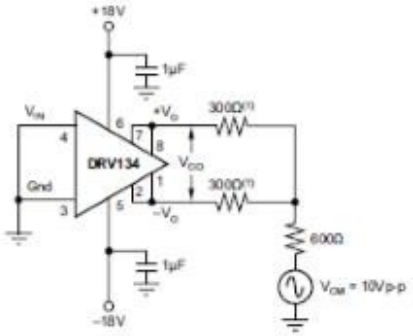

Figure 25. Output Common-Mode Rejection Test Circuit

8.3.3 Signal Balance Ratio

Signal balance ratio (SBR) measures the symmetry of the output signals under loaded conditions. To measure SBR an input signal is applied and the outputs are summed as shown in Figure 26. V_{OUT} should be zero since each output ideally is exactly equal and opposite. However, an error signal results from any imbalance in the outputs. This error is quantified by SBR. The impedances of the DRV134 and DRV135's output stages are closely matched by laser trimming to minimize SBR errors. In an application, SBR also depends on the balance of the load network.

Feature Description (continued)

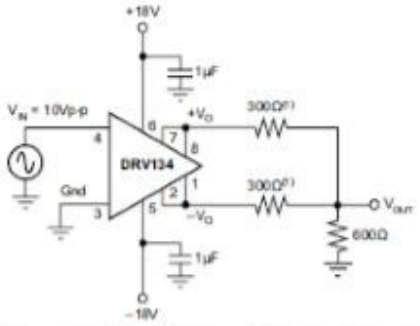

Figure 26. Signal Balance Ratio Test Circuit

8.4 Device Functional Modes

8.4.1 Differential-Output Mode

In differential-output mode, the DRV134 (and DRV135 in SO-8 package) converts a single-ended, ground-referenced input to a floating differential output with +6 dB gain (G = 2). Figure 27 shows the basic connections required for operation in differential-output mode.

Normally, $+V_O$ is connected to +Sense, $-V_O$ is connected to –Sense, and the outputs are taken from these junctions as shown in Figure 27.

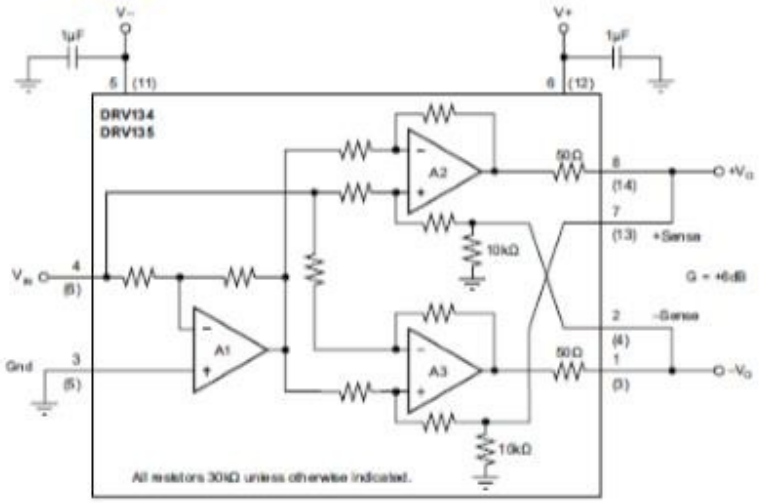

Figure 27. Basic Connections for Differential-Output Mode

Device Functional Modes (continued)

8.4.2 Single-Ended Mode

The DRV134 can be operated in single-ended mode without degrading output drive capability. Single-ended operation requires that the unused side of the output pair be grounded (both the V_O and Sense pins) to a low impedance return path. Gain remains +6 dB. Grounding the negative outputs as shown in Figure 28 results in a non-inverted output signal (G = +2) while grounding the positive outputs gives an inverted output signal (G = –2).

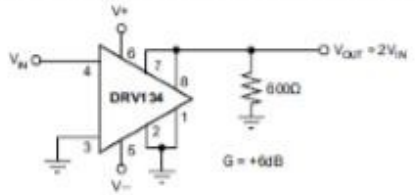

Figure 28. Typical Single-Ended Application

For best rejection of line noise and hum differential mode operation is recommended. However, single-ended performance is adequate for many applications. In general single ended performance is comparable to differential mode (see THD+N typical performance curves), but the common mode and noise rejection inherent in balanced-pair systems is lost.

9 Application and Implementation

NOTE

Information in the following applications sections is not part of the TI component specification, and TI does not warrant its accuracy or completeness. TI's customers are responsible for determining suitability of components for their purposes. Customers should validate and test their design implementation to confirm system functionality.

9.1 Application Information

Decoupling capacitors placed close to the device pins are strongly recommended in applications with noisy or high impedance power supplies.

For best system performance, it is recommended that a high input-impedance difference amplifier be used as the receiver. Used with the INA134 (G = 0 dB) or the INA137 (G = ±6 dB) differential line receivers, the DRV134 forms a complete solution for driving and receiving audio signals, replacing input and output coupling transformers commonly used in professional audio systems (Figure 29). When used with the INA137 (G = –6 dB) overall system gain is unity.

9.2 Typical Application

9.2.1 Cable Driving Application

The DRV134 is capable of driving large signals into 600-Ω loads over long cables. Low impedance shielded audio cables such as the standard Belden 8451 or 9452 (or similar) are recommended, especially in applications where long cable lengths are required.

For applications with large dc cable offset errors, a 10-µF electrolytic nonpolarized blocking capacitor at each sense pin is recommended as shown in Figure 29.

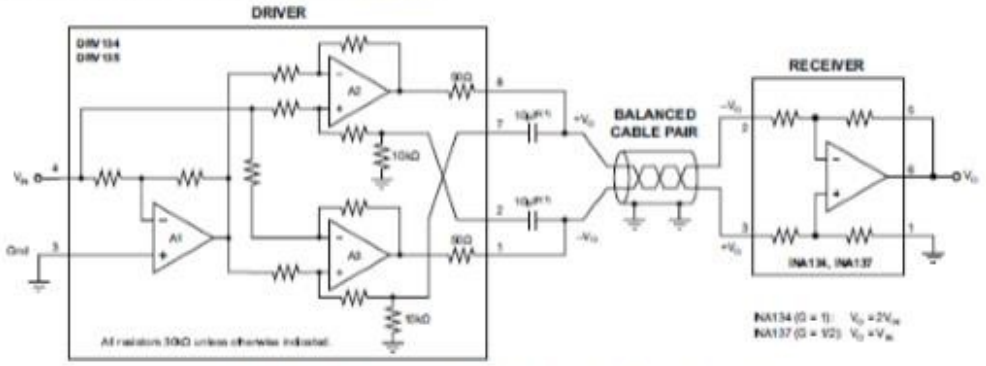

Figure 29. Complete Audio Driver and Receiver Circuit

9.2.1.1 Design Requirements

Consider a design with the goal of differentially transmitting a single ended signal of up to 22.2 dBu through 500 ft of cable with no load at the receiving side. The signal at the end of the cable should have no more than 0.002 percent of total harmonic distortion plus noise (THD+N) at 10 kHz and less than 0.0005 percent of THD+N for frequencies between 20 Hz and 1 kHz.

The system is required to put out a single ended signal 0 dB with respect to the input signal and accommodate inputs with peak to RMS ratios of up to 1.5 for the maximum 22.2 dBu range established above.

Typical Application (continued)

9.2.1.2 Detailed Design Procedure

The dBu is a common unit of measurement for input sensitivity and output level of professional audio equipment. A 0 dBu signal dissipates 1 mW into a 600-Ω resistive load; therefore, a 0 dBu signal corresponds to approximately 0.775 V_{RMS}. Equation 1 shows the relationship between the signal level in dBu (denoted by L_u) and the signal level in V_{RMS} (denoted by x).

$$L_u = 20\log_{10}\left(\frac{x}{0.775}\right) \quad (1)$$

For this design, the single ended input signal of 22.2 dBu corresponds to 9.98 V_{RMS} as shown in Equation 2.

$$V_{IN} = 0.775\left(10^{\frac{L_u}{20}}\right) = 9.98\ V_{RMS} \quad (2)$$

Given that the system must accommodate for 22.2 dBu signals with up to 1.5 of peak to RMS ratio, the maximum peak input signal is 14.97 V_{PEAK} as calculated in Equation 3.

$$V_{IN\ PEAK} = 1.5(9.98) = 14.97\ V_{PEAK} \quad (3)$$

The DRV134 is chosen to convert the single ended input signal into a differential signal and the outputs of the DRV134 will be connected to one end of the 500 ft cable. In order to prevent clipping and distortion of the input signal, the power supply rails for the DRV134 are chosen as 3 V above and below the peak calculated in Equation 3. The 3 V margin is derived from the output voltage swing specification given in the *Electrical Characteristics* table. The supplies selected are 18 V for V+ and –18 V for V–.

Finally, the INA137 is used at the end of the 500 ft cable in order to convert the differential signal output of the DRV134 into a single ended signal that is 0 dB with respect to the input signal.

Figure 30 shows the system diagram.

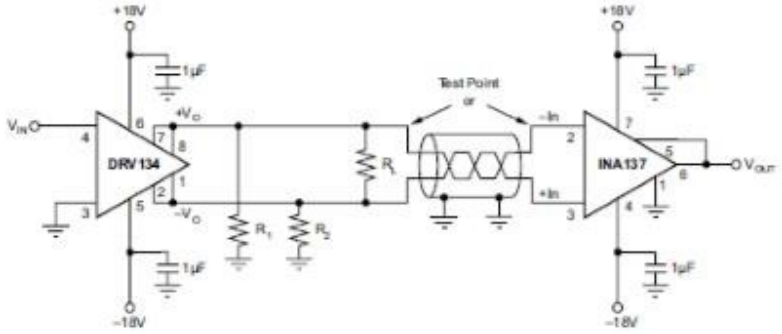

Figure 30. Diagram of System Based on DRV134 and INA137

BIOGRAPHICAL SKETCH

Dylan Michael Blackwell was born on June 16, 1993 in Waco, TX to Michael and Shirla Blackwell. He graduated from McAllen Memorial High School in 2011, after which, he attended the University of Texas-Pan American where he graduated with his Bachelor of Science in Mechanical Engineering in 2014. He continued his education at the University of Texas Rio Grande Valley and earned a Master of Science in Mechanical Engineering in December 2016. His time was spent devoted to his studies and working as a member of the Railroad Research Group. Dylan can be reached at xxdmblackwell16xx@hotmail.com or by his address located at 107 East Wisteria Avenue, McAllen, TX 78504.